Nonlinear Optical and Photorefractive Properties of Periodically Poled Channel Waveguides in Lithium Niobate

Dem Department Physik der
Universität Paderborn zur
Erlangung des akademischen
Grades eines Doktors der
Naturwissenschaften (Dr. rer. nat.)
vorgelegte

Dissertation

von

Ansgar Hellwig

1. Gutachter: Prof. Dr. W. Sohler

2. Gutachter: Prof. Dr. D. J. As

Eröffnung des Promotionsverfahrens: 4. November 2010

Tag der mündlichen Prüfung: 14. Februar 2011

Contents

継続は力なり。

1. Motivation

Digital communication has become more and more important in the last years. Especially the internet plays an important role in the daily life of many people. This results in a constantly growing demand for data bandwidth. The peak traffic at the DE-CIX internet node in Frankfurt am Main amounts to more than 3000 Gbit/s (July 2010) and has doubled in the past nine months. This development is very likely to continue.

An important means of data transportation is the optical fibre. Fibres usually consist of a core and a cladding with a lower index of refraction than the core. The light is therefore confined to the core. It can propagate over long distances because of the low attenuation in optical fibres in the so-called second and third telecom windows (i. e. wavelengths from 1260 nm to 1675 nm). These telecom windows are subdivided into several bands, the most important one being the so-called C-band ("conventional" band) spanning from 195.9 THz (1530 nm) to 191.0 THz (1569 nm). In this band, optical signals can easily be amplified using erbium-doped fibre amplifiers. The data bandwidth in fibre-optic communication is high because of the so-called wavelength division multiplexing (WDM): over a single strand of fibre, a number of data channels, which have different optical wavelengths, can be transmitted simultaneously. The channels are defined by the ITU as a grid of frequencies with a typical spacing of 100 GHz. As an example, the VSNL Transatlantic telecommunication cable system, one of the cables connecting the United Kingdom and the USA, consists of 8 fibre pairs, each of them carrying 64 wavelength channels at 10 Gbit/s each.

In optical network nodes, data packets have to be switched to another fibre connection, according to the destination of the data. If, however, the wavelength of the original incoming data channel is already in use by another data stream in the destination fibre (contention problem), the need arises to convert data from one channel to another. This can be done all-optically in so-called wavelength converters (AOWC). One possible approach is an integrated-optical device using $\chi^{(2)}$ nonlinear interaction in waveguides und using lithium niobate as substrate material. Fig. 1.1 shows, as an example, the simultaneous conversion of 103 wavelength channels. Using a strong fundamental wave at 1555 nm, the signal wavelengths in the range between 1530 nm and 1550 nm (approx.) are converted into the wavelength range between 1560 nm and 1580 nm. The signal waves are amplified during this process (so-called parametric amplification).

Lithium niobate ($LiNbO_3$) is a versatile material for optical purposes because of a number of advantageous properties. It is optically transparent over a wide

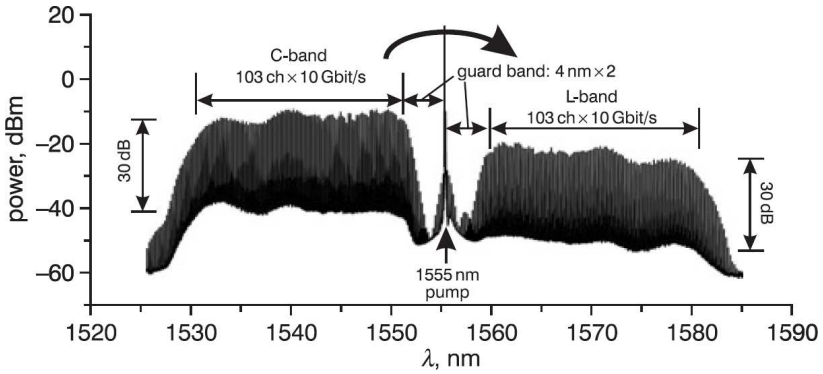

Figure 1.1.: Output spectrum of a lithium niobate wavelength converter (from [1])

wavelength range (approx. 350 nm…5000 nm [2]). Waveguides with low propagation losses ($< 0.1\,\mathrm{dB/cm}$) can be fabricated using different techniques. The material shows a number of physical effects: it's a ferroelectric material (at low temperatures), it has piezoelectric, pyroelectric, elastooptic, photorefractive, electrooptic and nonlinear optic properties.

The ferroelectric properties allow for very efficient nonlinear light interactions using the quasi phase matching scheme. A periodic reversal of ferroelectric domains is necessary for this method (periodically poled lithium niobate, PPLN). This will be described in detail later in this work.

For the mentioned application, the so-called photorefractive effect (i. e. the change in the index of refraction upon illumination with light) is a big disadvantage: because of the high light intensities, which can be achieved in waveguides, the effect is especially pronounced in integrated optical devices. The change in the refractive index leads to an unwanted change in the phase-matching conditions for nonlinear interactions, reducing the efficiency of those. Especially in titanium-indiffused waveguides, which are very widely used, the photorefractive effect is strong [3].

One method for reducing the photorefractive effect in $LiNbO_3$ crystals is heating them to approx. 180 °C. Wavelength converters using this technique, however, need to take special measures like caring for heat removal from the device or for heat-resistant fibre coupling. Devices operating at low temperature are therefore preferable.

A well-known material showing a reduced photorefractive effect in the bulk is MgO-doped lithium niobate. The doping level has to exceed a certain threshold level of approx. 4.5…5 mol% [4, 5]. However, it is difficult to grow crystals homogeneously with such a high dopant concentration. One alternative is the use of lithium niobate of stoichiometric composition. At a doping level of only 1 mol%, the light-induced index change was drastically reduced, at a level of 1.8 mol% no index change (at powers up to $8\,\mathrm{MW/cm^2}$ at 532 nm) was observed [6, 7]. One task

is to investigate if titanium-indiffused waveguides can be fabricated in this material with similar optical quality compared with the one in congruent material, and if a reduction in photorefractive sensitivity can be observed not only in the bulk material, but also in these waveguides.

Another dopant, which is also known to reduce the photorefractive effect, is zinc [8]. Because it increases the index of refraction, it can also be used for waveguide fabrication.

Yet another alternative are the so-called proton exchanged waveguides, which also have been reported to show a weaker photorefractive effect [9, 10].

The goal of this work is to find out which type of waveguide has the lowest photorefractive sensitivity, allows for the fabrication of ferroelectric domain gratings of good quality and shows a good nonlinear efficiency and is therefore best-suited for the use in nonlinear integrated optical devices operating at low temperature.

Overview of Dissertation

After an introduction to guided-wave optics and nonlinear optics in Chapter 2, the photorefractive effect will be explained in more detail (Chapter 3).

The fabrication of so-called periodically poled waveguides in lithium niobate is described in Chapter 4. This includes the material properties of $LiNbO_3$, the processing steps for preparing metal structures on the crystal surface to fabricate optical waveguides, the optical properties of those waveguides, and finally the periodic poling of the ferroelectric material. Experimental setups and measurement techniques, including a characterisation method which allows to compare different waveguide types concerning their photorefractive sensitivity, are described in Chapter 5.

After the introductory part, results of the experimental work are presented in Chapters 6 through 10. The work was part of two projects funded by the Deutsche Forschungsgemeinschaft (DFG). In a sub-project of the researcher group "Integrierte Optik in Lithiumniobat", periodically poled waveguides in MgO-doped congruent material (bulk-doped as well as indiffused MgO) were studied (Chapter 6). In that project, the fabrication of periodically poled titanium-indiffused waveguides in MgO-doped stoichiometric $LiNbO_3$ was also examined. The diffusivity of titanium in *Z*-cut MgO:SLN was determined and channel waveguides were fabricated and characterised (Chapter 7).

Fabrication and investigation of zinc-indiffused waveguides (Chapter 8) and proton exchanged waveguides (Chapters 9 and 10) were carried out as part of the project "Contention Resolution in Optical Burst Switching using Wavelength Conversion."

The dissertation will conclude with a summary and an outlook on further possible activities.

2. Theoretical Background

2.1. Light Propagation in Optical Waveguides

Integrated optics deals with optical devices on the surface of a substrate material. A waveguide in integrated optics is a small volume fraction in a dielectric medium where light can be confined perpendicular to the propagation direction by utilising an increased index of refraction compared with that of the surrounding material. It may be a simple layer (so-called planar waveguide) or it may be confined in both lateral directions (channel or stripe waveguide). Fig. 2.1 shows, as an example, a waveguide with a rectangular shape located at the surface of a substrate material, which means the cover material is air. Frequently, a waveguide has a graded index structure, e. g. when fabricated by diffusion, instead of a constant one.

The propagation of a light wave along such a waveguide (optical mode) can be described similar to a plane wave which propagates in a medium with an effective index of refraction n_{eff}. For guided modes, the effective index ranges between the bulk index n_{b} and the maximum waveguide index n_{w}. The refractive index profile of a waveguide can be considered as an analogue to a potential well. In this picture, solutions of the wave equation are analogues to energy states (see depiction in Fig. 2.2).

The electric and magnetic fields E and H of a monochromatic wave can be expressed in the following form (ω is the angular frequency and λ is the vacuum wavelength of the propagating light, z denotes the propagation direction in this

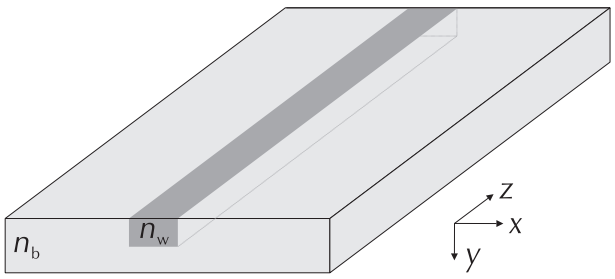

Figure 2.1.: Stripe waveguide with index n_{w}, rectangular shape, embedded in bulk material of index n_{b} and air as cover material

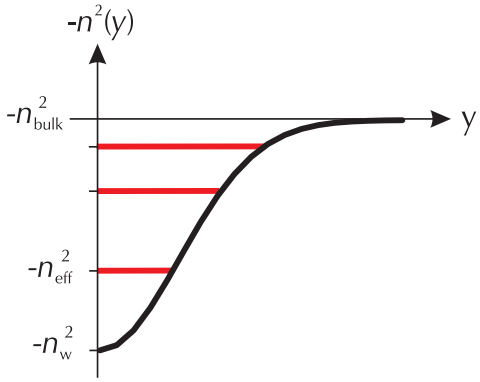

Figure 2.2.: Depiction of a refractive index profile in depth direction as a "potential well". Guided modes with effective indices n_{eff} are analogues to bound energy states. A Gaussian index profile, resulting from an indiffusion, is shown here.

chosen coordinate system):

$$\vec{E}(x,y,z,t) = \frac{1}{2}\vec{E}_0\,\mathcal{E}(x,y)\,\mathrm{e}^{\mathrm{i}(\omega t-\beta z)} + \text{c.c.} \tag{2.1a}$$

$$\vec{H}(x,y,z,t) = \frac{1}{2}\vec{H}_0\,\mathcal{H}(x,y)\,\mathrm{e}^{\mathrm{i}(\omega t-\beta z)} + \text{c.c.} \tag{2.1b}$$

$$\beta = \frac{2\pi}{\lambda}\,n_{\text{eff}} \tag{2.1c}$$

The field amplitudes E_0 and H_0 are determined by the actual power guided in the waveguide in a particular mode, $\mathcal{E}(x,y)$ and $\mathcal{H}(x,y)$ are the lateral profiles of the electric and magnetic fields, respectively.

These fields are related by Maxwell's equations (simplified here for dielectric materials)

$$\nabla\cdot\vec{D} = 0 \tag{2.2a}$$

$$\nabla\cdot\vec{H} = 0 \tag{2.2b}$$

$$\nabla\times\vec{E} = -\mu_0\frac{\partial}{\partial t}\vec{H} = -\mathrm{i}\omega\mu_0\vec{H} \tag{2.2c}$$

$$\nabla\times\vec{H} = \frac{\partial}{\partial t}\vec{D} = \mathrm{i}\omega\vec{D} \tag{2.2d}$$

where D ist the electric displacement field and μ_0 is the magnetic constant, also called vacuum permeability.

The electric displacement field is defined by

$$\vec{D} = \varepsilon_0 \vec{E} + \vec{P} \tag{2.3}$$

where P is the polarisation density (dipole moment per volume) and ε_0 is the electric constant (vacuum permittivity).

The polarisation density of the material is (in linear optics) proportional to the electric field

$$\vec{P} = \varepsilon_0 \underline{\underline{\chi}} \vec{E} \tag{2.4}$$

where χ is the electric susceptibility tensor. In general, the relation between P and E is nonlinear. Susceptibilities of higher order may then appear in the expansion of P in powers of E. This will be the topic of Section 2.2.

The susceptibility tensor can be related to the optical indices of refraction n (in the principal axis representation only diagonal elements are non-zero)

$$\underline{\underline{\chi}} = \begin{pmatrix} n_x^2 - 1 & 0 & 0 \\ 0 & n_y^2 - 1 & 0 \\ 0 & 0 & n_z^2 - 1 \end{pmatrix} \tag{2.5}$$

In stripe waveguides with a small refractive index change and a laterally slowly varying index profile, which is usually the case in diffused waveguides in lithium niobate, modes of propagation (i. e. solutions of the wave equations) can be divided into two groups according to their polarisation. Modes having a dominant electric field component in the lateral direction (E_x) and a dominant magnetic field component H_y are called quasi-transverse-electric modes (abbreviated QTE or simply TE). Modes having dominant field components H_x and E_y are called quasi-transverse-magnetic modes (QTM or TM).

The lateral field distributions $\mathcal{E}(x, y)$ and $\mathcal{H}(x, y)$ can be obtained by solving the corresponding scalar wave equations [11]:

$$\left(\frac{n_x^2}{n_z^2} \frac{\partial^2}{\partial x^2} + \frac{\partial^2}{\partial y^2} + \frac{\omega^2}{c^2} n_x^2 \right) \mathcal{E}_{x,jk} = \beta_{\mathrm{TE},jk}^2 \mathcal{E}_{x,jk} \tag{2.6}$$

$$\left(\frac{\partial^2}{\partial x^2} + \frac{n_y^2}{n_z^2} \frac{\partial^2}{\partial y^2} + \frac{\omega^2}{c^2} n_y^2 \right) \mathcal{H}_{x,jk} = \beta_{\mathrm{TM},jk}^2 \mathcal{H}_{x,jk} \tag{2.7}$$

Several numerical methods exist to solve these equations, e. g. the Gauss-Hermite-Gauss approximation [12], the effective index method [13] or the finite elements method [14].

Once $E_{y,jk}$ or $H_{y,jk}$ are calculated, the other field components can be obtained

by Maxwell's equations:

$$H_y = \frac{\beta_{\mathrm{TE}}}{\omega\mu_0} E_x \qquad H_z = \frac{\mathrm{i}}{\omega\mu_0}\frac{\partial E_y}{\partial x} \qquad \text{(QTE)}$$

$$E_y = -\frac{\beta_{\mathrm{TM}}}{n_y^2\omega\varepsilon_0} H_x \qquad E_z = -\frac{\mathrm{i}}{n_z^2\omega\varepsilon_0}\frac{\partial H_x}{\partial x} \qquad \text{(QTM)}$$

The subscripts j and k denote the number of field nodes of a particular mode in width and depth directions, respectively. Fig. 2.3 shows several examples of field distributions, which have been calculated using the effective index method for a Ti-diffused waveguide fabricated with "standard" conditions (i. e. a $1/\mathrm{e}$-depth $d \approx 5\,\mu\mathrm{m}$, see Section 4.2.1).

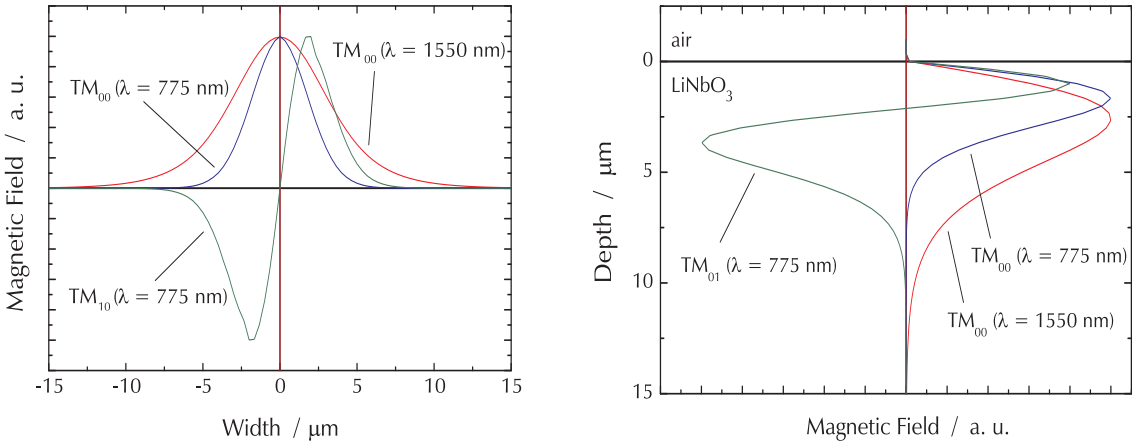

(a) Horizontal section (b) Vertical section

Figure 2.3.: Magnetic field distributions $\mathcal{H}_x$ of the fundamental modes TM_{00} at 1550 nm and 775 nm and the first higher modes TM_{01} and TM_{10} at 775 nm in a Ti-diffused waveguide

The power, which is carried by one mode, can be expressed by:

$$P = \frac{n_{\mathrm{eff}}}{2Z_0}|E_0|^2 \int_0^\infty \int_{-\infty}^\infty \mathcal{E}_{x,y}(x,y)^2\,dx\,dy \tag{2.8}$$

Z_0 denotes the free space impedance ($\approx 377\,\Omega$). The TM case uses the approximation of a weakly guided mode ($n_{\mathrm{eff}} \approx n_{\mathrm{bulk}}$, n_{bulk} being the substrate index of refraction).

2.2. $\chi^{(2)}$ Nonlinear Optical Interactions

2.2.1. The Nonlinear Polarisation

In the previous section, a linear response of the polarisation density P to the electric field E was assumed. In general, however, the dependence of P on E is a nonlinear one. A nonlinear interaction (frequency doubling) at optical frequencies was first observed by Franken et al. in 1961 [15].

A simple model for the nonlinear response is an oscillating charge, driven by an external electric field, in a non-parabolic potential [16, 17]. Fig. 2.4 schematically shows the resulting polarisation wave. It no longer resembles a sine-like function, but can be decomposed, by Fourier analysis, into several frequency components.

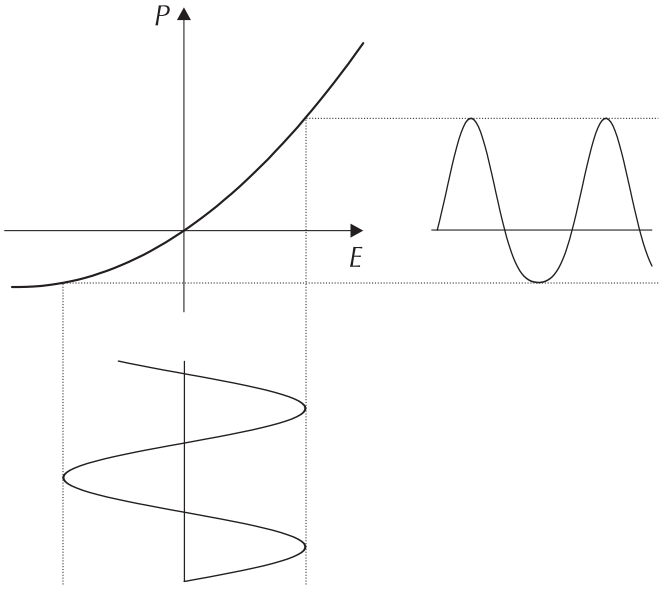

Figure 2.4.: Non-linear polarisation response $P(E)$ to an electric field E. The resulting wave contains frequency components other than the frequency of the incident wave.

The function $P(E)$ can be expanded in powers of E:

$$\vec{P} = \varepsilon_0 \left(\chi^{(1)} \vec{E} + \chi^{(2)} \vec{E}\vec{E} + \chi^{(3)} \vec{E}\vec{E}\vec{E} + \ldots \right) \tag{2.9}$$

Because of symmetry reasons, $\chi^{(2)}$ is non-zero only in materials having a non-inversion-symmetric crystal structure, which is the case in lithium niobate. The value of $\chi^{(3)}$ is much smaller than that of $\chi^{(2)}$, so the most important nonlinear effects are of the second order. This introduction will therefore be restricted to $\chi^{(2)}$ effects.

The second-rank tensor $\chi^{(2)}_{ijk}$ links two components of the electric field to one component of the polarisation density. A tensor called nonlinear coefficient can be defined by $d_{ijk} := \frac{1}{2}\chi^{(2)}_{ijk}$.[1]

$$P_i^{(\mathrm{nl})} = \varepsilon_0 \sum_{j,k} \chi^{(2)}_{ijk} E_j E_k = 2\varepsilon_0 \sum_{j,k} d_{ijk} E_j E_k \tag{2.10}$$

Please note that the coordinate system of this equation is the system of the particular material, which does not necessarily coincide with the laboratory system defined in Fig. 2.1. The crystal coordinate system of lithium niobate, the material used in this work, will be introduced in Section 4.1.1.

The nonlinear polarisation enters the wave equation as an additional "driving" term, which may give rise to excitation of optical modes at different frequencies [17].

2.2.2. Second Order Effects

If an electric field, which may now contain two frequency components, i. e.

$$\vec{E} = \vec{E}_1 + \vec{E}_2 \tag{2.11}$$

$$= \frac{1}{2}\left(\vec{E}_{01}\mathrm{e}^{\mathrm{i}\omega_1 t} + \vec{E}_{02}\mathrm{e}^{\mathrm{i}\omega_2 t} + \mathrm{c.c.}\right) \tag{2.12}$$

is inserted in Eq. (2.10), the resulting nonlinear polarisation density is

$$\begin{aligned}\vec{P}^{(\mathrm{nl})} = \frac{1}{4}\varepsilon_0 \underline{\underline{d}} \Big(&\vec{E}_{01}^2 \mathrm{e}^{\mathrm{i}\cdot 2\omega_1 t} + 2\vec{E}_{01}\vec{E}_{02}\mathrm{e}^{\mathrm{i}(\omega_1+\omega_2)t} + 2\vec{E}_{01}\vec{E}_{02}^*\mathrm{e}^{\mathrm{i}(\omega_1-\omega_2)t} \\ &+ \vec{E}_{02}^2 \mathrm{e}^{\mathrm{i}\cdot 2\omega_2 t} + \mathrm{c.c.}\Big) + \varepsilon_0 \underline{\underline{d}} \left(\vec{E}_{01}\vec{E}_{01}^* + \vec{E}_{02}\vec{E}_{02}^*\right)\end{aligned} \tag{2.13}$$

The resulting nonlinear polarisation consists of several components having different frequencies. Several effects can be assigned to these frequency components:

- Optical Rectification ($\vec{P}^{(\mathrm{nl})}(\omega = 0)$)
  This process results in a creation of a static electric field.
- Second Harmonic Generation (SHG, $\vec{P}^{(\mathrm{nl})}(\omega = 2\omega_1)$ and $\vec{P}^{(\mathrm{nl})}(\omega = 2\omega_2)$)
  The result of this effect is the generation of radiation with a doubled frequency compared with that of the incoming ("fundamental") wave.

[1] The use of i and j as index subscripts and simultaneously as imaginary unit and current density, respectively, should cause no confusion.

- Sum Frequency Generation (SFG, $\vec{P}^{(\mathrm{nl})}(\omega = \omega_1 + \omega_2)$)

  This process is similar to SHG, but in this case, two waves of different frequencies are interacting. The sum of these frequencies is the frequency of the excited third wave.

- Difference Frequency Generation (DFG, $\vec{P}^{(\mathrm{nl})}(\omega = \omega_1 - \omega_2)$)

  As a result of this process, a wave having a lower frequency than those of the two incident waves (i. e. the difference of those), is excited. Additionally, the input wave having the lower frequency is amplified. This process is called "parametric amplification".

An overview of these processed is shown in Fig. 2.5.

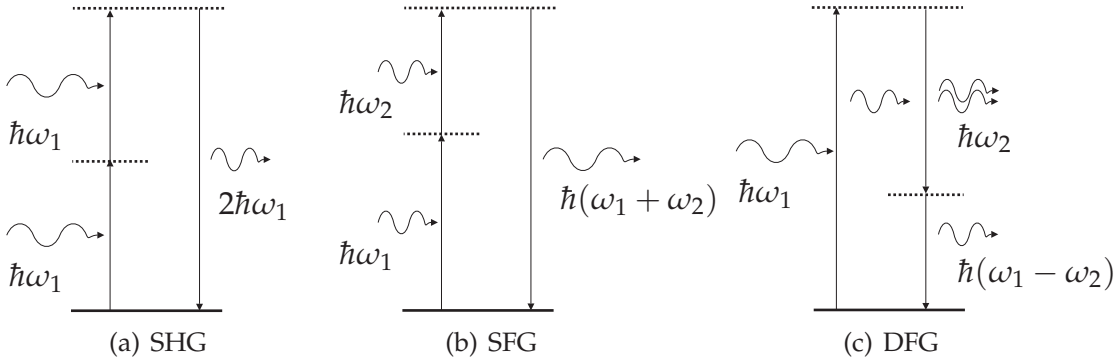

Figure 2.5.: Second-order nonlinear effects SHG, SFG, and DFG described by energy-level diagrams (see [17])

When Kleinmann's symmetry condition can be applied or in the case of second harmonic generation, the last two indices of the nonlinear tensor can be interchanged. The tensor d_{ijk} can then be written in a contracted notation d_{jl} (Voigt notation):

jk	11	22	33	23, 32	31, 13	12, 21
l	1	2	3	4	5	6

Eq. (2.10) can now be written in the form (SHG case):

$$\begin{pmatrix} P_1^{(\mathrm{nl})} \\ P_2^{(\mathrm{nl})} \\ P_3^{(\mathrm{nl})} \end{pmatrix} = 2\varepsilon_0 \begin{pmatrix} d_{11} & d_{12} & d_{13} & d_{14} & d_{15} & d_{16} \\ d_{21} & d_{22} & d_{23} & d_{24} & d_{25} & d_{26} \\ d_{31} & d_{32} & d_{33} & d_{34} & d_{35} & d_{36} \end{pmatrix} \cdot \begin{pmatrix} E_1(\omega)^2 \\ E_2(\omega)^2 \\ E_3(\omega)^2 \\ 2E_2(\omega)E_3(\omega) \\ 2E_1(\omega)E_3(\omega) \\ 2E_1(\omega)E_2(\omega) \end{pmatrix} \tag{2.14}$$

By inserting the nonlinear polarisation density into the wave equation, equations for the amplitudes of the three interacting waves can be obtained [18, 19]. The variation of the field amplitudes with the propagation direction z is considered to be small (so-called slowly varying amplitude approximation, SVEA)

$$\left|\frac{dA}{dz}\beta_\mathrm{f}\right| \gg \left|\frac{d^2A}{dz^2}\right| \tag{2.15}$$

This results in the following system of differential equations

$$\frac{dA_\mathrm{p}}{dz} = -\frac{1}{2}\alpha_\mathrm{p}A_\mathrm{p} + \mathrm{i}\frac{d_\mathrm{eff}}{c^2}\frac{\omega_\mathrm{p}^2}{\beta_\mathrm{p}}\kappa A_\mathrm{s}A_\mathrm{i}\mathrm{e}^{-\mathrm{i}\,\Delta\beta\, z} \tag{2.16a}$$

$$\frac{dA_\mathrm{s}}{dz} = -\frac{1}{2}\alpha_\mathrm{s}A_\mathrm{s} + \mathrm{i}\frac{d_\mathrm{eff}}{c^2}\frac{\omega_\mathrm{s}^2}{\beta_\mathrm{s}}\kappa A_\mathrm{p}A_\mathrm{i}^*\mathrm{e}^{\mathrm{i}\,\Delta\beta\, z} \tag{2.16b}$$

$$\frac{dA_\mathrm{i}}{dz} = -\frac{1}{2}\alpha_\mathrm{i}A_\mathrm{i} + \mathrm{i}\frac{d_\mathrm{eff}}{c^2}\frac{\omega_\mathrm{i}^2}{\beta_\mathrm{i}}\kappa A_\mathrm{p}A_\mathrm{s}^*\mathrm{e}^{\mathrm{i}\,\Delta\beta\, z} \tag{2.16c}$$

Usually, the three interacting waves are called *pump* (the strongest wave), *signal* and *idler*. The appropriate components of these fields are denoted with A_p, A_s, and A_i, respectively. The effective component of the $\underline{\underline{d}}$ tensor, which couples these field components, is called nonlinear coefficient d_eff. The mode field distributions enter the equations by the so-called overlap factor κ (the fields $\mathcal{E}$ are assumed to be normalised)

$$\kappa = \int_0^\infty \int_{-\infty}^\infty \mathcal{E}_\mathrm{p}(x,y)\mathcal{E}_\mathrm{s}(x,y)\mathcal{E}_\mathrm{i}(x,y)\,dx\,dy \tag{2.17}$$

The optical losses have been accounted for by an additional term $-\frac{1}{2}\alpha A$, α being the attenuation constant for the light intensity.

The quantity $\Delta\beta$ is called *phase mismatch* and determines (together with the nonlinear coefficient) the efficiency of the nonlinear process. This will be described in more detail in the next section.

In the special case of second harmonic generation, the equations (2.16) change into

$$\frac{dA_\mathrm{f}}{dz} = -\frac{1}{2}\alpha_\mathrm{f}A_\mathrm{f} + \mathrm{i}\frac{d_\mathrm{eff}}{c^2}\frac{\omega_\mathrm{f}^2}{\beta_\mathrm{f}}\kappa A_\mathrm{f}^*A_\mathrm{SH}\mathrm{e}^{\mathrm{i}\,\Delta\beta\, z} \tag{2.18a}$$

$$\frac{dA_\mathrm{SH}}{dz} = -\frac{1}{2}\alpha_\mathrm{SH}A_\mathrm{SH} + \mathrm{i}\frac{d_\mathrm{eff}}{c^2}\frac{\omega_\mathrm{SH}^2}{2\beta_\mathrm{SH}}\kappa A_\mathrm{f}^2\mathrm{e}^{-\mathrm{i}\,\Delta\beta\, z} \tag{2.18b}$$

2.2.3. Phase Matching

The transfer of energy from the fundamental wave to the generated wave is efficient if all the generated partial waves are in phase. This means, that the phase mismatch, defined by

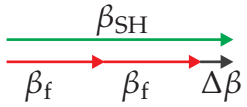

Figure 2.6.: Wave vector mismatch between fundamental and second harmonic waves

$$\Delta\beta = \beta_p - \beta_s - \beta_i \qquad \text{(DFG)} \qquad (2.19a)$$

$$\Delta\beta = \beta_{SH} - 2\beta_f \qquad \text{(SHG)} \qquad (2.19b)$$

must be zero: $\Delta\beta = 0$. This case of perfect phasematching may also be considered as "momentum conservation".

If $\Delta\beta \neq 0$, the nonlinear polarisation wave and the generated wave are getting out of phase after some distance of propagation and eventually are interfering destructively, resulting in a decreasing conversion efficiency.

The generated second harmonic power P_{SH} can especially easily be calculated from Eq. (2.18) if the material is lossless ($\alpha = 0$) and the pump wave is not depleted (A_f is constant). The SH power then is proportional to the square of the pump power P_f, to the square of the length L of the nonlinear interaction and a term depending on the phase mismatch:

$$P_{SH} \propto P_f^2 L^2 \left(\operatorname{sinc}\left(\frac{\Delta\beta\, L}{2}\right)\right)^2 \qquad (2.20)$$

Different conversion efficiencies can be defined to characterise the performance of the device:

$$\eta := \frac{P_{SH}}{P_f} \cdot 100\% \qquad [\eta] = \% \qquad (2.21)$$

$$\eta' := \frac{P_{SH}}{P_f^2} \cdot 100\% \qquad [\eta'] = \frac{\%}{\mathrm{W}} \qquad (2.22)$$

$$\eta'' := \frac{P_{SH}}{P_f^2 L^2} \cdot 100\% \qquad [\eta''] = \frac{\%}{\mathrm{W\,m^2}} \qquad (2.23)$$

The dependence of the power on the sinc^2 function is plotted in Fig. 2.7(a).

Frequently, the generated second harmonic power is plotted versus the wavelength λ of the fundamental wave. Assuming a linear relation between the full width at half maximum (FWHM) of the curve $\Delta\lambda_{FWHM}$ and $\Delta\beta_{FWHM}$ (because the spectral range of the phase matching peak is usually very small compared to

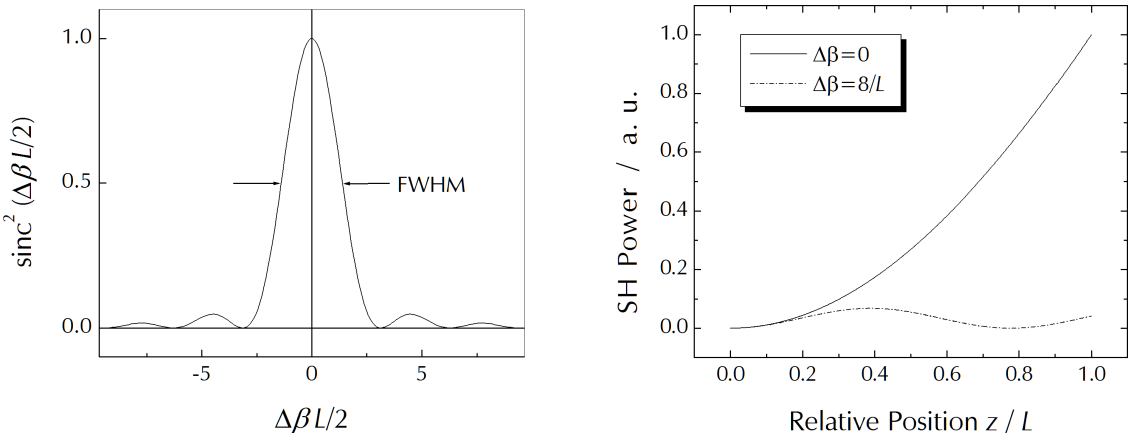

(a) sinc^2 dependence of the generated power on the phase mismatch

(b) Evolution of second harmonic power in the case of perfect phase matching and of slight mismatch

Figure 2.7.: Dependence of the generated power on phase mismatch

the absolute wavelength) leads to a relation between $\Delta\lambda_{\mathrm{FWHM}}$ and L:

$$L = \frac{5.56}{\left(2\frac{\partial\beta_{\mathrm{f}}}{\partial\lambda_{\mathrm{f}}} - \frac{1}{2}\frac{\partial\beta_{\mathrm{SH}}}{\partial\lambda_{\mathrm{SH}}}\right)\Delta\lambda_{\mathrm{f,FWHM}}} \tag{2.24}$$

Inserting values obtained from the dispersion of lithium niobate (see Sellmeier equations in Section 4.1.1) for a fundamental wavelength of $\lambda_{\mathrm{f}} = 1550\,\mathrm{nm}$ results in

$$L = \frac{11.7\,\mathrm{mm\,nm}}{\Delta\lambda_{\mathrm{f,FWHM}}} \tag{2.25}$$

Similar equations can be derived for the cases of SFG and DFG. These equations allow to assess the spatial homogeneity of the phase matching condition by comparing the calculated "effective" length with the actual sample length.

The effect of a phase mismatch is shown in Fig. 2.7(b). In the case of perfect phase matching, the generated power grows quadratically with propagation distance. The arbitrarily chosen example of $\Delta\beta\, L = 8$ shows the generation of the second harmonic wave, the decrease because of destructive interference and the eventual regeneration of SH power on a low power level.

Birefringence phase matching

A simple method for phase matching is utilising the birefringence of a material [18]. In lithium niobate, it is possible to generate a second harmonic wave in extraordinary polarisation from a fundamental wave having ordinary polarisation. The coupling nonlinear tensor element is d_{31}, see Eq. (2.14). The phase matching condition (2.19b) transforms into

$$\Delta\beta = \frac{2\pi}{\frac{1}{2}\lambda_\mathrm{f}} n_\mathrm{e}(2\omega) - 2\frac{2\pi}{\lambda_\mathrm{f}} n_\mathrm{o}(\omega) \quad \Leftrightarrow \quad n_\mathrm{e}(2\omega) = n_\mathrm{o}(\omega) \tag{2.26}$$

However, the spectral range, where this method of phase matching can be applied, is limited. Also, the d_{33} element, which is about 6 times larger in $LiNbO_3$, cannot be used.

Quasi phase matching

The so-called "quasi phase matching" (QPM) allows to fulfil the phase matching condition at virtually any wavelength in the transparency range of the material as well as to utilise any component of the nonlinear tensor. This method has already been proposed in 1962 by Armstrong et al. [16].

The principle of this method is a reversal of the sign of the nonlinear coefficient d after a certain propagation distance ("coherence length" L_c), when the phase difference between the already travelling SH wave and the newly generated partial waves is π (see Fig. 2.8). After that, instead of interfering destructively, they add constructively again, so the SH wave amplitude (and therefore, the power) rises again. Thus, the periodicity of the reversal is $\Lambda := 2L_\mathrm{c}$. On average, phase matching can be achieved for a large interaction length.

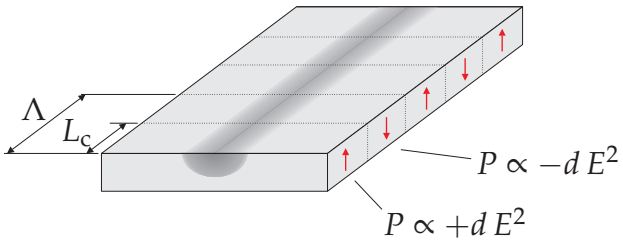

Figure 2.8.: Periodic reversal of the sign of d

From the condition $\left(\beta_\mathrm{SH} - 2\beta_\mathrm{f}\right)L_\mathrm{c} = \pi$ (in the case of SHG) a new expression for the phase mismatch in the case of QPM follows:

$$\Delta\beta = \beta_\mathrm{SH} - 2\beta_\mathrm{f} - \frac{2\pi}{\Lambda} \tag{2.27}$$

Similarly, the equation for the case of SFG/DFG reads

$$\Delta\beta = \beta_p - \beta_s - \beta_i - \frac{2\pi}{\Lambda} \tag{2.28}$$

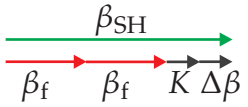

Figure 2.9.: Wave vector mismatch, QPM case

The last term in the above equation can also be considered as a "grating vector" $K = 2\pi/\Lambda$ which is added to the wave vectors of the incomig waves. The choice of Λ determines the wavelength range where phase matched interaction can take place. Fig. 2.10 shows, as an example, a so-called tuning curve, calculated for bulk $LiNbO_3$ at a temperature of 200 °C and for a periodicity of $\lambda = 18.13\,\mu m$. Phase matching for the SHG process then takes place at $\lambda_f = 1550\,nm$. Such a curve is obtained by solving Eq. (2.28) for the pump or the idler wavelength with given signal wavelength values. The corresponding third wavelength is calculated using the law of energy conservation.

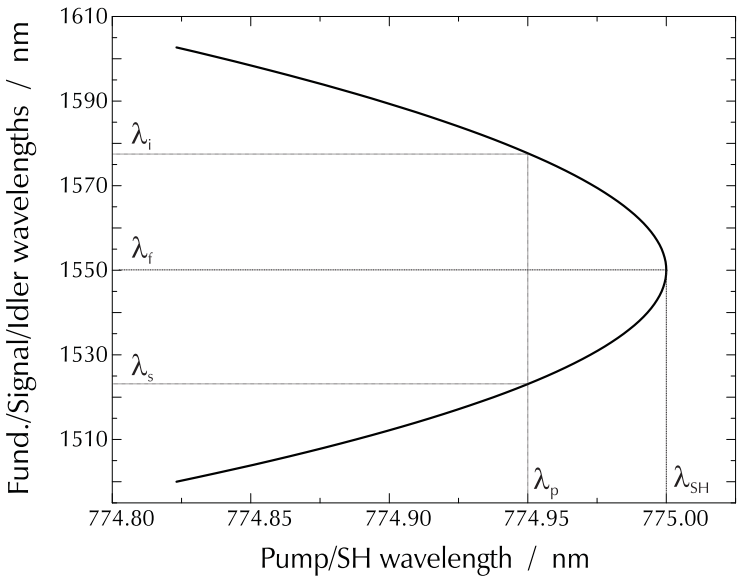

Figure 2.10.: Tuning curve for nonlinear interactions in the C-band wavelength range ($T = 200\,°C$, $\lambda_f = 1550\,nm$)

The phase mismatch is only cancelled on average by the method of QPM. This results in a smaller effective nonlinear coefficient compared with the component of the $\underline{\underline{d}}$ tensor which has been chosen in a particular application, e. g. the largest coefficient d_{33}. The periodically modulated function $d(z)$ can be expanded into a

Fourier series [19]

$$d(z) = d_{33} \sum_{m=-\infty}^{\infty} G_m e^{-iK_m z} = \sum_{m=-\infty}^{\infty} d_{\text{eff},m} e^{-iK_m z} \tag{2.29}$$

where

$$d_{\text{eff},m} = d_{33}\, G_m \tag{2.30}$$

$$K_m = \frac{2\pi m}{\Lambda} \tag{2.31}$$

For a nonlinear coefficient $d(z)$ changing periodically between $\pm d_{33}$ with a duty cycle of 50 % : 50 %, the Fourier expansion coefficients are

$$G_m = \frac{2}{m\pi} \sin\left(m \tfrac{\pi}{2}\right) \tag{2.32}$$

Using the first order grating component ($m = 1$, i. e. $K = {}^{2\pi}/_{\Lambda}$), the effective nonlinear coefficient is

$$d_{\text{eff}} = \frac{2}{\pi} d_{33} \tag{2.33}$$

The fabrication of such "domain gratings", where the sign of the nonlinear coefficient is periodically reversed, will be discussed in Section 4.3.

2.2.4. Wavelength Conversion using Cascaded Processes

Nonlinear interactions presented in the previous sections allow for the generation of light of frequencies different to those of the incoming waves. These frequencies (or wavelengths, respectively) usually differ a lot. Wavelength conversion in the telecommunication wavelength ranges, however, requires the generation of light at a wavelength very close to that of the original data channel. A solution is the cascading of two $\chi^{(2)}$ processes.

Fig. 2.11 shows a possible approach. In a first step, a second harmonic wave is generated from a strong pump. In the second step, this SH light then serves as pump for a DFG process: the second harmonic wave and the signal wave are mixed to generate an idler wave having a frequency closely spaced to the original waves. This process is called cascaded SHG/DFG (cSHG/DFG).

The bandwidth, i. e. the wavelength range, where the device can be used efficiently, can be calculated using the equations (2.28) and (2.20). Fig. 2.12(a) shows again the example of a 8 cm long device where the SHG process is phase matched for a fundamental wavelength of 1550 nm.The limits of the tuning range are usu-

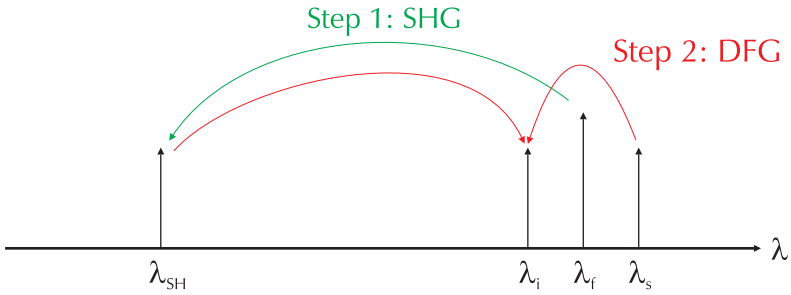

Figure 2.11.: Wavelength conversion by cascaded SHG and DFG processes

ally defined as the wavelengths where the efficiency drops below 0.5 ("3 dB tuning range"), i. e. the range is determined by the condition

$$\operatorname{sinc}^2\left(\frac{\Delta\beta(\lambda_\mathrm{p},\lambda_\mathrm{s},\lambda_\mathrm{i})\,L}{2}\right) \geq 0.5 \tag{2.34}$$

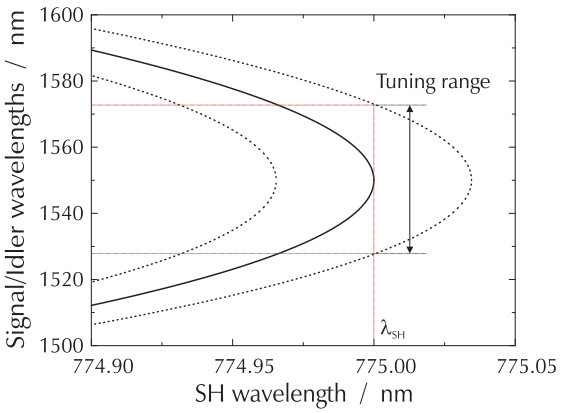

(a) Phase matching curves for perfect phase matching and 50% conversion efficiency

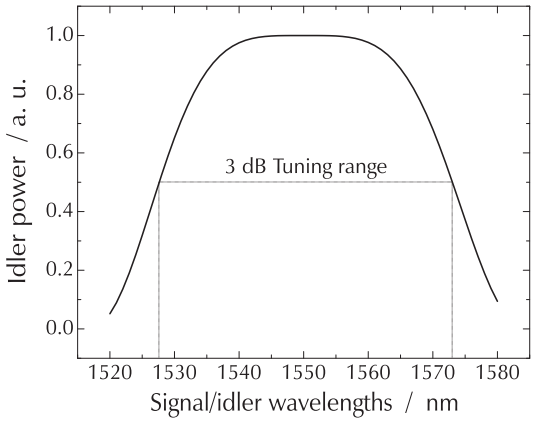

(b) Wavelength range where conversion efficiency is $> -3\,\mathrm{dB}$

Figure 2.12.: Tuning range of cSHG/SFG wavelength conversion ($L = 8\,\mathrm{cm}$, $T = 200\,°\mathrm{C}$, $\lambda_\mathrm{f} = 1550\,\mathrm{nm}$)

3. The Photorefractive Effect

The photorefractive effect is the main topic of this work and is presented in more detail in this chapter. After a short introduction with general remarks on the effect and its discovery, the effect will be described theoretically.

3.1. The Phenomenon of Photorefraction

The photorefractive effect in $LiNbO_3$ was first reported by Ashkin et al. in 1966 [20]. Laser beams having wavelengths shorter than 1 µm showed a fanning-out of the beam profile preferably parallel to the crystal's Z direction caused by index inhomogeneities. Small inhomogeneities could be erased by illuminating a larger area with light of the same wavelength. Heating the sample to approx. 170 °C made the effect dissappear. While the origin of this inhomogeneity was unknown at that time, the detrimental effect on nonlinear optic devices was already recognized. The effect is therefore sometimes called "optical damage". Fig. 3.1 shows own photographs of the intensity profile of a green laser beam ($\lambda = 532\,\text{nm}$) transmitted through a 30 mm long CLN crystal developing over time.

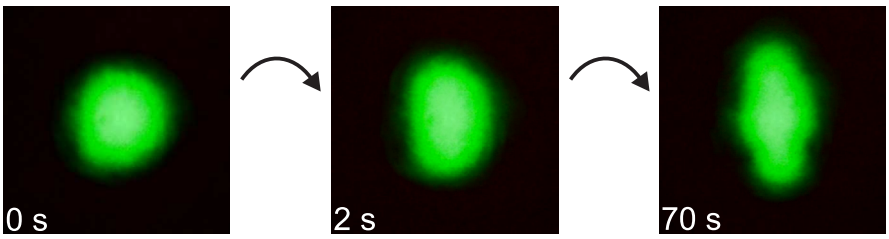

Figure 3.1.: Green laser beam (8 mW focused to a waist of $\approx$ 100 µm) transmitted through a CLN crystal (Z axis is vertical)

Especially in waveguide devices, the index inhomogeneities are detrimental, because—at least for multi-moded waveguides—there will be no equilibrium state. Waveguides, which are single-mode at a wavelength of e.g. 1550 nm, will guide several transverse modes at short wavelengths. If the index profile of the waveguide is perturbed locally by the photorefractive effect, this will lead to mode coupling and the transverse mode(s) of propagation will change. Because of the now different intensity profile, the index perturbation also changes, which again effects the modes of propagation, and so on (see Fig. 3.2).

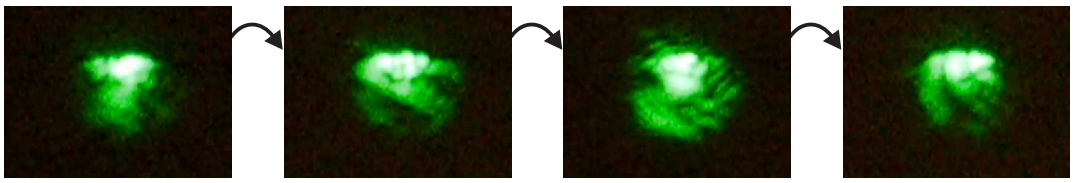

Figure 3.2.: Near field image of green light guided in a 7 µm wide Ti-diffused channel waveguide (images taken with an interval of a few seconds)

Ashkin et al. mention a number of possible origins of this effect. Later, an explanation of the effect was proposed by Chen et al. [21, 22], which quickly became accepted and extended. Their explanation consists of the drift of charge carriers after optical excitation, a build-up of a space-charge field and the change of the index of refraction by the electrooptic effect.

3.2. Theoretical Description

The photorefractive effect occurs in several stages (see Fig. 3.3). First, charge carriers are excited. The spatially modulated charges lead to spatially modulated currents. Electrical space-charge fields E_{SC} build up. The index of refraction is finally changed by means of the electrooptic effect: $\Delta n \propto -E_{SC}$.

This section will present an overview of the different types of current, which may occur, and of different charge transport models.

The photorefractive properties of lithium niobate will be presented in Section 4.1.4.

3.2.1. Charge Driving Forces

The total current density j is determined by three contributions [23, 24]

$$\vec{j} = \vec{j}_{\text{drift}} + \vec{j}_{\text{diff}} + \vec{j}_{\text{phg}} \tag{3.1}$$

where j_{drift} is the drift current, j_{diff} is the current resulting from charge carrier diffusion and j_{phg} is the contribution of the photogalvanic effect.

The drift current is simply an ohmic current

$$\vec{j}_{\text{drift}} = \underline{\underline{\sigma}}\vec{E} = e\underline{\underline{\mu}}_{\text{e}} N \vec{E} \tag{3.2}$$

where $\underline{\underline{\sigma}}$ is the conductivity tensor, $\underline{\underline{\mu}}_{\text{e}}$ the mobility tensor (for simplicity, no hole conduction is considered here), e the elementary charge, N the electron density in the conduction band, and $\vec{E}$ the electric field.

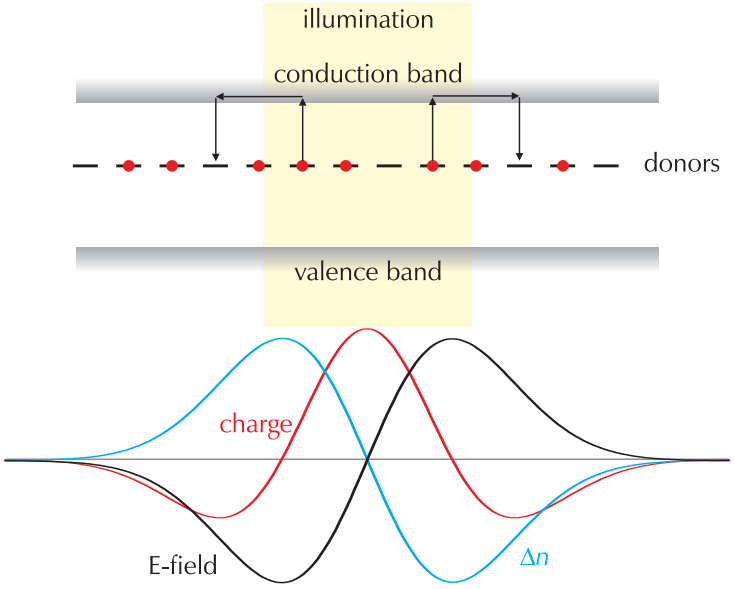

Figure 3.3.: Band transport model of the photorefractive effect. Charges are moving out of the illuminated area, resulting in an inhomogeneous charge distribution. A space-charge field builds up, which changes the refractive index. A possible preferential direction of charge movement is not taken into account here.

The electric field, again, is also determined by three contributions:

$$\vec{E} = \vec{E}_{\mathrm{SC}} + \vec{E}_{\mathrm{ext}} + \vec{E}_{\mathrm{pyro}} \tag{3.3}$$

where $\vec{E}_{\mathrm{SC}}$ is the space-charge field, $\vec{E}_{\mathrm{ext}}$ is an externally applied field and $\vec{E}_{\mathrm{pyro}}$ is an electric field generated by the pyroelectric field upon temperature change: $\vec{E}_{\mathrm{pyro}} \propto {}^{\partial P_{\mathrm{s}}}/_{\partial T}\, \Delta T$, where P_{s} is the spontaneous polarisation density.

While the pyroelectric effect is of minor importance for light at slowly changing low intensities, it must be taken into account for pulsed illumination at high power levels.

The diffusion current is driven by concentration gradients in the free charge carriers:

$$\vec{j}_{\mathrm{diff}} = e\underline{\underline{D}}\nabla N = \underline{\underline{\mu}}_{\mathrm{e}} k_{\mathrm{B}} T \nabla N \tag{3.4}$$

where $\underline{\underline{D}}$ is the diffusivity tensor and with $e\underline{\underline{D}} = \underline{\underline{\mu}}_{\mathrm{e}} k_{\mathrm{B}} T$.

The photogalvanic effect (also called bulk photovoltaic effect) is present in crystals lacking inversion symmetry, e. g. lithium niobate. Glass et al. [25] reported on photocurrents proportional to the absorbed light intensity:

$$j_{\mathrm{phg}} = \kappa \alpha I \tag{3.5}$$

where α is the absorption coefficient, I is the light intensity (in units of power per area), and κ is a proportionality constant now known as Glass constant.

Later, the photogalvanic current was found to be polarisation dependent [26], so a photogalvanic tensor was introduced [27]:

$$j_{\mathrm{phg},i} = \sum_{j,k} \frac{1}{2} \left(\alpha_{ijk} E_j^* E_k + \mathrm{c.c.} \right) \tag{3.6}$$

where α_{ijk} are the components of the photogalvanic tensor. It can be written, like the nonlinear optical tensor, in a contracted notation $\alpha_{ijk} \rightarrow \alpha_{il}$.

Calculating the resulting space-charge fields means fulfilling the Poisson equation and the continuity equation.

$$\nabla \cdot \vec{D} = \varrho \tag{3.7}$$

$$\nabla \cdot \vec{j} + \frac{d\varrho}{dt} = 0 \tag{3.8}$$

3.2.2. Charge Transport Models

The simplest model describing the excitation and re-trapping of charge carriers is a model using only one trap (one-centre model), which has two possible valence states. It is shown in Fig. 3.4(a). A filled donor is labelled D^0, an ionised donor is labelled D^+. Acceptors and interaction with the valence band will not be treated here. For more information on other charge transport models, see Ref. [24].

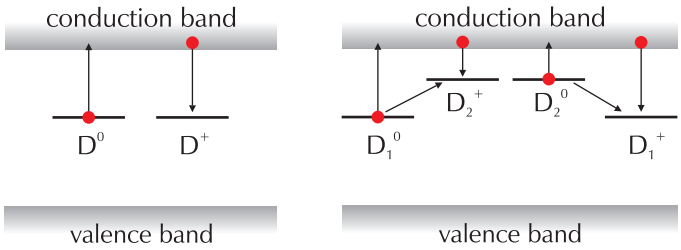

(a) One-centre model (b) Two-centre model

Figure 3.4.: One-centre and two-centre charge transport models (see [24])

A rate equation for ionised and neutral donors can be set up as follows [23, 28]

$$\frac{dN^+}{dt} = -\frac{dN^0}{dt} = (\beta + qsI)N^0 - \gamma N^+ N \tag{3.9}$$

where N^0 and N^+ are the concentrations of the D^0 and the D^+ centres, respectively, β is the thermal generation rate, q is the quantum efficiency for exciting

an electron when a photon is absorbed, s is the absorption cross section, I is the photon flux and γ is the recombination coefficient.

A second model includes not only deep traps, but also a second type of traps being more shallow ones (Fig. 3.4(b)). Also for this model, rate equations can be set up, now including the concentrations of the two types of traps as well as the possible direct interaction between deep and shallow traps [29].

$$\frac{dN_1^+}{dt} = \left(\beta_1 + q_{1\to2}s_{1\to2}N_2^+\right) I N_1^0 - \left(\gamma_1 N + \gamma_{2\to1}N_2^0\right) N_1^+ \tag{3.10}$$

$$\frac{dN_2^+}{dt} = \left(\beta_2 + q_2 s_2 I + \gamma_{2\to1}N_1^+\right) N_2^0 - \left(\gamma_2 N + q_{1\to2}s_{1\to2} I N_1^0\right) N_2^+ \tag{3.11}$$

where the subscripts 1 and 2 denote the traps D_1 and D_2, respectively.

The carrier densities enter Eqs. (3.7) and (3.8) according to

$$\varrho = -e(N + N^0 - N_C) \qquad \text{(one centre)} \tag{3.12a}$$

$$\varrho = -e(N + N_1^0 + N_2^0 - N_C) \qquad \text{(two centres)} \tag{3.12b}$$

where N_C is the concentration of non-mobile charges required to maintain charge neutrality.

Usually, except for very high light intensities, the density of free charge carriers N is small compared with the number of photorefractive centers and can therefore be neglected. The time derivative $\dot{N}$, entering Eq. (3.8) by Eq. (3.12a) or Eq. (3.12b), respectively, also can usually be neglected (so-called "adiabatic approximation"), except for the case of very short light pulses.

Jermann et al. [29] derive for the case of Fe-doped $LiNbO_3$ and continuous-wave illumination, after some approximations, an expression for the photoconductivity

$$\sigma_{ph} = e\mu_e \frac{q_1 s_1 I (N_1^0 + N_1^+ - N_C) + \left(\beta_2 + (q_2 s_2 - q_1 s_1) I\right) N_2^0}{\gamma_1 (N_C + N_2^0)} \tag{3.13}$$

With their definition of the photogalvanic current density

$$j_{phg} = \kappa_1 I N_1^0(I) + \kappa_2 I N_2^0(I) \tag{3.14}$$

where κ_1 and κ_2 are the photogalvanic coefficients of the deep and the shallow centres, they obtain the following expression for the saturation value of the refractive index change by the electrooptic effect:

$$\Delta n_s = \frac{1}{2} n^3 r \frac{\kappa_1 I (N_1^0 + N_1^+ - N_C) + (\kappa_2 - \kappa_1) I N_2^0}{\sigma_{ph}} \tag{3.15}$$

4. Periodically Poled Channel Waveguides in Lithium Niobate

In this chapter, the material "lithium niobate" is introduced. Important linear, nonlinear, and photorefractive properties are given. Different technologies to achieve waveguiding in this material are presented in the second section. Finally, the inversion of ferroelectric domains using electric fields is described.

4.1. Properties of Lithium Niobate

A number of important properties of lithium niobate have already been mentioned in the first chapter. This section will focus on those ones being important for nonlinear optics. More detailed overviews of the material can be found in further literature, e.g. [2, 30–32].

4.1.1. Stoichiometry and Crystal Structure

Lithium niobate cannot be found in nature, but is grown artificially usually by the Czochralski method. The starting materials are lithium carbonate and niobium oxide. Different compounds exist in the system Li_2O–Nb_2O_5 (see Fig. 4.1). The compound "$LiNbO_3$" can exist in a small range around the ratio of 50 mol%. Crystal growth is usually done from a melt having a composition which is the same as that of the grown crystal (so-called congruent melt, leading to the name congruent lithium niobate, CLN). However, this composition is not 50 mol% (i. e. a [Li]/[Nb] ratio of 1:1), but is lithium deficient. The congruent composition is approximately 48.4 mol% [33], resulting in a [Li]/[Nb] ratio of 0.938. Material having really the composition "$LiNbO_3$" is called stoichiometric lithium niobate (SLN). Crystals with this composition are more difficult to grow. Methods used for this are the double-crucible Czochralski growth (DCCZ) [34, 35] or the top-seeded solution growth (TSSG) from a flux containing K_2O [36]. Another method for changing the composition of existing congruent crystals to a stoichiometric one is the so-called vapour transport equilibration (VTE) [37, 38].

The crystal structure of lithium niobate belongs to the trigonal space group R3c (at low temperatures). The hexagonal unit cell is depicted in Fig. 4.2, including the hexagonal axes a, b, c and the axes of the cartesian crystal coordinate system X, Y, Z. The cations Li^+ und Nb^{5+} are displaced along the Z axis with respect

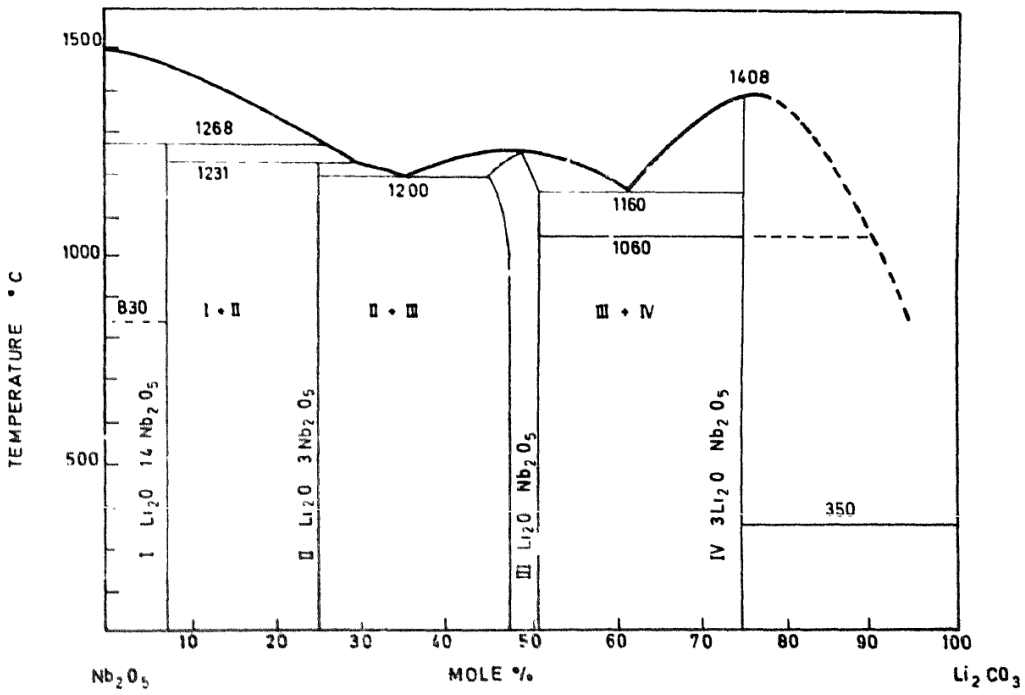

Figure 4.1.: Phase diagram of $LiNbO_3$ (from [39])

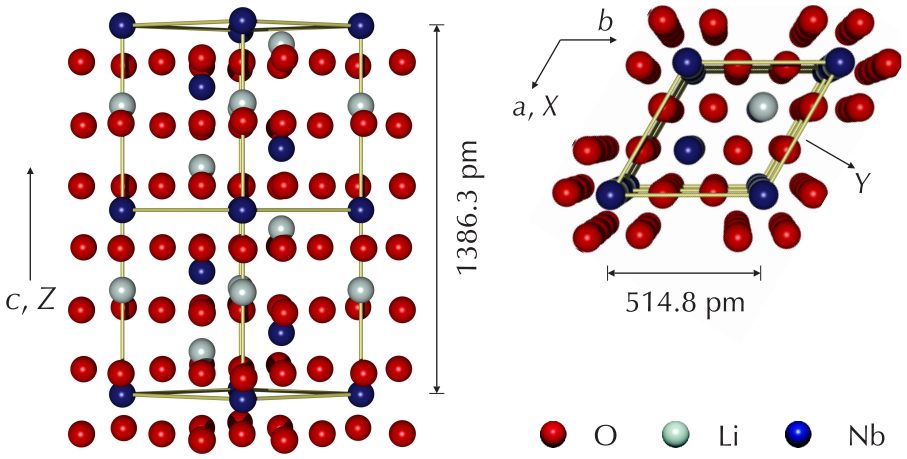

Figure 4.2.: Crystal structure of $LiNbO_3$

to their positions above the transition temperature T_C in the oxygen planes and in the middle between the oxygen planes, respectively. This results in a spontaneous dielectric polarisation. In this phase, lithium niobate is a ferroelectric material. The value of the spontaneous polarisation is $P_s \approx 80\,\mu C/cm^2$ and is relatively insensitive to the crystal nonstoichiometry [40].

In nonstoichiometric crystals, several crystal defects can occur because of the lithium deficiency. These defects include niobium antisite defects and vacancies on either the lithium or the niobium sites, which are created to maintain charge neutrality [41–44]. In the niobium vacancy model, each missing Nb^{5+} ion is replaced by a Li^+ ion, with compensating vacancies at the Nb site (according to the formula $[Li_{1-5x}Nb_{5x}][Nb_{1-4x}V_{4x}][O_3]$). In the lithium vacancy model model, niobium ions occupy lithium positions with the creation of an appropriate amount of lithium vacancies for charge compensation ($[Li_{1-5x}Nb_xV_{4x}][Nb][O_3]$).

4.1.2. Linear Optical Properties

Lithium niobate is an unaxial crystal with negative birefringence, i. e. the ordinary index of refraction is larger than the extraordinary one ($n_e - n_o < 0$). The refractive indices are dependent on wavelength and temperature. For undoped congruent $LiNbO_3$, a Sellmeier fit by Edwards and Lawrence [45] is frequently used. The fit is considered to be valid with reasonable accuracy over nearly the whole transparency range.

$$n_{o,e}^2 = A_1 + \frac{A_2 + B_1 F}{\lambda^2 - (A_3 + B_2 F)^2} + B_3 F - A_4 \lambda^2 \tag{4.1}$$

where

$$F = (T - 24.5\,°C)(T + 570.5\,°C)$$
$$T \text{ in } °C,\ \lambda \text{ in } \mu m$$

Another Sellmeier fit was developed by Schlarb und Betzler [46]. They also took into account the stoichiometry (lithium content) of the crystal c_{Li} as well as a doping with magnesium oxide (c_{Mg}). The threshold concentration c_{thr} in Eq. (4.2) is considered to have a linear behaviour between 5 mol% for congruent (they assume $c_{Li} = 48.5$ mol%) and 0 mol% for stoichiometric $LiNbO_3$. The fit is valid in the range $\lambda = 400 \ldots 1200$ nm. The numerical values of the parameters in both fits are listed in Tables 4.1 and 4.2.

$$n_i^2 = \frac{A_{0,i}(c_{Li}, c_{Mg})}{\lambda_{0,i}(T)^{-2} - \lambda^{-2}} - A_{IR,i}\lambda^2 + A_{UV} \tag{4.2}$$

where

$$A_{0,i}(c_{\mathrm{Li}}, c_{\mathrm{Mg}}) = \begin{cases} A_{0,i} + \frac{c_{\mathrm{thr}} - c_{\mathrm{Mg}}}{5\,\mathrm{mol\%}} A_{\mathrm{Nb_{Li}},i} + c_{\mathrm{Mg}} A_{\mathrm{Mg},i} & \text{if } c_{\mathrm{Mg}} < c_{\mathrm{thr}} \\ A_{0,i} + c_{\mathrm{Mg}} A_{\mathrm{Mg},i} & \text{if } c_{\mathrm{Mg}} > c_{\mathrm{thr}} \end{cases}$$

$$c_{\mathrm{thr}} = \frac{5\,\mathrm{mol\%}}{1.5\,\mathrm{mol\%}}(50\,\mathrm{mol\%} - c_{\mathrm{Li}}) \quad \text{for } 48,5\,\mathrm{mol\%} \leqslant c_{\mathrm{Li}} \leqslant 50\,\mathrm{mol\%}$$

$$\lambda_{0,i}(T) = \lambda_{0,i} + \mu_{0,i}\big(f(T) - f(24.5\,^{\circ}\mathrm{C})\big)$$

$$f(T) = (T + 273)^2 + 4.0238 \times 10^5 \left(\frac{261.6}{T + 273} - 1\right)$$

$c_{\mathrm{Li/Mg/thr}}$ in mol%, λ in nm, T in °C, i = e,o

Table 4.1.: Parameters for the Sellmeier fit by Edwards und Lawrence [45]

	n_{o}	n_{e}
A_1	4.9048	4.8520
A_2	0.11775	0.09921
A_3	0.21802	0.21090
A_4	0.027153	0.021940
B_1	2.2314×10^{-8}	5.2716×10^{-8}
B_2	-2.9671×10^{-8}	-4.9143×10^{-8}
B_3	2.1429×10^{-8}	2.2971×10^{-7}

Table 4.2.: Parameters for the Sellmeier fit by Schlarb und Betzler [46]

	n_{o}	n_{e}
λ_0	223.219	218.203
μ_0	1.1082×10^{-6}	6.4047×10^{-6}
A_0	4.5312×10^{-5}	3.9466×10^{-5}
$A_{\mathrm{Nb_{Li}}}$	-7.2320×10^{-8}	11.8635×10^{-7}
A_{Mg}	-7.3548×10^{-8}	7.6243×10^{-8}
A_{IR}	3.6340×10^{-8}	3.0998×10^{-8}
A_{UV}	2.6613	2.6613

4.1.3. Nonlinear Optical Properties

The nonlinear tensor $\underline{\underline{d}}$ was introduced in Section 2.2. It consists, in general, of 18 elements in the contracted notation. If the crystal structure and its symmetries are taken into account, some tensor elements may be zero or some elements equal to other ones. In the case of lithium niobate, the nonlinear tensor looks like (see [2])

$$\underline{\underline{d}} = \begin{pmatrix} 0 & 0 & 0 & 0 & d_{31} & -d_{22} \\ -d_{22} & d_{22} & 0 & d_{31} & 0 & 0 \\ d_{31} & d_{31} & d_{33} & 0 & 0 & 0 \end{pmatrix} \tag{4.3}$$

In a recent study, Shoji et al. [47] obtain values for the coefficients d_{33} and d_{31} (see Tab. 4.3). The value of d_{22} is even smaller than d_{31} [18], so it's hardly made use of in practice. Values for other wavelengths can be calculated using Miller's rule [17]. The validity of this rule, however, is doubted [47].

Table 4.3.: Nonlinear coefficients of $LiNbO_3$ and MgO:$LiNbO_3$ in pm/V at $\lambda = 1313\,\text{nm}$ (from [47])

	$LiNbO_3$	MgO(1%):$LiNbO_3$	MgO(5%):$LiNbO_3$
d_{33}	19.5	20.3	20.3
d_{31}	3.2	3.2	3.4

4.1.4. Photorefractive Properties

Charge transport mechanisms have been introduced in Section 3.2. In $LiNbO_3$, the photorefractive effect can be explained at low light intensities by the one-centre model [48]. The responsible centres usually are iron atoms. Even in nominally pure lithium niobate, impurities in the ppm range are present [33]. Iron can occur in the valence states Fe^{2+} (serving as donor) and Fe^{3+} (serving as trap).

The main charge transport mechanism is the photogalvanic current, the dominant charge carriers are electrons. When illuminated with UV light, also holes can contribute to the effect because of a direct excitation from the valence band. The simple one-centre model has to be extended then [48].

In deliberately iron-doped material, the photorefractive effect can be enhanced and utilised for applications like the creation of holographic gratings (see e. g. [49]).

At high light intensities, the one-centre model is no longer sufficient. The effects ocurring then, like a nonlinear dependence of the photoconductivity on the light intensity, can be explained by the two-centre model also introduced in Section 3.2. The shallow centre was identified as Nb^{5+} on a Li^+ site, called a small polaron. This kind of defect is especially abundant in congruent (i. e. lithium-deficient) lithium niobate (see explanation of the defect structure above).

Several dopants are known to reduce the photorefractive effect, magnesium being the most well-known one. Doping with magnesium or zinc increases the photoconductivity, therefore reducing the saturation value of the refractive index change [50]. Incorporation of protons increases the dark conductivity [51]. Also other metals like zirconium [52], scandium [53] or hafnium [54] are known to reduce the photorefractive effect.

Frequently, a threshold behaviour is observed. The photorefractive effect is only reduced significantly if the doping level exceeds a certain value. For magnesium doped lithium niobate (also called magnesium oxide doped, because MgO is used as one of the starting material for the crystal growth), this value is approx. 5 mol% for material with congruent composition. For material having stoichiometric composition, however, this value is significantly lower. Furukawa et al. could observe no optical damage for MgO concentrations exceeding 1 mol% [6] (see Fig. 4.3).

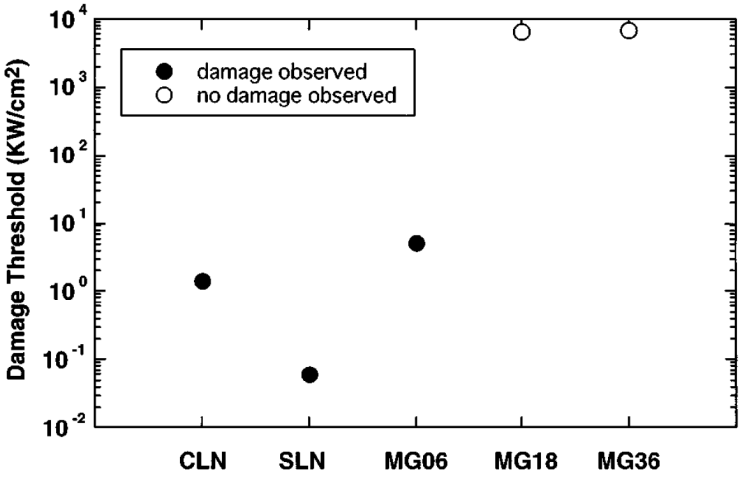

Figure 4.3.: Damage thresholds for undoped CLN, undoped SLN and SLN doped with 0.6 mol%, 1.8 mol% and 3.6 mol% magnesium, respectively (from [6])

4.2. Properties of Optical Waveguides

4.2.1. Titanium-indiffused Waveguides

Schmidt and Kaminow reported on the fabrication of waveguides by indiffusion of metals, including titanium, in 1974 [55]. This waveguide type has become the most well-known one in $LiNbO_3$ because of several advantages: waveguiding is possible in both TE and TM polarisations, the nonlinear properties of the substrate material are preserved, and the propagation losses are very low ($< 0.1\,\mathrm{dB/cm}$).

A simple model to describe the increase in the index of refraction induced by the indiffused titanium is based on the assumptions of a constant concentration-independent diffusion coefficient and an index increase which only depends on the local Ti concentration [13, 56–58].

Diffusing a titanium stripe of small thickness τ and width w leads to the following solution of the diffusion equation for the local concentration c [56]:

$$c_{\mathrm{Ti}}(x,y) = c_0\, f(y)\, g(x) \tag{4.4}$$

where

$$f(y) = \mathrm{e}^{-y^2/d_y^2} \tag{4.5}$$

$$g(x) = \frac{1}{2\,\mathrm{erf}\left(\frac{w}{2d_x}\right)} \left(\mathrm{erf}\left(\frac{\frac{1}{2}w + x}{d_x}\right) + \mathrm{erf}\left(\frac{\frac{1}{2}w - x}{d_x}\right) \right) \tag{4.6}$$

The diffusion depths d_x and d_y (1/e depth) for the width and depth directions, respectively, are related to the diffusion coefficient D and the diffusion time t by $d_{x,y} = 2\sqrt{D_{x,y}t}$. The maximum surface concentration c_0 is related to the initial stripe thickness by

$$c_0 = \frac{2\varrho N_\mathrm{A}}{M_\mathrm{Ti} d_y \sqrt{\pi}} \operatorname{erf}\left(\frac{w}{2d_x}\right) \tau \tag{4.7}$$

where $\varrho = 4.507\,\mathrm{g/cm^3}$ is the density of titanium (bulk density is assumed here for evaporated layers), $N_\mathrm{A} = 6.02214179 \times 10^{23}\,\mathrm{mol^{-1}}$ is the Avogadro number, and $M_\mathrm{Ti} = 47.867\,\mathrm{g/mol}$ is the molar mass of the deposited material.

The dependence of the index increase Δn on the local concentration has been shown to be a linear one for the extraordinary index and a nonlinear one for the ordinary index [58]. The wavelength-dependent index increase can be expressed as [59, 60]

$$\Delta n_\mathrm{e}(\lambda, c) = E c_\mathrm{Ti} \frac{0.839\,\lambda^2}{\lambda^2 - 64500} \qquad (\lambda \text{ in nm}) \tag{4.8a}$$

$$\Delta n_\mathrm{o}(\lambda, c) = \left(F c_\mathrm{Ti}\right)^{0.55} \frac{0.8\,\lambda^2}{\lambda^2 - 80660} \tag{4.8b}$$

with fitting parameters $E = 1.2 \times 10^{-23}\,\mathrm{cm^3}$ and $F = 1.3 \times 10^{-25}\,\mathrm{cm^3}$.

Different values for the diffusivity of titanium into lithium niobate can be found in the literature. Tab. 4.4 gives an overview of diffusion coefficients at a temperature of 1060 °C.

Table 4.4.: Diffusion coefficients of titanium (given in $\mu\mathrm{m^2/h}$) in lithium niobate at 1060 °C, parallel to the crystal axes

	$\parallel X$	$\parallel Y$	$\parallel Z$
Caccavale et al. [61]	0.89	–	1.3
Fukuma et al. [62]	–	6.26	0.96
Luedtke at al. [58]	–	–	0.57

Besides the advantages mentioned above, titanium-indiffused waveguides in CLN are known to show a strong photorefractive effect [3]. To avoid the photorefractive damage, the crystals have to be heated to approx. 180 °C during device operation. Since MgO-doped lithium niobate shows a greatly reduced photorefractive sensitivity in the bulk, part of this work will address the question if this also holds true for Ti waveguides in this material. Experimental details will be presented in the following chapters.

4.2.2. Zinc-indiffused Waveguides

The use of zinc for waveguiding application (in $LiTaO_3$) was first reported by Eknoyan et al. [63]. Successful waveguide fabrication in lithium niobate using indiffusion of Zn vapour (Herreros et al. [64]), of zinc oxide (Young et al. [65]), and of metallic zinc (Ming [66]) has been reported.

The diffusivity of zinc is known to be much higher than that of titanium. A lower diffusion temperature can therefore be chosen. The waveguides fabricated in the course of this work were all diffused at a temperature of 900 °C. Table 4.5 shows some diffusivity values found in the literature, including a value for metallic zinc obtained during previous investigations in our work group of planar zinc waveguides [67].

Schlarb et al. [68] derived a Sellmeier fit for the index of refraction depending on the Zn concentration, similar to Eq. (4.2). The result for the index increase compared with undoped CLN is

$$\Delta\left(n_i^2\right) = \frac{A_{\mathrm{Nb_{Li}}}\left(c_{\mathrm{Nb_{Li}}} - 1\right) + A_{\mathrm{Zn},i}\, c_{\mathrm{Zn}}}{\lambda_{0,i}(T)^{-2} - \lambda^{-2}} \tag{4.9}$$

where

$$c_{\mathrm{Nb_{Li}}} = \begin{cases} \frac{c_{\mathrm{thr}} - c_{\mathrm{Zn}}}{6.5\,\mathrm{mol\%}} & c_{\mathrm{Zn}} < c_{\mathrm{thr}} \\ 0 & c_{\mathrm{Zn}} \geq c_{\mathrm{thr}} \end{cases}$$

$$c_{\mathrm{thr}} = \frac{50\,\mathrm{mol\%} - c_{\mathrm{Li}}}{1.5\,\mathrm{mol\%}}\, 6.5\,\mathrm{mol\%}$$

The concentrations have to be given in mol%. A value of 6.5 mol% is used for the threshold concentration c_{thr} in CLN. The coefficient for the oscillator term depending on c_{Zn} is $A_{\mathrm{Zn,o}} = 6.7963 \times 10^{-8}$ and $A_{\mathrm{Zn,e}} = 1.9221 \times 10^{-7}$. See also Eq. (4.2) for an explanation of the other parameters.

Table 4.5.: Diffusion coefficients (given in $\mu m^2/h$) for zinc or zinc oxide in lithium niobate at 900 °C

	$\perp Z$	$\parallel Z$	
Herreros et al. [64]	–	18.48	(vapour)
Boyd et al. [69]	10.90	–	(ZnO)
Young at al. [70]	–	2.89	(ZnO)
Hübner [67]	–	3.76	(metal)

Zinc-doped bulk CLN crystals are known to show less photorefraction compared with undoped crystals [8]. Zn-indiffused waveguides can therefore be ex-

pected to show a higher damage resistance compared with Ti-indiffused waveguides in CLN. Several authors report on second harmonic generation in Zn waveguides [71–73] and emphasise a high damage resistance of their waveguides. Again, own experimental work will be presented in the following chapters.

4.2.3. Proton Exchanged Waveguides

The third type of waveguide which has been studied in this work is the so-called proton-exchanged waveguide, which was first reported by Jackel and Rice [74, 75]. They immersed $LiNbO_3$ crystals in benzoic acid melt. Lithium atoms are replaced by hydrogen atoms during this process. A quite high extraordinary index increase of $\Delta n_e = 0.12$ with a nearly step-like depth profile, but no increase of the ordinary index could be observed. The ordinary index was later found to even decrease ($\Delta n_o = -0.04$) [76]. PE waveguides therefore cannot guide ordinarily polarised light and have a polarising effect. This is, however, no disadvantage for wavelength conversion using periodically poled $LiNbO_3$, where utilising the d_{33} nonlinear coefficient requires extraordinarily polarised light.

It has been found that the index profile of these waveguides is unstable, even several weeks after the waveguide fabrication. Yi-Yan et al. attributed this to the high proton mobility [77]. Diluting (buffering) the melt with lithium benzoate resulted in more stable waveguides, but with a reduced index increase Δn_e and a greatly reduced exchange coefficient (approx. one order of magnitude when buffering with 1 mol% lithium benzoate up to 3 orders of magnitude when using 4 mol% [78, 79]).

A number of different crystal phases, which can occur during the proton exchange process, have been identified [80, 81]. Fig. 4.4(a) shows numerous phases in dependence of the hydrogen ratio. A weak exchange leads to the so-called α-phase ($x < 0.12$) which has the same crystal structure as pure litihum niobate. A complete exchange of lithium leads to $HNbO_3$, having a cubic lattice strucure.

Fabricating α-phase waveguides directly by proton exchange requires buffering the melt with 4 mol% lithium benzoate, leading to long exchange times [78]. Another method for fabricating this type of waveguide has been published by De Micheli et al. [82]. They annealed a crystal after the proton exchange for 4 h at 400 °C. The resulting concentration profile is shown in Fig. 4.4(b). The step-like profile has changed into a Gaussian-like profile. Annealing sufficiently long will finally result in a waveguide with low Δn_e. The kind of waveguide is called "annealed proton exchanged" (APE).

The reduced photorefractive sensitivity in these kind of waveguides was discovered early [9], indicating a possible use of those waveguides at short light frequencies. A major disadvantage of PE waveguides was reported by Becker et al. [83]. Compared with Ti-diffused waveguides, the electrooptic effect was found to be significantly weaker in proton exchanged waveguides. Suchoski et

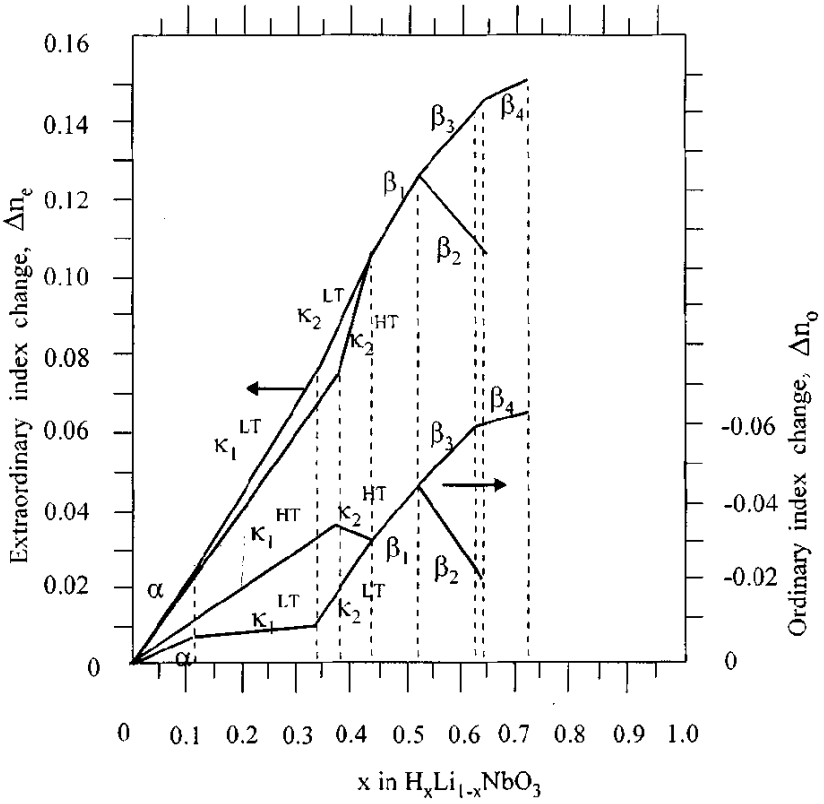

(a) Crystal phases

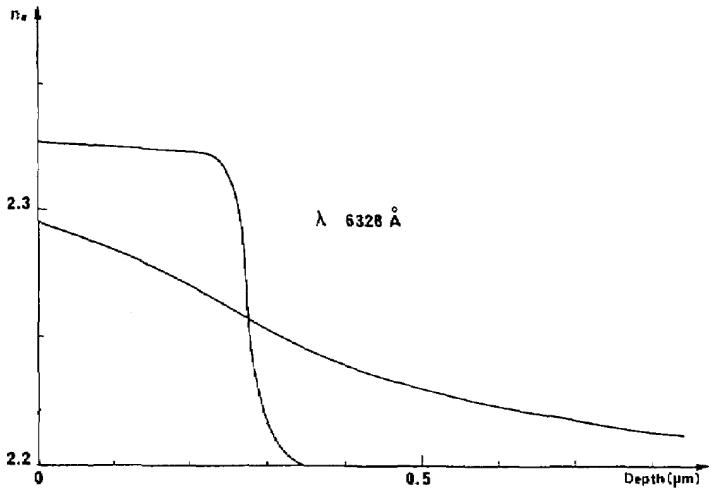

(b) c_H depth profiles

Figure 4.4.: (a) Different crystal phases identified by Korkishko et al. The change in extraordinary and ordinary indices of refraction are plotted versus the hydrogen ratio x in the compound $H_xLi_{1-x}NbO_3$ (from [81]). (b) Depth profiles of proton exchanged layers before (step-like profile) and after annealing (graded profile) (from [82])

al. examined the electrooptic effect in APE waveguides [84]. They observed no reduction of the r_{33} coefficient and concluded that α-phase waveguides are necessary for good device performance. Bortz et al. analysed the depth profile of the d_{33} nonlinear coefficient in a planar APE waveguide [85]. At depths larger than the origonal PE depth, the value was comparable to the one of pure $LiNbO_3$. The value near the surface in the initial PE region varied with annealing time, but was always lower than the bulk value.

A time- and temperature-dependent analysis of the proton exchange process of Z-cut $LiNbO_3$ in pure benzoic acid has been published by Clark et al. [86]. They obtained a diffusion constant of $1.84 \times 10^9\,\mu m^2/h$ and an activation energy of 0.974 eV. For example, this will result in a waveguide depth of $d = 0.72\,\mu m$ for a 15 h exchange at 160 °C.

An attempt to describe the diffusion of protons during the annealing step has been made by Bortz et al. [87]. Assuming a linear dependence of the change of refractive index on the concentration, they obtained from inverse WKB analyses (see [88] for an explanation of the iWKB method) an empirical model for the concentration-dependent diffusivity of H in $LiNbO_3$ for an annealing temperature of 333 °C:

$$D(C) = D_0\big(0.1 + 0.9\,\exp(-12C)\big) \tag{4.10}$$

where $D_0 = 0.55\,\mu m^2/h$ and where C is the proton concentration normalised to its initial value of the step-like profile after the exchange.

Recently, Roussev [89] published a model for the concentration-dependent planar diffusion for low concentrations (α-phase):

$$D(x) = D_0 \exp\left(\frac{1.39\,\mathrm{eV}}{k_B T}\right)\left(0.08 + \frac{0.92}{35x + 0.065}\right) \tag{4.11}$$

where $D_0 = 3.2477 \times 10^{11}\,\mu m^2/h$ and where x is the proton concentration (in the compound $H_xLi_{1-x}NbO_3$, $x < 0.12$).

He also examined the dispersion of planar waveguides:

$$\begin{aligned} n_e(\lambda)_{x=0.12} &= \sqrt{A_1 + \frac{A_2}{\lambda^2 - {\lambda_0}^2} - A_3\lambda^2} \\ n_e(\lambda, x) &= x\, n_e(\lambda)_{x=0.12} \qquad (x < 0.12) \end{aligned} \tag{4.12}$$

with

$$\begin{aligned} A_1 &= 4.945\,, & A_2 &= 0.1354 \\ A_3 &= 0.0278\,, & \lambda_0 &= 232.4\,\mathrm{nm} \end{aligned}$$

Using benzoid acid melts is not the only way for proton exhange in lithium niobate. Other hydrogen sources like, among others, stearic acid melts [90] or pyrophosphoric acid [91] have been used. However, using benzoic acid melt is a well-known and widely-used method and has therefore been chosen for this work.

4.3. Periodic Poling

4.3.1. Ferroelectric Domain Reversal

Early approaches to obtain periodically inverted domains (i. e. neighbouring areas where the spontaneous polarisation $\vec{P}_S$ has opposite sign) for nonlinear applications in $LiNbO_3$ utilised, among other methods, temperature variations during Czochralski growth [92] or indiffusion of titanium into the $+Z$ surface [93]. While crystals produced by the first method lacked of homogeneity, the latter method is not well suited for integrated optics because of the periodic surface-near index perturbation.

A method to invert a large part of the crystal simultaneously and to achieve a good homogeneity of the domain structure is the poling using an electric field. A periodic domain inversion utilising this method was first reported by Yamada et al. in 1993 [94]. They used a periodically patterned metal electrode on the $+Z$ face and a plane electrode on the $-Z$ face. High voltage pulses with an electric field exceeding the coercive field of the material were applied.

When a sufficiently large electric field is applied, the cations Li^+, having positions slightly displaced from the oxygen planes in the ferroelectric phase, move to the other side of the planes. The other cation Nb^{5+} performs a similar movement between the oxygen planes (see Fig. 4.5). This causes a reversal of the c axis of the crystal.

The externally applied field must be larger than the so-called coercive field of the crystal. For CLN, the coercive field at room temperature is $E_C \approx 21\,\mathrm{kV/mm}$. For a typical sample thickness of 0.5 mm, a voltage of approx. 10.5 kV has to be applied. Gopalan et al. [95] report on domain reversal measurements, where they discovered a built-in internal coercive field of approx. $3\,\mathrm{kV/mm}$ magnitude, leading to an asymmetric hysteresis loop (see Fig. 4.6). The forward poling field is larger than the reverse poling field. This effect, although not as strong as described by Gopalan et al., was also observed in own reversal experiments.

The domain inversion takes place in several stages [96]. Fig. 4.7 shows a sketch of a crystal where the voltage is applied using a periodically patterned electrode grating. The domain nucleation starts at the edges of the electrodes, where the electric field strength is highest. The new spike-like domain propagates quickly through the crystal in Z direction. After that, these domains grow laterally until they merge and form plane domain walls. This horizontal domain wall motion is slow compared to the vertical one.

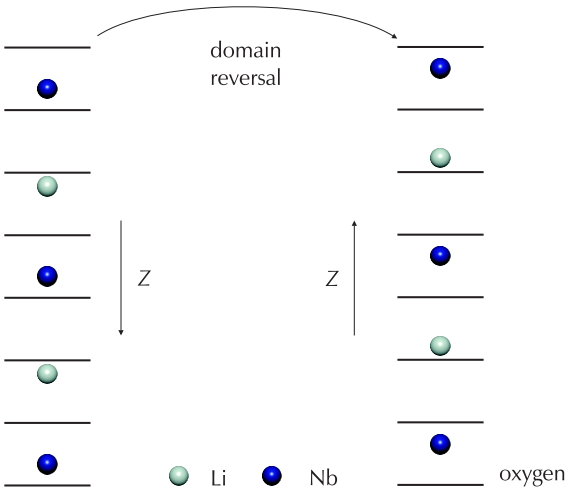

Figure 4.5.: Two directions of $\vec{P}_s$ are possible due to displacement of cations along the Z axis (depiction is not to scale)

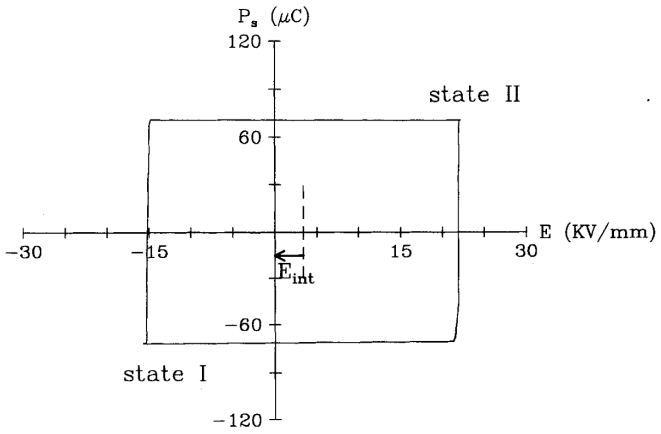

Figure 4.6.: Hysteresis loop of a 0.5 mm thick Z-cut CLN single crystal at room temperature (from [95])

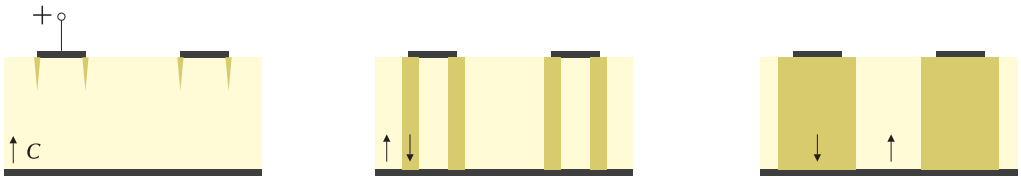

Figure 4.7.: Different stages during domain reversal: (a) Nucleation of domain reversal at the edges of the electrodes. (b) Fast propagation in Z direction. (c) Slow domain wall motion in X direction.

4.3.2. UV-light-assisted Poling in MgO:CLN

In earlier work, the standard poling method described above was also applied to MgO-doped lithium niobate. Lee et al. managed to fabricate a periodic domain structure in MgO-doped lithium niobate [97]. However, they mentioned that a homogeneous regular domain pattern could only be achieved for limited areas of the sample surface.

Fujimura et al. [98] discovered a new method for poling MgO-doped lithium niobate. They contacted a crystal homogeneously and illuminated the $-Z$ face with periodically patterned UV light. After applying a voltage ramp up to 3 kV, they observed a homogeneous periodic domain pattern on the $-Z$ surface (see Fig. 4.8). This was explained by a reduction of the coercive voltage under UV illumination. It was also noticed that the domain nucleation started on the $-Z$ face, in contrary to the usual case where no illumination is done.

A possible explanation for the reduction of the coercive voltage has been given by Wengler et al. [99]. According to them, in MgO-doped lithium niobate the UV light is able to recharge pinning defects, which can otherwise frustrate the domain inversion.

This new method promises domain gratings of very good homogeneity over large areas, leading to long nonlinear interactions lengths. See Section 5.2.2 for an explanation how the UV-assisted poling was performed in this work, experimental results will be reported on in Section 6.2.

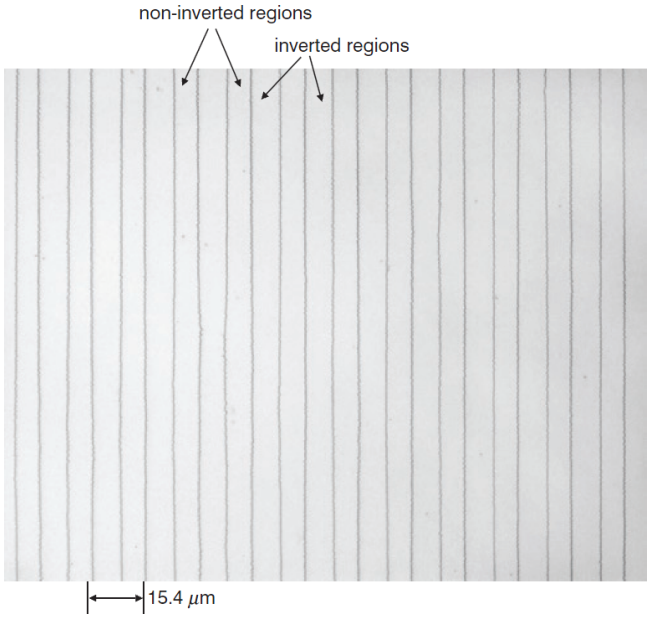

Figure 4.8.: Domain-inverted grating on $-Z$ surface after etching (from [98])

5. Experimental Setups and Measurement Techniques

This chapter describes the experimental aspects of the topics presented in Chapter 4. The chapter starts with a detailed description of the different processing steps which are necessary for the fabrication of periodically poled channel waveguides. In the first part, two methods (etching and lift-off) for the preparation of metal stripes (which are then indiffused at high temperatures or can be used as mask material for the proton exchange) are presented as well as a method of introducing hydrogen into the crystal at low temperatures (proton exchange).

The second part focuses on the inversion of ferroelectric domains. The well-known electric field poling of $LiNbO_3$ will be described and a new method, which facilitates poling in MgO-doped material ("light-assisted poling").

The chapter closes with a description of the measurement setups for second harmonic light and for the photorefractive sensitivity.

5.1. Waveguide Fabrication

5.1.1. Fabrication of Ti-diffused Waveguides

The preparation of titanium stripes on the crystal surface is shown in Fig. 5.1. The first step is the deposition of a titanium layer by e-gun evaporation. The photo resist on the surface is structured using photolithography. The resist is illuminated through a chromium mask, having the desired structure layout. After that, the exposed areas are removed by a developer. The titanium is removed by etching at the desired positions. After finally removing the photo resist with acetone, only the metal stripes remain on the surface. Those are subsequently diffused into the substrate.

The following parameters are usually used: in undoped congruent material, 7 µm wide and 98 nm thick titanium stripes are indiffused for 8.5 h at 1060 °C. In 5 mol% MgO-doped CLN, indiffusion of $\approx$ 117 nm thick stripes for 15…16 h at 1130 °C yield low-loss waveguides [100].

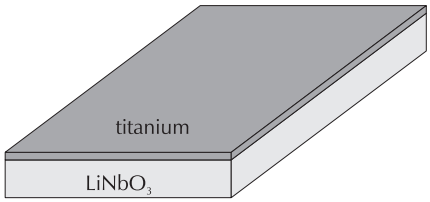

(a) Evaporation of metallic titanium

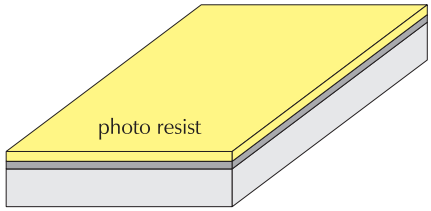

(b) Spin coating of positive photo resist

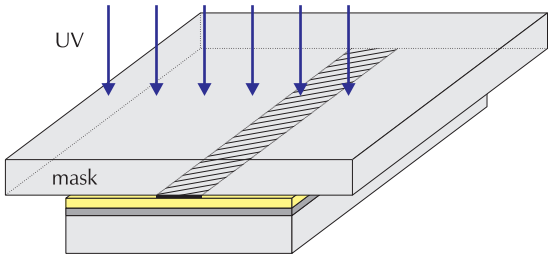

(c) Exposure through chromium mask

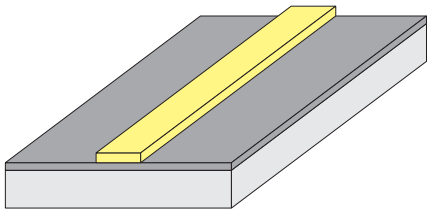

(d) Development

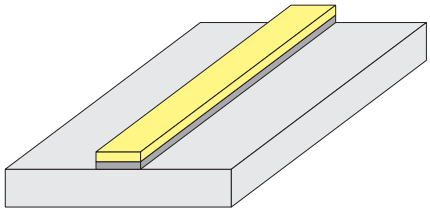

(e) Wet etching of titanium

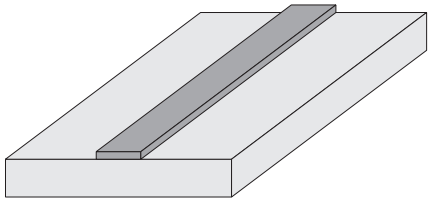

(f) Removal of photo resist

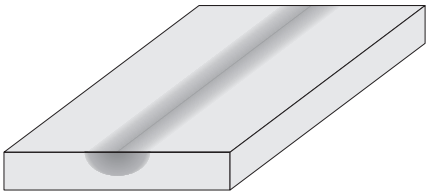

(g) Indiffusion of titanium stripes

Figure 5.1.: Steps for fabricating Ti-diffused channel waveguides

5.1.2. Fabrication on Zn-diffused Waveguides

The fabrication method chosen for this work was the indiffusion of metallic zinc, because the well-developed technology for the fabrication of titanium stripes can be adopted for this waveguide type.

However, it turned out that using the etching method, only rough sidewalls of the Zn stripes could be achieved and the etchant frequently got between the photo resist and the metal layers, leading to an inhomogeneous layer thickness [101].

Therefore, the lift-off method was chosen. Its steps are depicted in Fig. 5.2. First, image reversal resist (positive photo resist with an admixture of imidazole) is spin-coated on the lithium niobate substrate. The resist is exposed as usual. After a reversal baking step, the previously illuminated areas are now insensitive to light. Flood exposure and developing therefore lead to a resist structure consisting of the negative image compared with the chromium mask structure. For more information about image reversal lithography, see e. g. [102] and references cited there. Metallic zinc is now evaporated onto the resist structure. Because of the negative slope of the resist side walls, the resist can easily be removed using acetone. Only metal stripes remain on the sample surface. These can now be indiffused. The waveguides fabricated in the course of this work were all diffused at a temperature of 900 °C.

5.1.3. Fabrication of APE Waveguides

As already stated in Section 4.2.3, benzoic acid melt has been chosen as proton source for this work. The exchange conditions have been chosen similar to the ones reported by Parameswaran [103, 104]. A low temperature of 160 °C . . . 170 °C allows to use a quite simple setup without tight sealing because of the low vapour pressure.

Fig. 5.3 shows the setup which was used to carry out the proton exchange. It consists of an inner container, in which the actual exchange takes place, which is located in an oil bath for homogenising the temperature. The outer container ist heated by a hot plate. First of all, the benzoic acid is heated up to the melting point. The melt is stirred to ensure homogenisation. A sample holder made from quartz glass, in which the samples are kept vertically and are supported only at the ends, is suspended by a platinum wire above the melt. The melt is heated up to the desired temperature and the sample holder is immersed into the liquid. A Pt100 temperature sensor is attached to the inner glass container to allow for temperature stabilisation using a PID controller. After the desired exchange time has passed, the sample holder is pulled out of the melt and the setup is cooled down. The samples can be cleaned with solvents (ethanol, aceton) from acid residues.

After etching away the metal mask, the crystal is annealed in a platinum box inside a three-zone furnace at 330 °C.

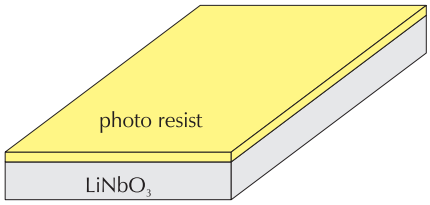

(a) Spin coating with image reversal resist

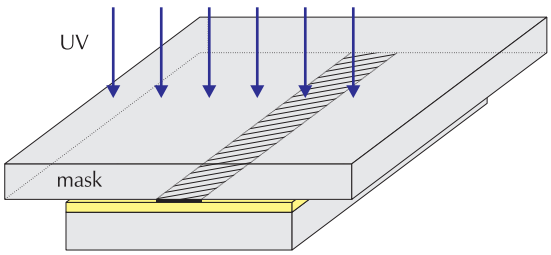

(b) Exposure through chromium mask

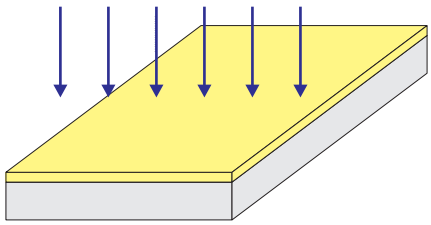

(c) Reversal bake and flood exposure

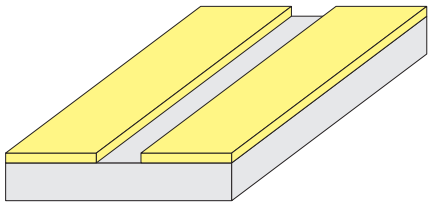

(d) Development

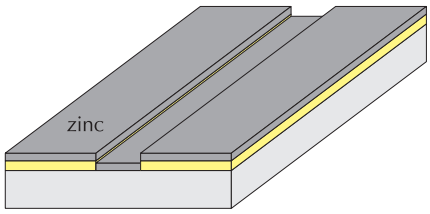

(e) Evaporation of metallic zinc

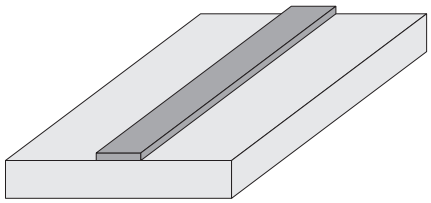

(f) Removal of photo resist

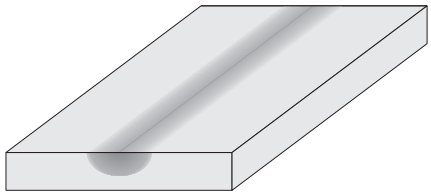

(g) Indiffusion of zinc stripes

Figure 5.2.: Steps for fabricating Zn-diffused channel waveguides

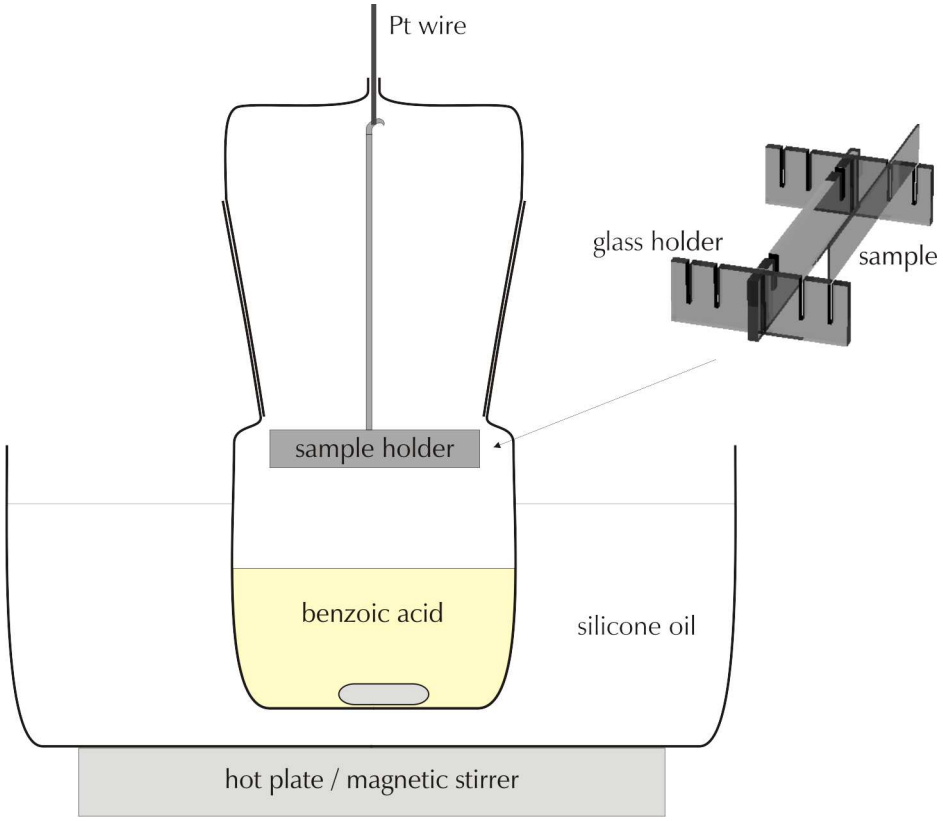

Figure 5.3.: Setup for proton exchange

5.2. Periodic Poling of Lithium Niobate Crystals

5.2.1. Common Procedure

Fig. 5.4 shows the necessary steps for preparing a periodic domain reversal. After waveguide fabrication, a shallow domain inverted layer exists on the $+Z$ side. This has to be removed by grinding. After a reversal of the bulk crystal, the waveguides are now on the $+Z$ side, where domain nucleation usually starts. A periodically patterned photo resist structure is fabricated by lithography. The crystal is now electrically contacted using liquid electrodes (a saturated solution of LiCl in isopropyl alcohol has been used). Silicone O-rings are used for sealing. The outer part of the sample holder is filled with diffusion pump oil to prevent arcing (see Fig. 5.5(a)). A sketch of the electric circuit is depicted in Fig. 5.5(b). The necessary voltage is generated by a computer-controllable high voltage supply. The voltage across the sample can be monitored by a 1:2000 voltage divider (R_D, R_V). The current through the sample is measured using a switchable shunt resistor (R_I). Both outputs are connected to an A/D converter card in a standard PC. During the poling process, the current is integrated and the accumulated

charge is calculated. The current is kept constant by the HV supply. When the desired charge value Q_{pol} is reached (i. e. the desired surface area has been domain inverted), the poling process is stopped.

The charge Q_{pol} can be calculated from the sample surface area A, which is to be domain inverted, and the spontaneous polarisation P_{s}:

$$Q_{\mathrm{pol}} = 2AP_{\mathrm{s}} \tag{5.1}$$

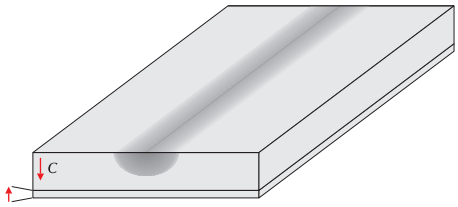

(a) Waveguide fabrication on $-Z$ face. A shallow domain-inverted layer exists on the back.

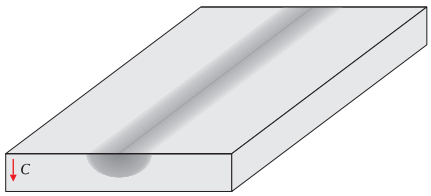

(b) Grinding

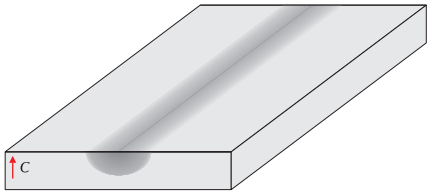

(c) Homogeneous reversal of the crystal

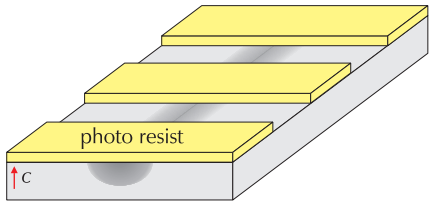

(d) Lithography of photo resist structure

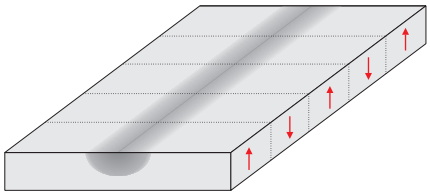

(e) Poling and removal of photo resist

Figure 5.4.: Process steps for periodic poling

5.2.2. UV-assisted Poling

The method UV-light-assisted poling—introduced in Section 4.3.2—was modified in the following way, which is depicted in Fig. 5.6(a). The sample is coated with photo resist on the $-Z$ surface. It is illuminated with a Philips TL12 UV-B lamp through quartz glass windows in the sample holder. The photo resist is partially absorbing the UV light (see Fig. 5.6(b)), which leads to a higher light in-

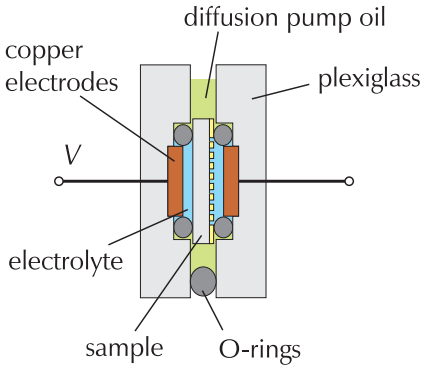

(a) Sample holder

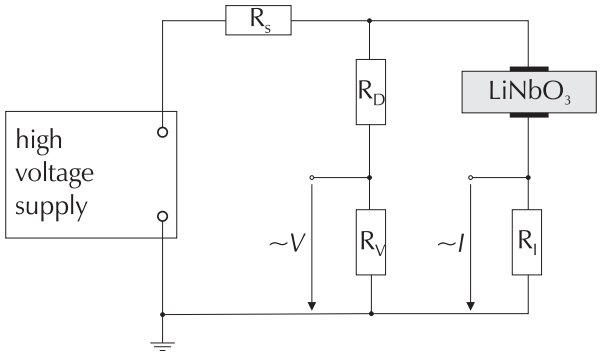

(b) Scheme of electrical circuit. $R_S = 1.2\,M\Omega$, $R_D = 1\,G\Omega$, $R_V = 500\,\Omega$, $R_I = 8\,k\Omega \ldots 55\,k\Omega$ (switchable)

Figure 5.5.: Setup for poling

tensity in the non-coated (and therefore electrically contacted) areas. The coercive field strength is periodically modulated.

The experimental results will be reported on in Section 6.2.

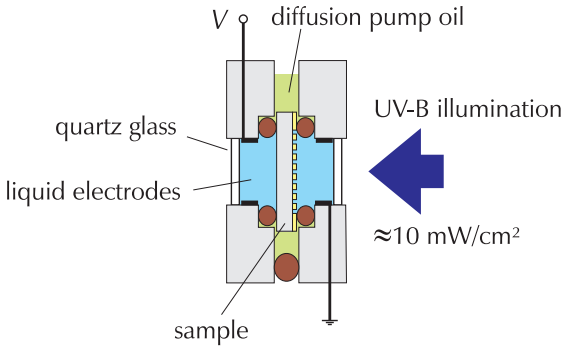

(a) Sample holder

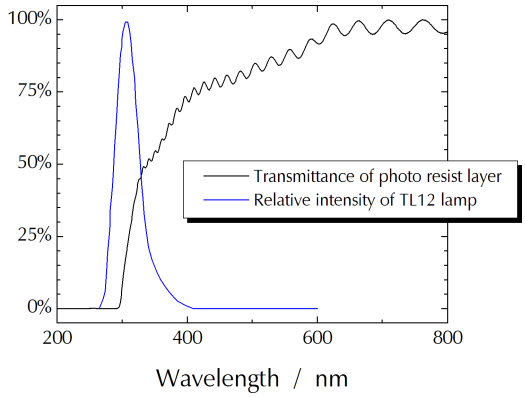

(b) Spectral transmittance of a photo resist layer (measured with a spectrophotometer) and spectrum of a Philips TL12 lamp (manufacturer data)

Figure 5.6.: UV-light-assisted poling

5.3. Characterisation Methods

5.3.1. Second Harmonic Measurements

The experimental setup used for measuring the second harmonic light which is generated in the waveguides is sketched in Fig. 5.7. Usually, short-wavelength infrared light from an external cavity laser (ECL) is coupled into a waveguide of the sample using fibre butt coupling. The light exiting the waveguide is collected using an uncoated lens and focused onto the detector. A silicon photodiode is used for measuring the power of the SH light, because it is insensitive to IR radiation with $\lambda > 1100\,\text{nm}$. A germanium diode is used to determine the fundamental power.

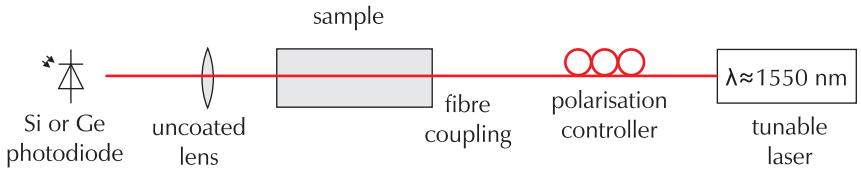

Figure 5.7.: Measurement of the power of the generated SH light and of the fundamental light

5.3.2. Photorefraction Measurements

The photorefractive sensitivity of waveguide samples has been characterised for this work using a simple method utilising a Fabry-Pérot effect. The endfaces of uncoated samples have a reflectivity of approx. 14 %, thus a resonator with low finesse is formed. This method is therefore related to the low-finesse method for measuring losses in optical waveguides, which is also utilised in this work to characterise the waveguide samples (see [105] for a detailed description of the method). If light with a short wavelength λ_{PR} propagates along the waveguide, the (effective) index of refraction n changes (for light of all wavelengths, not only for light having the PR-inducing wavelength). The index change Δn is read out using light with a longer wavelength λ_{Probe} as probe light. If Δn varies with time, an oscillating behaviour in the transmitted power can be observed (sketched in Fig. 5.8(a)).

The index change Δn can easily be calculated from the wavelength λ_{Probe}, the length L of the sample and the number of observed maxima and minima m:

$$\Delta n(\lambda_{\text{Probe}}) = \frac{\lambda_{\text{Probe}}}{2L}\, m \tag{5.2}$$

The wavelengths used here were chosen to be $\lambda_{\text{Probe}} = 1550\,\text{nm}$ (external

cavity laser) and $\lambda_{PR} = 780\,\text{nm}$ (from a laser diode or a Ti:sapphire laser), respectively, because the relevant wavelengths for wavelength conversion in the C-band (fundamental and second harmonic waves) are in this range. Only TM polarised light was used during the measurements for this work.

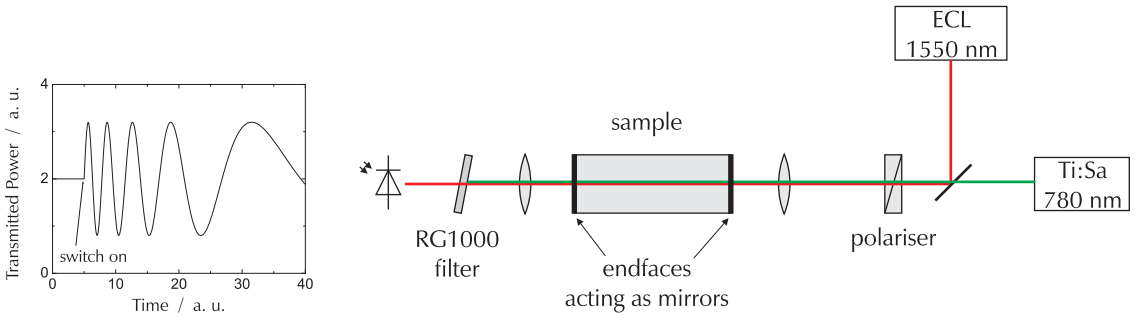

(a) Schematic plot of result (b) Experimental setup

Figure 5.8.: Measurement of the light-induced refractive index change by the Fabry-Pérot method

By illuminating the sample homogeneously with an UV-B lamp (Philips TL12), the induced index change could be erased. Photorefraction measurements performed before and after the erasing procedure yielded similar results, making this method quite reproducible.

A drawback of this method is that the waveguide usually is able to guide higher transverse modes at 780 nm. This may lead to ambiguous results depending on the coupling of the incident laser beam into the waveguide and depending on the coupling of modes while the PR-inducing light propagates through the waveguide. While the first case may lead to a different value of Δn, the second case leads to sudden changes in the oscillatory behaviour, making it difficult to judge the number of fringes m. However, the method should be accurate enough to allow at least for a qualitative comparison of different waveguide types.

6. Ti-diffused Waveguides in MgO:CLN

Two approaches for the fabrication of MgO-diffused periodically poled waveguides were adopted and are described here. The first one is the standard periodic poling of undoped Ti:$LiNbO_3$ waveguide samples and the subsequent indiffusion of a MgO layer to obtain MgO-doped waveguides (Section 6.1). The second approach is to fabricate titanium-diffused waveguides in commercially available bulk-doped $LiNbO_3$ and use the technique of UV-light assisted poling afterwards (Section 6.2).

6.1. MgO Diffusion-Doping of Ti:CLN Waveguides

The planar indiffusion of magnesium oxide into lithium niobate after titanium indiffusion has already been reported on by Caccavale et al. [106]. Their goal was a surface-near reduction of the index of refraction in order to increase the coupling efficiency from an optical fibre to the waveguide. The goal of this work was to utilise MgO post-diffusion for a possible surface-near reduction of the photorefractive effect in Ti-diffused channel waveguides by the MgO doping.

Indiffusion of magnesium oxide after the fabrication of optical waveguides and periodic poling has the advantage that the poling takes place in undoped congruent material, which is a well-established technology. The (surface-near) lateral homogeneity of the MgO concentration may also be better than in melt-doped material.

6.1.1. Titanium-diffused Waveguides

Titanium-diffused waveguides have been fabricated in four samples (Pb502z, Pb504z, Pb505z, and Pb520z). The fabrication steps for preparing titanium stripes are described in Section 5.1.1. The target layer thickness of the titanium for waveguide fabrication is usually 98 nm. The actual layer thicknesses for the mentioned four samples were in the range 95 nm … 99 nm. The metal stripes are indiffused by ramping the temperature within 1.5 h up to 1060 °C, keeping the temperature constant for 8.5 h, and cooling down in 8 h. These conditions are known to yield high-quality low-loss waveguides. The samples were periodically poled afterwards with a periodicity of 16.6 µm using the standard method described in Section 5.2.

6.1.2. Planar Diffusion of MgO into CLN

The MgO diffusion step must take place at temperatures that are low enough not to destroy the ferroelectric domain grating. A periodically poled crystal which was annealed at 950 °C showed no domain structure afterwards (after etching in a HF:HNO_3 mixture). For the diffusion experiments, a significantly lower temperature of 850 °C was chosen.

The diffusion of MgO in $LiNbO_3$ has already been investigated by Caccavale et al. [107] and Komatsu et al. [108]. They report significantly different diffusivities. The diffusion coefficients at $T = 850\,°C$ are $D = 0.234\,\mu m^2/h$ and $D = 0.135\,\mu m^2/h$, respectively. Differences between the diffusivities for diffusion into the $+Z$ and $-Z$ faces are not known from the literature, they have been assumed to be equal.

Fig. 6.1 shows the diffusion depths $d_{1/e} = 2\sqrt{Dt_{diff}}$ (assuming a Gaussian concentration profile) calculated from these diffusivities. The layer thickness τ necessary for a surface concentration c_0 of 5 mol% is also plotted. It can be calculated as follows:

$$\tau = \frac{c_0 M \sqrt{\pi}}{2\varrho}\, d_{1/e} \tag{6.1}$$

where $M = 40.32\,g/mol$ is the molar mass of MgO and $\varrho = 3.58\,g/cm^3$ is the (bulk) density.

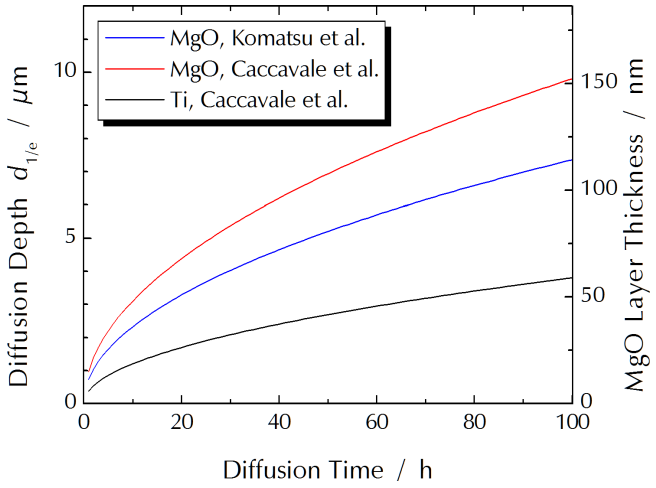

Figure 6.1.: Plotted are the diffusion depths of MgO and Ti in $LiNbO_3$ (after [106–108]) versus diffusion time for a temperature of 850 °C; additionally, the MgO layer thickness necessary for a surface concentration of 5 mol% is plotted.

Diffusion experiments of planar layers of titanium and magnesium oxide have been performed in order to study co-diffusion. The layers were deposited on a test sample (named Pb488z) as shown on Fig. 6.2. First, a titanium layer of 102 nm

thickness was indiffused for 8.5 h at 1060 °C. After that, a 60 nm thick MgO layer was indiffused for 40 h at 850 °C.

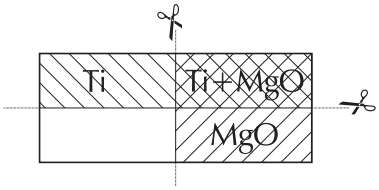

Figure 6.2.: Preparation of the sample Pb488z for SNMS

The sample was cut afterwards. In each part of the sample, a SNMS measurement (secondary neutral mass spectroscopy) has been performed. The SNMS measurements were performed at the FH Soest. The depth scale was calibrated by measuring the depth of the sputtering crater with a surface profiler (Tencor AlphaStep). Fig. 6.3 summarises important results of these investigation.

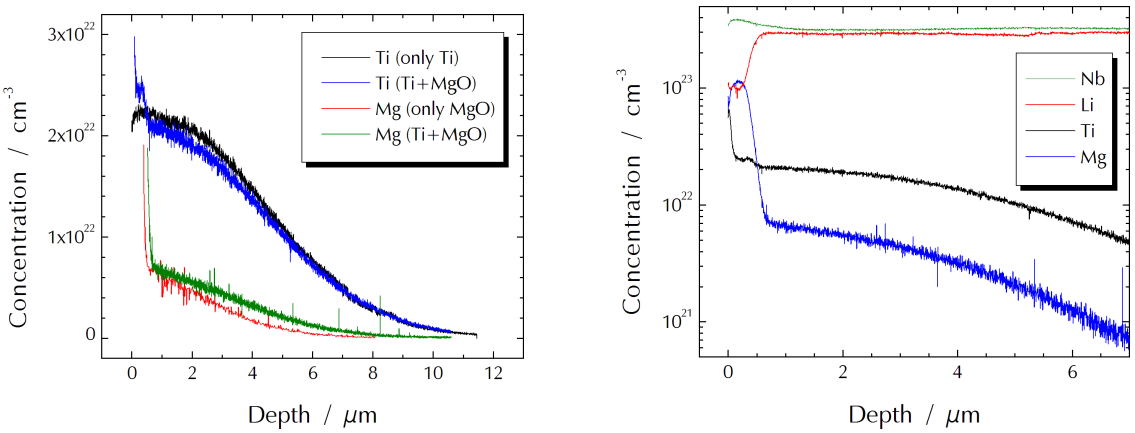

(a) Ti/MgO, different sections

(b) Ti/MgO co-diffused section

Figure 6.3.: SNMS results of the sample Pb488z. (a) Ti and Mg profiles in the different sections. (b) Ti, Mg, Li, and Nb profiles in the co-diffused section

Fig. 6.3(a) shows titanium and magnesium concentration profiles in the three diffused sections of the samples. The large peak directly below the surface is not displayed for clarity. Two things can be noticed. First of all, the Mg profile has a larger depth in the Ti-diffused section. This phenomenon was also observed by Caccavale et al. [106]. Second, the titanium concentration has increased below the surface during the MgO indiffusion.

Fig. 6.3(b) shows the concentration profiles of Li, Nb, Ti, and Mg in the Ti/MgO co-diffused section. The surface-near peaks on Nb and Ti, which were omitted in the other figure, are displayed here. The formation of a Mg-rich layer was also

reported by Bremer at al. [109] and Kim et al. [110]. The lithium profile in the Ti/Mg co-diffused part is significantly decreased directly below the surface. This might be attributed to a higher lithium outdiffusion if a MgO layer is present, as described by Lau et al. [111].

6.1.3. MgO-doped Ti:CLN Waveguides

MgO Diffusion

After fabricating the waveguides in the samples Pb502z, Pb504z, Pb505z, and Pb520z, MgO diffusion has been carried out. Each sample was cut into two parts "A" and "B". The "A" parts were used for MgO indiffusion. The "B" parts were kept as reference samples for later comparison. Table 6.1 gives an overview of the experiments which were performed. MgO layer thicknesses and diffusion times are listed.

Table 6.1.: Diffusion conditions MgO into $LiNbO_3$

sample no.	MgO thickness	diffusion time
Pb502zA	99 nm	40 h
Pb505zA	50 nm	40 h
Pb520zA	40 nm	40 h
Pb504zA	25 nm	28.5 h

For each of those samples, a MgO layer was deposited by e-gun evaporation on one half of the surface area (see Fig. 6.4). This means, after the diffusion experiments, there are optical waveguides, which are not MgO doped, but annealed a second time. This allows for examining a possible degradation of the waveguiding by the additional annealing. The optical losses of TM polarised light in the waveguides after periodical poling and before the MgO diffusion typically were measured to be $(0.10 \pm 0.04)\,{}^{\mathrm{dB}}/_{\mathrm{cm}}$.

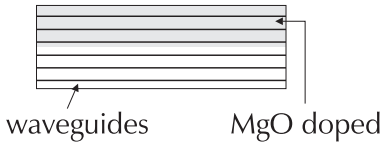

Figure 6.4.: MgO diffusion into $LiNbO_3$ waveguide samples

For the first sample Pb502zA, a 99 nm thick MgO layer was indiffused for 40 h, which should result in the desired surface concentration according to the data of Caccavale. The optical losses in the doped waveguides were unmeasurably

high using the low-finesse method. The surface of this sample was observed to be quite rough (see Fig. 6.5(d)).

Therefore, the other samples (Pb505zA, Pb520zA, and Pb504zA) have been indiffused with decreased magnesium oxide layer thicknesses. However, also in the doped waveguides of these samples, the propagation losses in TM polarisation could not be determined by the low-finesse method. In TE polarisation, the loss in the sample Pb504zA was approx. 1 $^{dB}/_{cm}$. The losses in the annealed undoped channels of this sample increased slightly to $\sim 0.19\,^{dB}/_{cm}$.

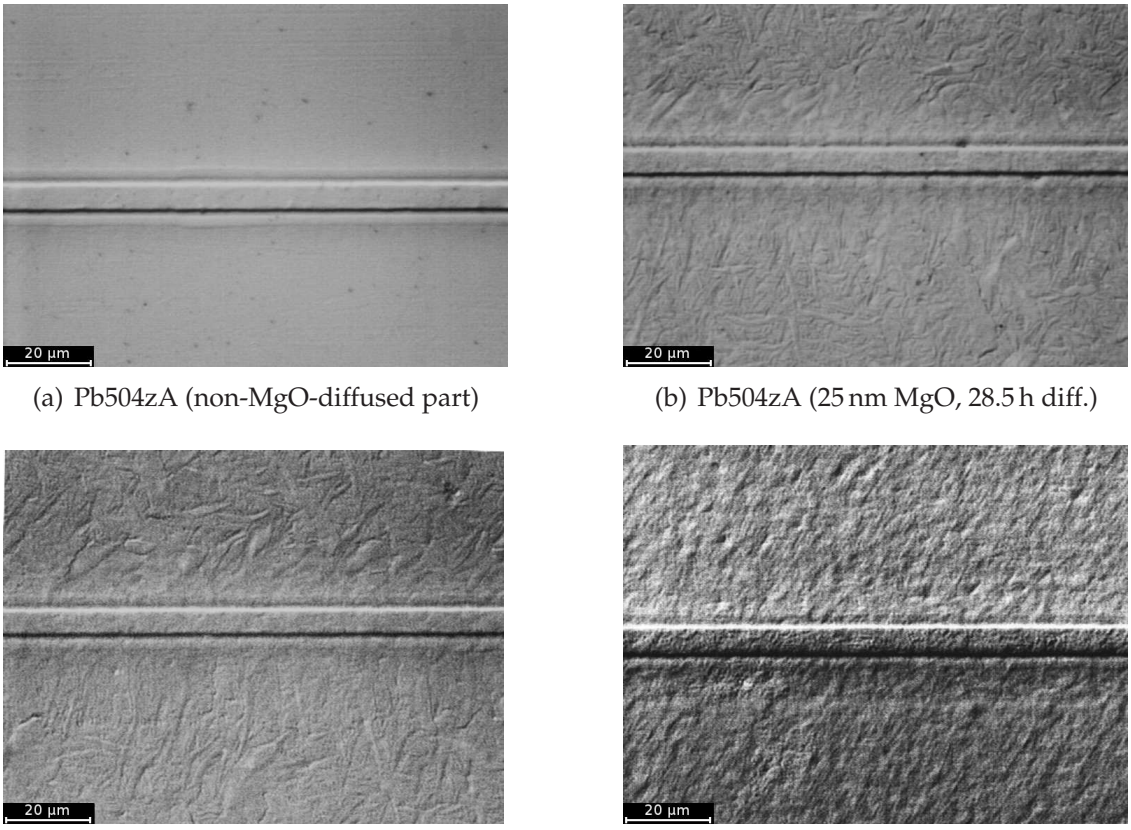

(a) Pb504zA (non-MgO-diffused part)

(b) Pb504zA (25 nm MgO, 28.5 h diff.)

(c) Pb505zA (50 nm MgO, 40 h diff.)

(d) Pb502zA (99 nm MgO, 40 h diff.)

Figure 6.5.: Surfaces of several samples after MgO indiffusion experiments

Second Harmonic Generation

Second harmonic measurements carried out using this sample are displayed in Fig. 6.6(b). The length of both samples Pb504zA and Pb504zB was 45 mm, the length of the poled areas was 36 mm. In the reference sample, the SHG efficiency is $\sim 250\,\%/W$ (if the fringes, which arise from the gap between the fibre and sample endfaces, acting as a Fabry-Pérot etalon, are not taken into account). In the

undoped annealed waveguides, the efficiency has decreased to $\sim$ 60 %/W. The FWHM of the SHG phasematching curve is 0.32 mm for the reference sample Pb504zB, which is a results of an effective interaction length of 36 mm, matching the length of the poled area. The FWHM of the SHG curve of the annealed sample Pb504zA is 0.42 mm, which is a result of an effective interaction length of 28 mm. In the doped region, only very little SH power could be measured.

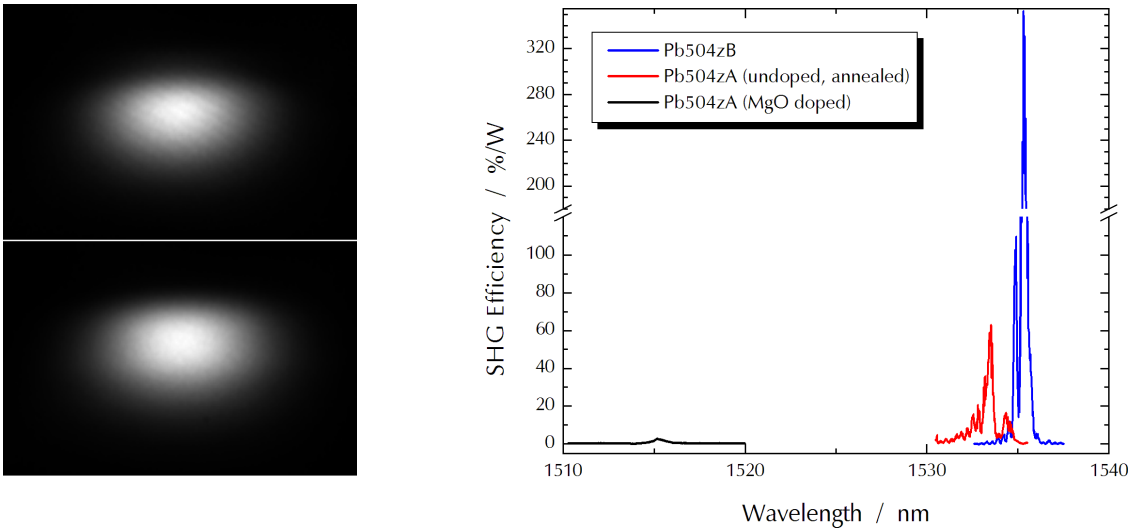

(a) Near field images

(b) Second Harmonic Generation

Figure 6.6.: Optical modes (upper image: Pb504zA undoped, FWHM $4.5 \times 3.2\,\mu m^2$; lower image: Pb504zA doped, $4.7 \times 3.5\,\mu m^2$) and second harmonic generation in samples Pb504zA and Pb504zB

A possible explanation for the lower SH efficiency in the waveguides which were annealed for 28.5 h at 900 °C is a reduced mode overlap due to the spread of the titanium by the second diffusion step. To investigate this, second harmonic generation in these waveguides has been studied theoretically. The differences between the bulk indices and the effective indices of the unannealed and the annealed waveguides were calculated using a finite element method developed by Strake [14] (software "FOCUS"). Also, the FWHMs of the intensity distributions of the optical modes at the fundamental and SH wavelengths were calculated. The overlap factor κ was calculated from the FWHMs assuming Gauss-Hermite-Gauss type field profiles. The Sellmeier equation (4.1) was used for the bulk indices. A nonlinear coefficient d_{33} of 20 pm/V was assumed. The equation system (2.18) has then been solved using the 4^{th} order Runge-Kutta method.

The resulting SHG spectra are plotted in Fig. 6.7. The shift of the phase matching wavelengths is much larger than the shift observed in the samples Pb504zB and Pb504zA. Also the SHG efficiency did not reduce by an amount which was measured in the sample Pb504zA. A degradation of the domain grating may be

possible, since the effective interaction length has been measured to be smaller than the length of the poled area. But even for a reduced length of 28 mm, the theoretical peak SHG efficiency is still 50 % of the value of the unannealed waveguide. The reduced SHG efficiency in the sample Pb504zA can therefore not fully be explained.

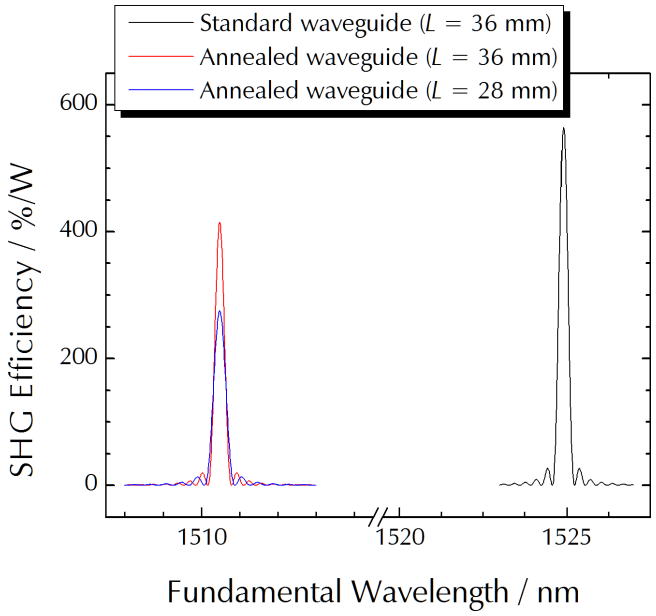

Figure 6.7.: SHG spectra calculated for standard waveguides (8.5 h at 1060 °C) and for waveguides after an additional annealing step (28.5 h at 900 °C) for two sample length 36 mm and 28 mm

The very low SH power in the doped waveguies can be explained using the results of the planar MgO diffusion experiments mentioned above. As depicted in Fig. 6.3, the Mg concentration is approx. 10 times higher in the region 0.5 µm below the surface compared with the region below that, where a Gaussian Mg profile can be observed. That means, there are two very much different materials in the waveguide region: a Mg-rich Li-Nb-Mg compound and slightly Mg-doped lithium niobate. It can be expected that the scattering losses will be higher and that the nonlinearity will effectively be lower in such waveguides.

Photorefraction measurements have not been carried out, because loss measurements, which essentially work with the same physical effect (low-finessese Fabry-Pérot, see Section 5.3.2), were not possible.

As a conclusion, none of the fabricated MgO-indiffused waveguides was suitable for use in nonlinear integrated optical devices.

6.2. UV-assisted Poling of Bulk-doped MgO:CLN Waveguide Samples

6.2.1. Channel Waveguides

Commercially available CLN crystals, bulk-doped with 5 mol % MgO, were used for the experiments presented in this section. The first poling experiments were performed using samples without waveguides. Later, two waveguide samples were fabricated. For the sample Pb60zMg5, the titanium layer thickness for the waveguides was 117.0 nm, the diffusion conditions were 15 h at 1130 °C (diffusion conditions of Ti in MgO:CLN were examined by Lee [100]). The titanium thickness for waveguide fabrication for the sample Pb61zMg5 was 116.3 nm.

6.2.2. Periodic Poling

As already explained in Section 4.3.2, the chosen method for UV-assisted poling is leveraging the photoresist layer for two purposes: providing an electrode grating (in the non-coated areas using liquid electrodes) and providing a patterning of the UV light irradiance at the surface, because the photoresist partially absorbs the light.

One experiment to confirm the results of Fujimura et al. was the periodic poling of two identical samples, which both had photoresist gratings on the $-Z$ surfaces. One sample was poled with UV illumination present, the other one was poled without light assistance. The grating period was 16.6 µm. The results (after etching for some minutes in a HF:HNO_3 mixture) are depicted in Fig. 6.8.

Several effects can be observed. The sample illuminated with UV light shows a quite homogeneous domain pattern. The other sample shows nearly no regular patterning. This could be expected because without illumination, which was the standard method so far, the domain growth starts at the $+Z$ surface. The total charge for the illuminated sample was 176 µC, which matches quite well the nominal value of 187 µC calculated for a sample area of 234 mm^2 and a domain duty cycle of 50%:50%. The measured charge for the other sample was slightly higher (226 µC). The fact that—despite the higher charge—only a very sparse domain patterning is observed can be attributed to the domain nucleation on the $+Z$ surface: that surface is electrically contacted homogeneously, so that the electric field is not spatially modulated and domain inversion can start on the whole $+Z$ surface. The flipping of the dipoles during the poling process causes a current flow. Most of the $-Z$ surface, however, is insulated in this case, which obviously prevents dipole flipping and a regular domain growth for large areas of the sample. While the voltage stayed above 2 kV for the sample poled with the standard method, the voltage dropped down to 1.25 kV (after the initial voltage peak) for the other sample (Fig. 6.8(a)). The initial voltage peak, which can be observed in

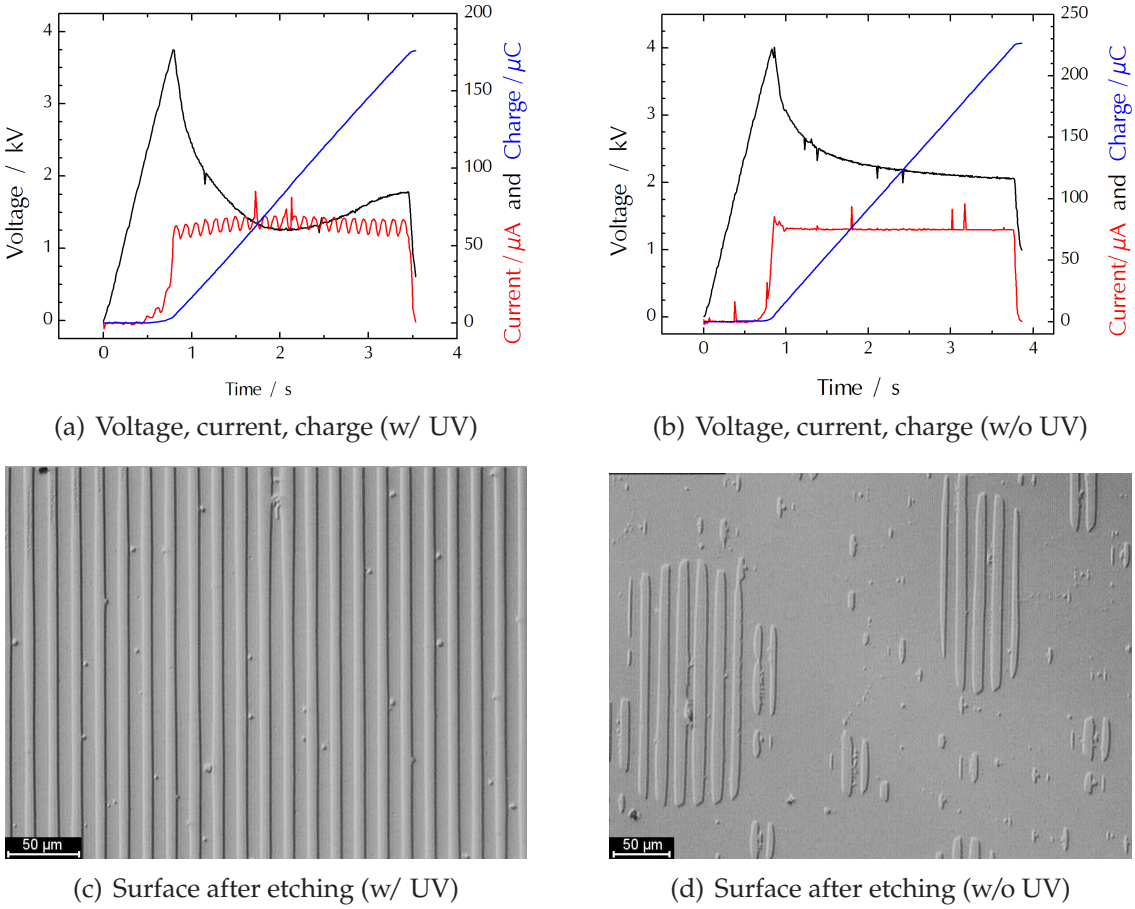

(a) Voltage, current, charge (w/ UV)

(b) Voltage, current, charge (w/o UV)

(c) Surface after etching (w/ UV)

(d) Surface after etching (w/o UV)

Figure 6.8.: Periodic poling of sample Pb54zMg5. One half of the sample was poled with light assistance (a, c), the other half without (b, d).

all poling experiments, is more pronouced for the poling of MgO:$LiNbO_3$ than for poling of undoped material. It is unknown if this has a physical reason or simply results from the setting of the maximum voltage of the high voltage supply which is used for the poing experiments. Nevertheless, the reduction of the coercive voltage by the UV illumination could be verified. The current for the illuminated sample is observed to be modulated due to an aliasing of the data acquisition time of approx. 10 ms and the 100 Hz modulation of the UV lamp intensity (2× mains frequency).

As a confirmation that domain growth really starts at the $-Z$ surface when using UV illumination, Fig. 6.9 shows another sample poled with a slightly smaller charge of 153 µC, cut perpendicular to the domain walls, polished and etched. Due to the little charge, the domains are still in the nucleation stage and only small spike-like domains can be observed (see also Fig. 4.7a).

For the next experiment, the charge was chosen to be significantly higher to im-

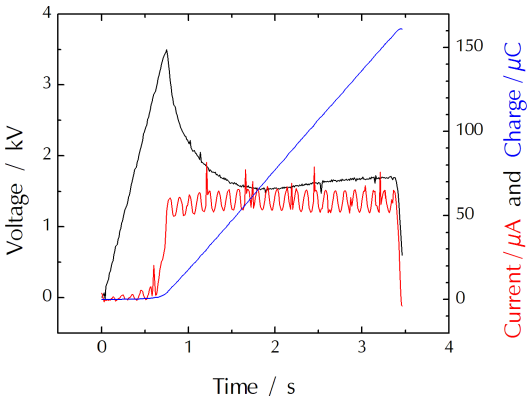

(a) Voltage, current, charge

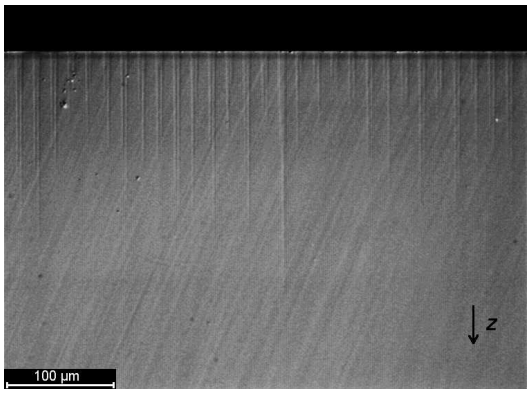

(b) Side view ‖ *Y*

Figure 6.9.: Periodic poling with UV light assistance of sample Pb48zMg5

prove the domain growth and to increase the domain depth. The sample named Pb60zMg5l was periodically poled and etched for 15 min. The results are depicted in Figs. 6.10 and 6.11.

Although the measured charge of 252 µC is higher than the expected charge mentioned above, the domains still did not grow completely in depth direction. However, the domain depth in Fig. 6.11(b) is at least 20 µm, which is sufficient for waveguide applications.

Nevertheless, for poling the next sample Pb60zMg5r, the charge again was increased. The resulting voltage, current and charge are plotted in Fig. 6.12(a). A 100 Hz notch filter was used here, so the current modulation is not visible.

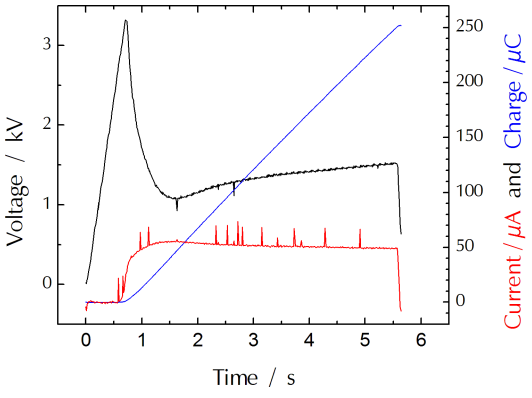

(a) Voltage, current, charge

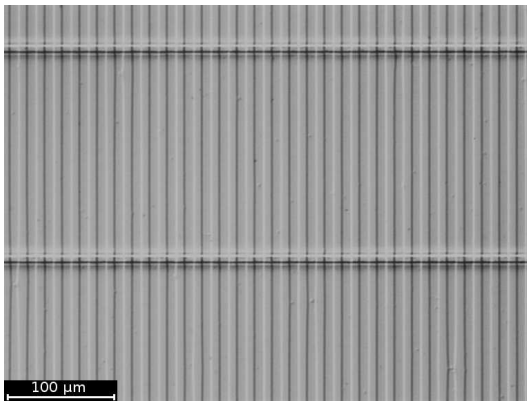

(b) Top view (‖ *Z*)

Figure 6.10.: Periodic poling (w/ UV) of the sample Pb60zMg5l. The titanium-indiffused channel waveguides are visible in (b).

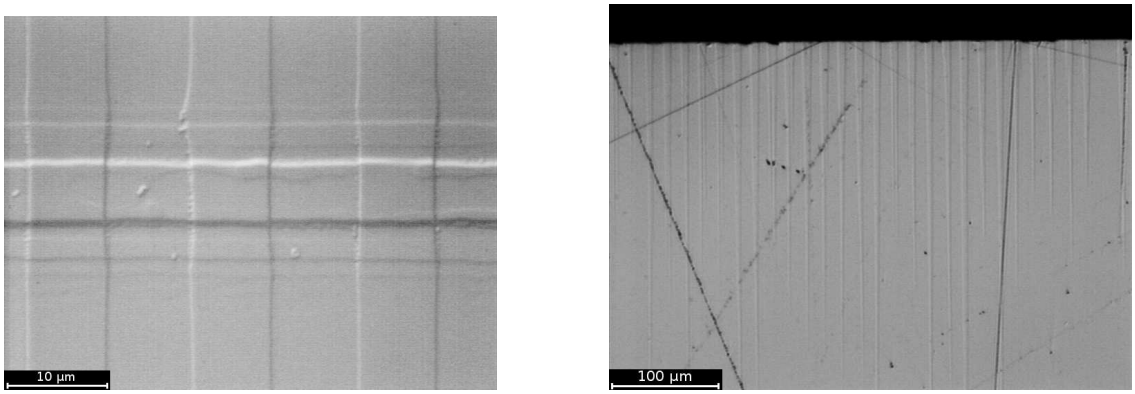

(a) Top view (zoomed) (b) Side view (‖ Y)

Figure 6.11.: Top view of etched domains and titanium-indiffused channel waveguides of the sample Pb60zMg5l, and a side view of the cut and etched sample.

The measured charge was 312 µC for this sample. The sample was etched for 2 min only to visualise and assess the domain structure (see Fig. 6.12(b)). It looks very homogeneous over a large area with a duty cycle of nearly 50%:50%. This result was considered satisfactory to try second harmonic generation experiments (see next subsection).

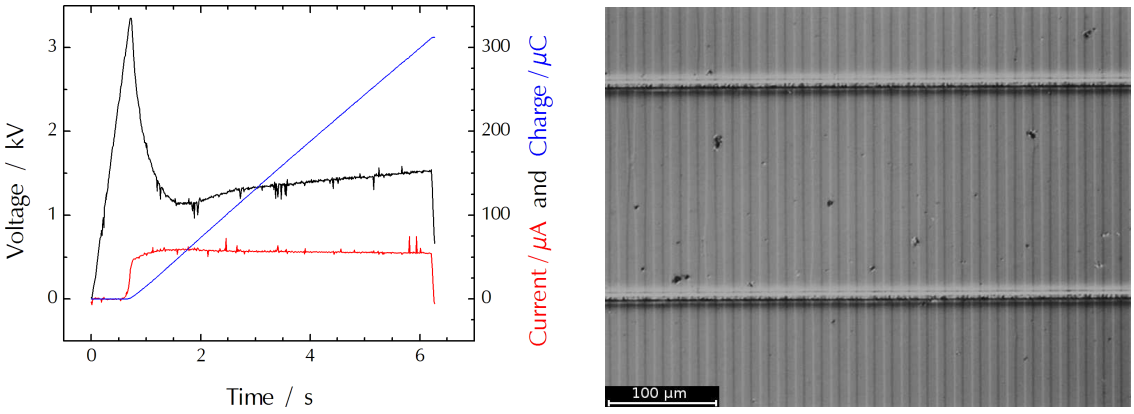

(a) Voltage, current, charge (b) Top view (‖ Z)

Figure 6.12.: Periodic poling (w/ UV) of the sample Pb60zMg5r

For the next sample, the domain period was increased to shift the phasematching condition to a longer wavelength. The sample Pb61zMg5 was poled with a period of 17.96 µm (Fig. 6.13). That periodicity was the only one available on a photomask, which was larger than 16.8 µm , and had therefore to be used.

The measured charge during the poling process was 343 µC, 1.8 times higher than one would expect for a 50%:50% duty cycle. The voltage shows a differ-

ent characteristic compared with the previous samples. The reason for this is unknown. Nevertheless, judging from the SHG results presented in the next subsection, the domain grating is of similar quality compared with the other samples.

A possible explanation for the significantly higher charge which is necessary to pole the MgO doped crystals using UV light assistance is the higher photoconductivity.

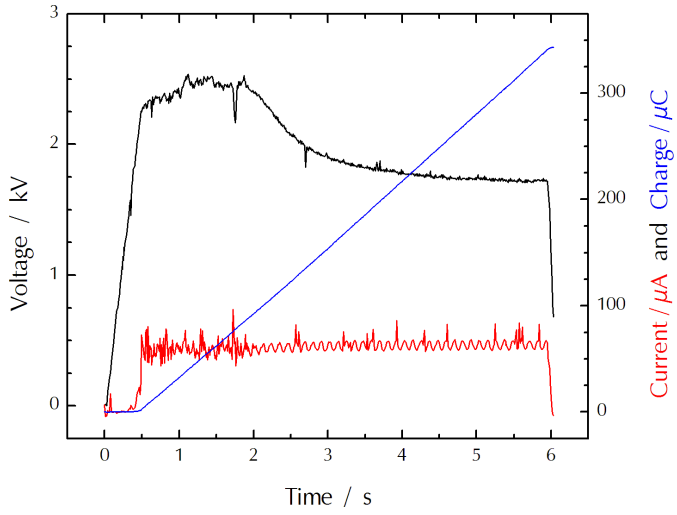

Figure 6.13.: UV light assisted periodic poling of sample Pb61zMg5 (voltage, current, charge)

6.2.3. Second Harmonic Generation

Using the sample Pb60zMg5r, second harmonic generation could be observed at quite high temperatures of $\geq 170\,°C$ at short wavelengths of approx. 1490 nm (see Fig. 6.14). The high temperature had to be chosen because that wavelength is located at the lower end of the wavelength tuning range of the ECL used for this experiment. The loss of the waveguides was measured to be approx. 1.1 $^{dB}/_{cm}$. This can be attributed to the etched sample surface (see previous section).

SHG experiments were carried out with the sample Pb61zMg5, which has a larger domain period, at different temperatures (see Fig. 6.15). The coupled fundamental power was 2.2 mW. The peak conversion efficiency was approx. 20 $^{\%}/_{W}$ ($\widehat{=}$ 2.2 $^{\%}/_{W\,cm^2}$). The loss of the measured channel was 0.47 $^{dB}/_{cm}$. The FWHM of the SHG peak can be measured to be 0.39 nm, which results in an effective interaction length of 30 mm, using Eq. (2.25). This exactly matches the length of the poled area, meaning a very good homogeneity of the waveguide. The SHG efficiency is significantly lower than the value reported above for Ti-indiffused waveguides in undoped CLN (250 $^{\%}/_{W}$ $\widehat{=}$ 19.3 $^{\%}/_{W\,cm^2}$).

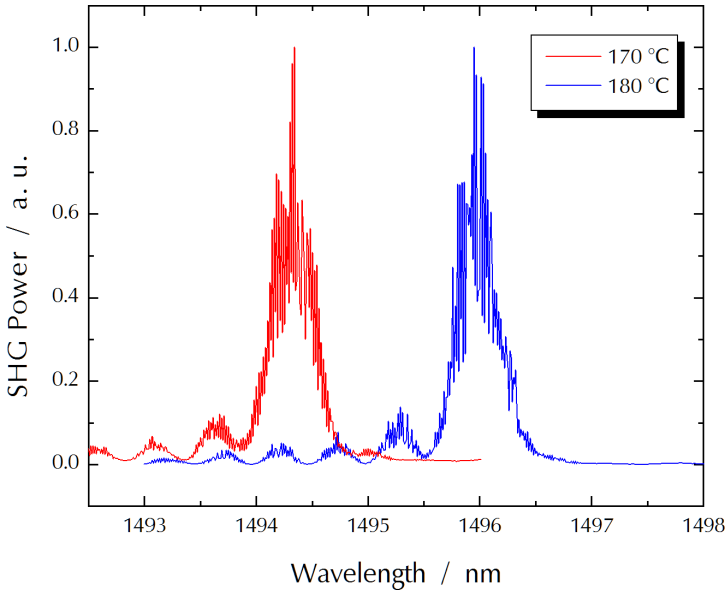

Figure 6.14.: Second Harmonic Generation using sample Pb60zMg5

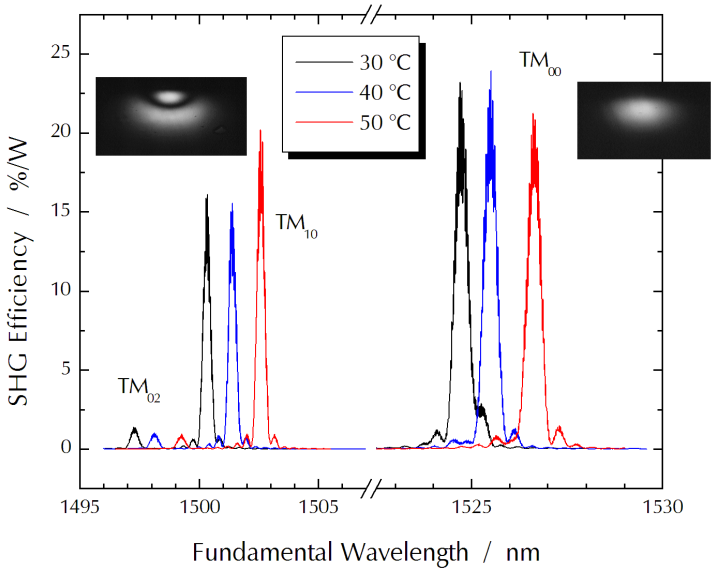

Figure 6.15.: Second Harmonic Generation for coupling to the first and second order modes (sample Pb61zMg5, channel 7b)

The dependence of the phase matching wavelength λ_{PM} on temperature T and domain period Λ can be determined using the results above:

$$\frac{d\lambda_{PM}}{dT} = 0.16\,\mathrm{nm/K}$$
$$\frac{d\lambda_{PM}}{d\Lambda} = 37.06\,\mathrm{nm/\mu m}$$

For a target fundamental wavelength of 1550 nm, i. e. the center of the C band, the resulting temperature for phase matching is 186 °C for a domain period of 17.96 µm, the required periodicity for room temperature operation is 18.63 µm, respectively.

To illustrate the phasemathing behaviour for different temperatures and different domain periods, tuning curves for 5 mol% MgO-doped lithium niobate are plotted in Fig. 6.16. Bulk MgO:$LiNbO_3$ has been used for the calculation to simplify matters. Increasing the temperature does not influence the phase matching condition strongly, so the sample has to be heated to quite high temperatures to shift the second harmonic phasematching wavelength into the range of the tunable laser. Changing the domain period, however, leads to a large shift of the SH phasematching wavelength, allowing SHG experiments at room temperature.

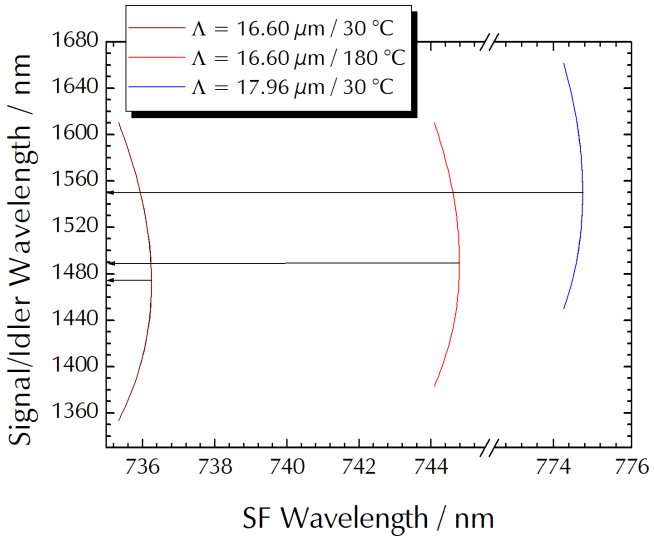

Figure 6.16.: Tuning curves in bulk MgO:$LiNbO_3$ for QPM periodicities of $\Lambda = 16.60\,\mu m$ ($T = 30\,°C$, $T = 180\,°C$) and $\Lambda = 17.96\,\mu m$ ($T = 30\,°C$). Phasematching wavelengths for SHG are indicated with arrows.

Information on titanium-diffusion in MgO:$LiNbO_3$ is extremely rare in the literature. Bulmer studied titanium indiffusion into undoped an doped Z-cut $LiNbO_3$ using only one diffusion condition [112]. The result reported there is not sufficient to set up complete diffusion and waveguide models. This makes theo-

retical modeling of this type of waveguide difficult, and the result of such simulations is of limited validity. Nevertheless, calculations were carried out treating the waveguides as Ti-indiffused waveguides in undoped CLN. Also, the FEM tool "FOCUS" developed by Strake can only calculate Ti-indiffused waveguides in undoped CLN. The Ti layer thickness and the diffusion time were determined using the relative surface index changes and diffusion coefficients reported by Bulmer and taking into account own mode size measurements of Ti:MgO:CLN waveguides. Using the differences between bulk index and effective indices as well as the mode sizes from the FEM calculation, and using the Sellmeier fit (4.2), the equation system (2.18) has been solved numerically. A nonlinear coefficient d_{33} of 20 pm/V was assumed. The result is shown in Fig. 6.17.

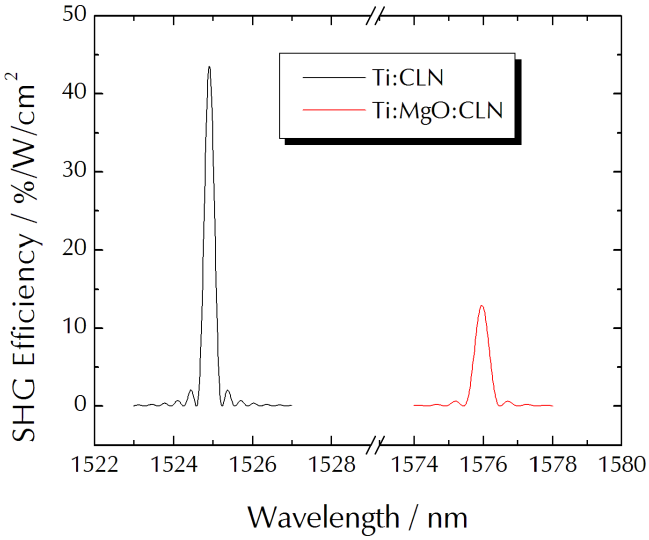

Figure 6.17.: Calculated SHG efficiencies of Ti:CLN ($L = 36\,\text{mm}$, $\Lambda = 16.60\,\mu\text{m}$) and Ti:MgO:CLN waveguides ($L = 30\,\text{mm}$, $\Lambda = 17.96\,\mu\text{m}$) at $T = 30\,°\text{C}$.

The calculated peak efficiency of the Ti:MgO:CLN waveguide is 30 % of the value obtained for the Ti:CLN waveguide. This is higher than the experimentally observed value of 11 % (see above). The reason for this is unknown. The d_{33} nonlinear coefficients in CLN and MgO:CLN are approximately the same. Another discrepancy of the calculated results is the phasematching wavelength of 1576 nm, which is larger than the obserevd value of approx. 1527 nm. An explanation is the Sellmeier equation (4.2), which is valid only for wavelengths shorter than 1200 nm. Also, the effective indices used for the calculation were probably incorrect due to the inaccurate waveguide model.

6.2.4. Photorefraction

Using the experimental setup for the Fabry-Pérot method, which has already been explained in Section 5.3.2, the photorefractive sensitivity of the Ti-diffused waveguides of the sample Pb61zMg5 (length $L = 33\,\text{mm}$) was characterised. The same experiment was conducted with a 7 µm wide waveguide in undoped congruent lithium niobate (sample Pb584zB, length $L = 42\,\text{mm}$) for comparison. The same experimental conditions (incident power of approx. 0.5 mW at 780 nm, using a laser diode as source) were used.

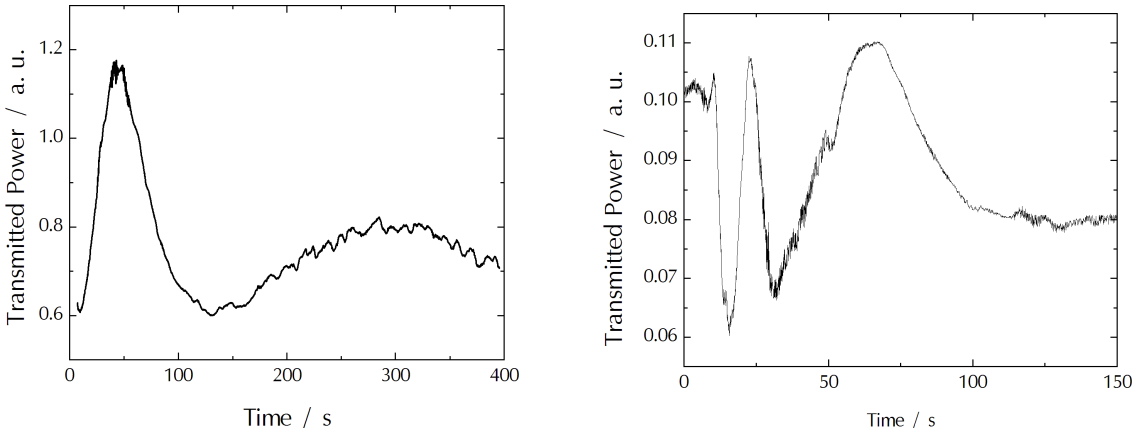

(a) P/R in sample Pb584z (b) P/R in sample Pb61zMg5

Figure 6.18.: Photorefraction in Ti-diffused waveguides in undoped CLN and in MgO:CLN ($T = 30\,°\text{C}$)

The results are depicted in Fig. 6.18. The numbers of interference fringes are $m = 1.5$ (undoped sample) $m = 2.5$ (doped sample). The refractive index changes can be calculated with Eq. (5.2) to $\Delta n = 2.8 \times 10^{-5}$ (CLN) and $\Delta n = 5.9 \times 10^{-5}$ (MgO:CLN), respectively. The resulting Δn in the doped sample is twice as high as in the undoped sample.

The result may be slightly inaccurate because of different light intensities inside the waveguide due to different mode sizes and other disadvantages of the characterisation method itself which were mentioned in Section 5.3.2. Nevertheless, a reduction of the photorefraction in MgO-doped waveguides could not be confirmed.

6.3. Conclusion

Ti:$LiNbO_3$ channel waveguides which were post-diffused with magnesium oxide have been reported on in the literature for the purpose of mode size and mode shape control. The post-diffusion technique was applied here in order to reduce

the photorefractive effect in such waveguides. However, the experiments yielded no satisfactory results. Even for a low MgO layer thickness, the Ti-diffused waveguides showed high loss and low SHG efficiency because of the Mg-rich layer near the crystal surface. Increasing the MgO diffusion temperature is no option because of the periodic domain structure. Prolonging the diffusion time might lead to usable MgO concentration profiles, but the degradation of the Ti-diffused waveguides will probably be higher because of the further diffusion of Ti into the bulk crystal and the accumulation of Ti near the surface.

In the last subsection, the periodic poling of MgO:CLN and the comparison of the photorefractive index change in undoped and MgO-doped Ti:$LiNbO_3$ waveguides was reported on. A new simple "semi-quantitative" measurement technique to characterise the photorefraction was presented. As a conclusion, Ti-diffused waveguides in bulk-doped MgO:CLN can, according to the results, not be considered to be a suitable candidate for high-power nonlinear optical waveguide devices. A reduced photorefraction in Ti-diffused waveguides could not be confirmed in this work. However, the such reduction of the photorefraction in MgO:CLN bulk crystals is well-known from the literature. The increased photorefraction must therefore be caused by the indiffused titanium. An explanation for this is given by Gericke et al. [3]. They report a stabilisation of Fe^{2+} centres against oxidisation in the surface region, increasing the photorefractive sensitivity.

A positive result is the successful poling of MgO:CLN using the new UV-assisted poling method, which was adapted from the one described in the literature to combine the advantages of that method and the well-established "standard" poling technique.

7. Ti-diffused Waveguides in MgO:SLN

As mentioned earlier, the photorefraction in MgO-doped (near-)stoichiometric lithium niobate bulk crystals is greatly reduced. It has to be found out if this still holds true for Ti-indiffused waveguides in this material. Also, the periodic poling of such waveguides has to be investigated.

7.1. Planar Diffusion of Titanium into MgO:SLN

Knowledge of the diffusivity of titanium in MgO-doped near-stoichiometric lithium niobate is useful for determining proper diffusion conditions for the fabrication of channel waveguides as well as for the calculation of field distributions of optical modes. Therefore, diffusion experiments in MgO(1 mol%):SLN have been performed.

Several planar waveguides were fabricated by evaporating layers of titanium on Z-cut MgO:SLN samples and subsequent indiffusion. The layer thicknesses can be found in Table 7.1. The titanium was deposited on the $-Z$ face except for sample Pb13zS, where the $+Z$ face was used. This has been done in order to find out a possible difference between the diffusivities in $+Z$ and $-Z$ directions. All samples were diffused for 19 h in argon atmosphere and 1 h in oxygen atmosphere. The diffusion temperatures can also be found in Tab. 7.1. Three different temperatures have been chosen so that the temperature-dependent diffusion coefficient can be calculated later.

Table 7.1.: Diffusion conditions for planar waveguides

Sample no.	Titanium thickness	Diffusion temperature
Pb11zS	92 nm	1100°C
Pb13zS	120 nm	1130°C
Pb14zS	120 nm	1130°C
Pb15zS	120 nm	1150°C

To examine the titanium concentration profile, SNMS (secondary neutral mass spectroscopy) measurements have been performed. Fig. 7.1 shows the resulting concentrations of the four samples plotted versus depth coordinate. As expected,

the sample which was diffused with the lowest temperature shows the shallowest titanium concentration profile. The peak concentration at the surface is similar to the samples diffused at higher temperature because of the reduced Ti layer thickness. The profiles of the two samples diffused at 1130 °C are nearly identical, so the diffusivities in $+Z$ and $-Z$ directions are assumed to be the same. As an example, a fit to a Gaussian function is also shown for the diffusion at 1150 °C. The concentration profiles do not fit perfectly to Gaussian functions, but are similar enough to allow for a determination of the $1/e$ diffusion depth with an error of $\pm 0.5\,\mu m$.

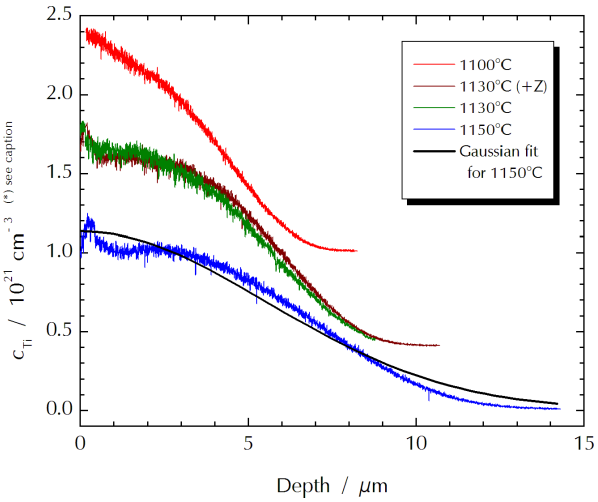

Figure 7.1.: Results of the SNMS measurement performed at four samples diffused at 1100 °C, 1130 °C and 1150 °C, respectively. (*) The curves for 1130 °C and 1150 °C have been shifted by 0.4 and 1.0, respectively, for better visibility.

By fitting the concentration profiles to Gaussian distributions, the diffusion depths d can be obtained. The diffusion coefficients can then be calculated according to $D = d^2/4t_{\text{diff}}$ (see page 31). Plotting these values in an Arrhenius plot yields values for the diffusion constant $D_0 = 1.10 \times 10^{13}\,\mu m^2/h$ and the activation energy $Q = 3.72\,eV$ (Fig. 7.2). The figure also contains for comparison the Arrhenius plots for titanium diffusion into undoped Z-cut CLN (after [61] and [62]) and SLN (after [113]). The error bars are calculated for an error in the determined diffusion depth of 0.5 µm. The diffusivity of titanium into MgO:SLN turns out to be similar to undoped SLN, but around one order of magnitude smaller than the diffusivity in CLN. This can qualitatively be explained by the smaller number of crystal defects, which facilitate the movement of indiffused ions, in the stoichiometric material.

The effective refractive indices of the guided modes of the corresponding planar waveguides have been measured using the m-line technique. This measurement technique uses a prism coupler attached to the surface of the planar waveguide (see [114] for a description of prism-coupling). Light (usually from a laser)

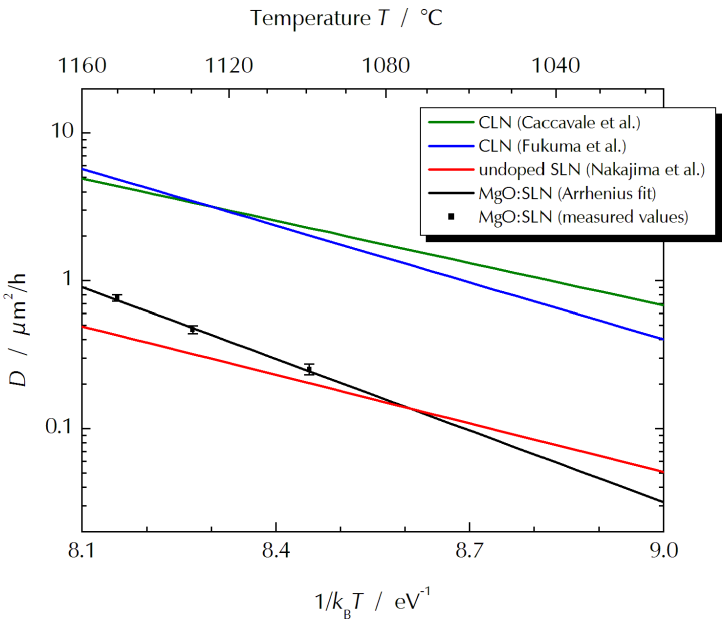

Figure 7.2.: Arrhenius plot of diffusion coefficients. Plotted are the measured values, a linear fit to these, literature values for CLN (Caccavale et al. [61] and Fukuma et al. [62]) and for SLN (Nakajima et al. [113])

which is incident on the prism can couple into the waveguide if the (effective) angular wavenumbers in propagation direction match at the interface. If a waveguide mode is excited, the effective index of the guided mode can be calculated from the angle of incidence of the laser light and from the geometry and the index of refraction of the coupling prism. This kind of measurement was performed at four different wavelengths: 532 nm, 640 nm, 790 nm, and 1064 nm. Sample Pb15zS, having the deepest titanium concentration profile, is multi-moded at all these wavelengths for both TM and TE polarisations. The depth profile of the index of refraction $\Delta n(y)$ can approximately be determined by the inverse WKB method [88]. As an example, the resulting profile of sample Pb15zS, normalised according to $(n_{\text{eff}} - n_{\text{bulk}})/(n_{\text{surface}} - n_{\text{bulk}})$, is shown in Fig. 7.3. The measured profiles fit quite well to Gaussian distributions.

A direct comparison of the refractive index profile with the titanium concentration profile allows to determine the refractive index change as function of the Ti concentration $\Delta n(c_{\text{Ti}})$. Fig. 7.4 shows this relation for a wavelength of 640 nm. Similar plots can be generated for the other three wavelengths. Both ordinary and extraordinary index change can be fitted by a straight line (dotted graphs), indicating that the dependence is almost linear for both polarisations in contrast to the corresponding functions in undoped CLN, also plotted in the figure for comparison (after [59]). The change of the ordinary index in MgO:SLN is considerably lower than in CLN, whereas the index increase of the extraordinary polarisation is of similar magnitude.

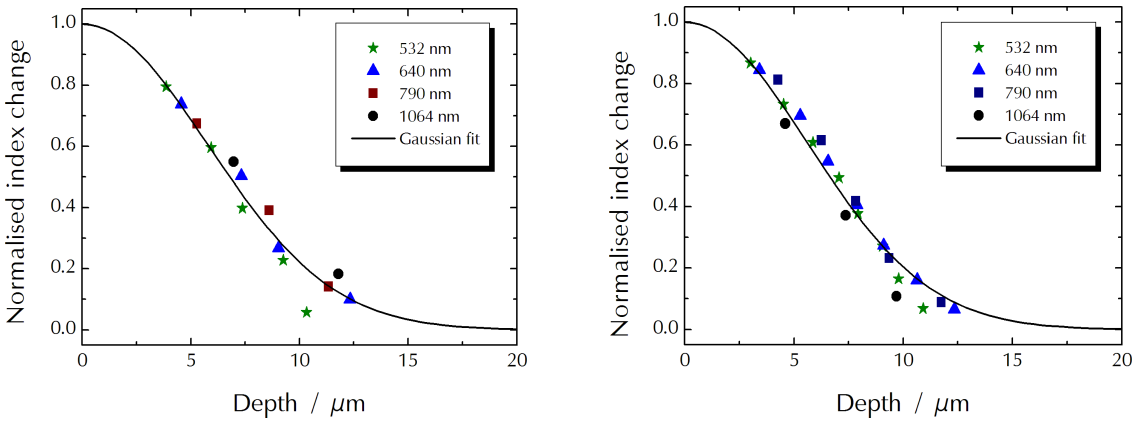

(a) Ordinary index (b) Extraordinary index

Figure 7.3.: Profiles of the indices of refraction of sample Pb15zS, normalized according to $(n_{\text{eff}} - n_{\text{bulk}})/(n_{\text{surface}} - n_{\text{bulk}})$, versus depth, reconstructed using the inverse WKB-method

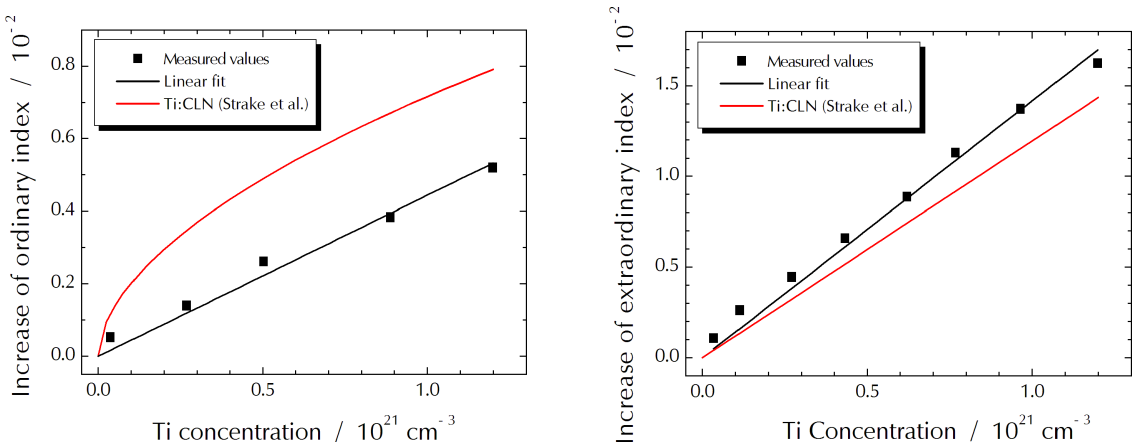

(a) Ordinary index (b) Extraordinary index

Figure 7.4.: Refractive index increase of sample Pb15zS at 640 nm wavelength. Measured values were determined by iWKB analysis.

To obtain the dispersion, i. e. the wavelength dependence of the refractive index increase, the maximum index change $n_{\text{surface}} - n_{\text{bulk}}$ was fitted to a Sellmeier oscillator term (see Fig. 7.5). Using this fit, the refractive index change can be expressed as a function of titanium concentration and wavelength:

$$\Delta n_{\text{o}}(\lambda) = 2.29 \times 10^{-14}\,\text{cm}^3 \frac{c_{\text{Ti}}\lambda^2}{\lambda^2 - 1.26 \times 10^5\,\text{nm}^2} \tag{7.1}$$

$$\Delta n_{\text{e}}(\lambda) = 9.68 \times 10^{-14}\,\text{cm}^3 \frac{c_{\text{Ti}}\lambda^2}{\lambda^2 - 9 \times 10^4\,\text{nm}^2} \tag{7.2}$$

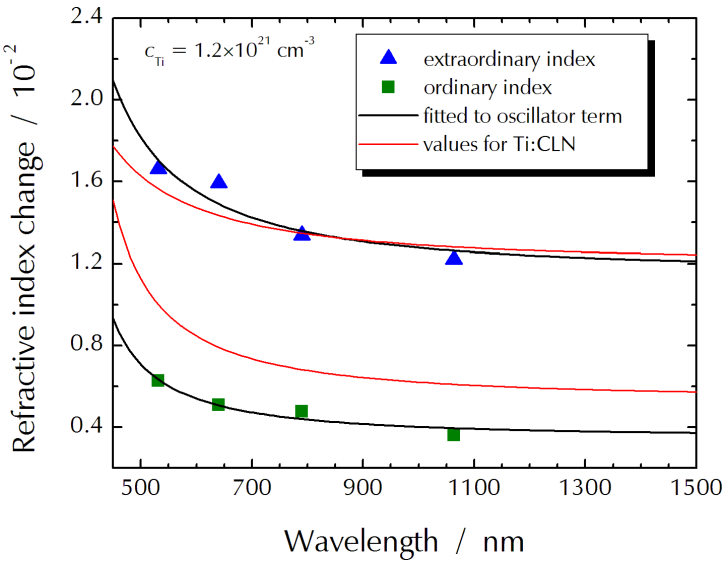

Figure 7.5.: Dependence of refractive index increase on wavelength (dispersion), for both polarisations

7.2. Channel Waveguides

Because of the similar behaviour of optical waveguiding in the extraordinary polarisation, waveguides in MgO(1%):SLN should have about the same diffusion depth as waveguides in CLN, i. e. approx. 5 µm. The best results were achieved by diffusing titanium stripes for 30 h at 1100 °C inside a platinum box. The photomask #3 (see p. 112) has been used for waveguide fabrication.

Typical optical losses of these channels were measured to be $\approx 1\,^{\mathrm{dB}}/_{\mathrm{cm}}$, the lowest obtained value was $0.5\,^{\mathrm{dB}}/_{\mathrm{cm}}$. Monomode waveguides were obtained for waveguide widths $< 7\,\mu\mathrm{m}$ and an initial Ti layer thickness of 98 nm. Fig. 7.6 shows the surface of the sample Pb16zS and the near field of the TM fundamental mode of a 7-µm-channel (FWHM 4.3 µm × 2.7 µm). The rough edges of the diffused waveguide channel result in significantly higher losses compared with those usually obtained in Ti:CLN waveguides. In TE polarisation, only weak waveguiding could be observed with a large field distribution.

Since the 7 µm wide channels were multi-moded for a titanium thickness of 98 mm, another sample Pb76zS with a reduced thickness of 70 nm was diffused. The resulting waveguides were indeed single-moded with a larger mode size of approx. $7.5 \times 5.3\,\mu\mathrm{m}^2$ measured for a 7 µm wide waveguide. The mode sizes were slightly larger for smaller channel widths and therefore still larger than in standard Ti:CLN waveguide samples. More experiments to find optimum diffusion conditions are necessary. Such experiments were, however, not carried out during this work, because other waveguide types proved to be better suited for the targeted application (see later chapters).

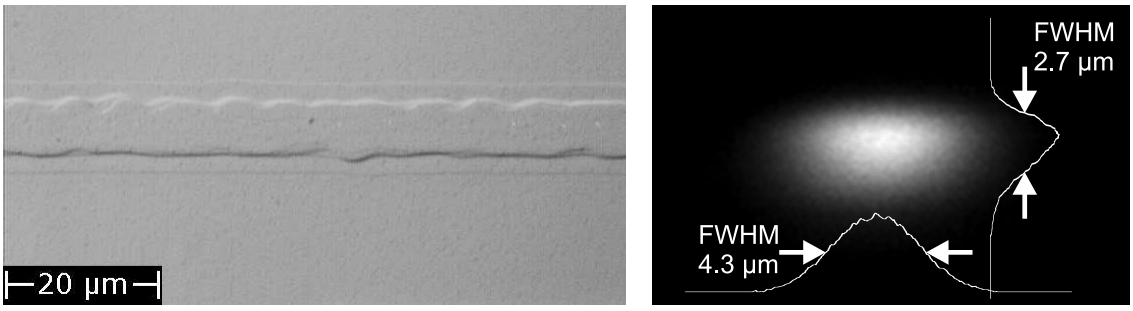

(a) Top view of sample Pb16zS (b) Near field of a 7-µm-wide waveguide

Figure 7.6.: Ti-diffused waveguide in MgO:SLN sample Pb16zS

7.3. Periodic Poling

For fabricating periodic domain structures in MgO:SLN, the method of UV-light assistance was chosen (see Sect. 5.2.2 for a description), which was already successfully utilised in MgO:CLN (Sect. 6.2.2).

For the first experiment, an identical charge as for the sample Pb61Mg5 was chosen (343 µC). The domain period was $\Lambda = 17.96\,\mu m$. The characteristics of voltage and current are plotted in Fig. 7.7(a). After an initial peak of 1.4 kV, the voltage drops to only 300 V. The initial peak is even more pronounced here than observed for MgO:CLN samples. It can also be noted that the modulation of the poling current, which arises from the modulated intensity of the UV lamp and the photoconductivity of the material, is less pronounced for the MgO:SLN samples. An explanation for this is the lower concentration of MgO, since MgO is known to cause an increase in photoconductivity [50]. Figs. 7.7(c) and 7.7(e) show top and side views of the sample Pb78zSl after etching in an HF:HNO_3 mixture. Even in the top view it is visible that poling mainly occurred at the edges of the electrodes. Most of the domains can still be considered to be in early nucleation stage because of the spike-like shape of the domains near the electrode edges (see also sketch in Fig. 4.7 on p. 37).

Because of the insufficient domain inversion, another sample Pb78zSr was poled using a significantly higher charge (setpoint increased by 30 %, measured value: 457 µm). Figs. 7.7(d) and 7.7(f) show pictures of the sample after poling. The top view now shows an improved homogeneity and duty cycle. However, the domain growth in depth direction shows no significant improvement.

The Ti-diffused waveguides are of similar quality in the two samples, although the waveguides of sample Pb78zSl appear to have a worse morphology in that particular photograph. Fig. 7.8(a) proves that also the titanium-diffused waveguides are periodically poled, since this is not clearly visible in the previous pictures (Figs. 7.7(c) and 7.7(d)). A closer look at Fig. 7.7(f) shows that the domains

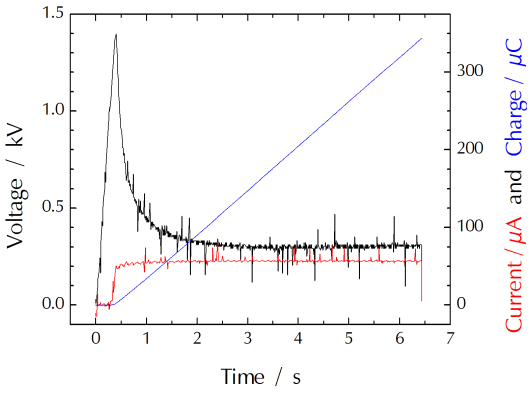

(a) Poling of sample Pb78zSl

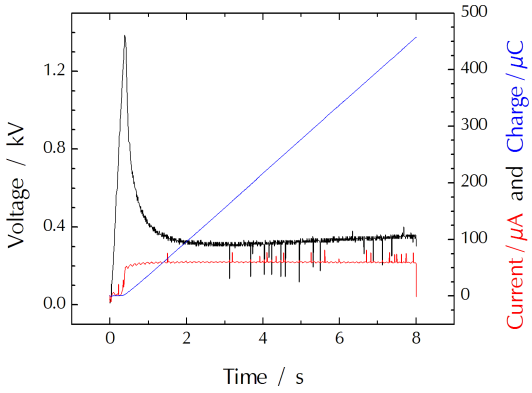

(b) Poling of sample Pb78zSr

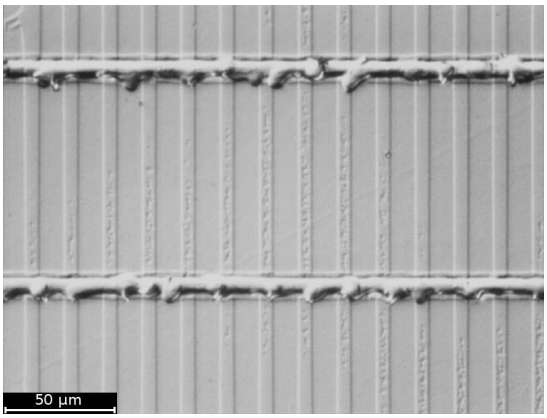

(c) Top view (‖ Z) of sample Pb78zSl

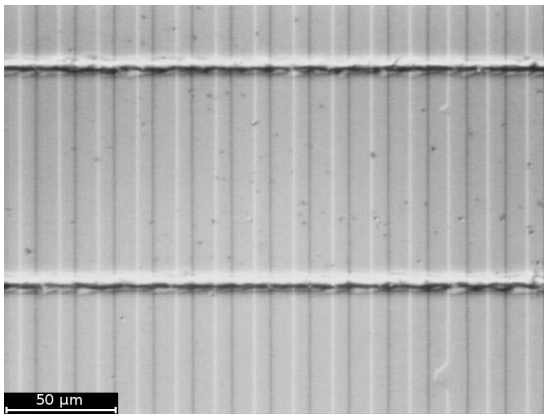

(d) Top view (‖ Z) of sample Pb78zSr

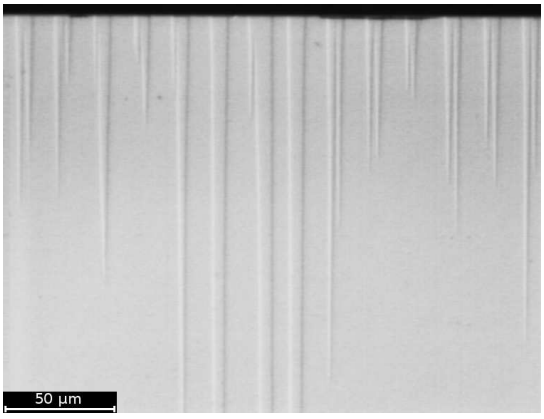

(e) Side view (‖ Y) of sample Pb78zSl

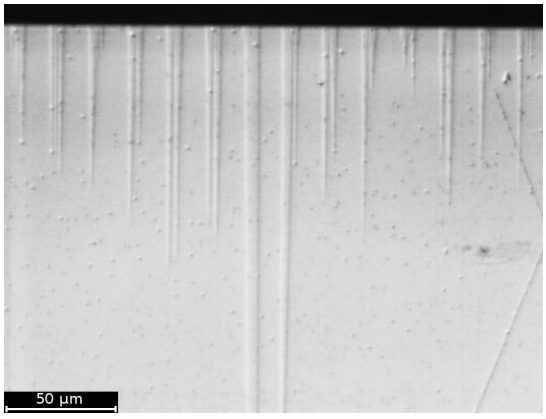

(f) Side view (‖ Y) of sample Pb78zSr

Figure 7.7.: UV-assisted periodic poling of the two parts of the MgO:SLN sample Pb78zS

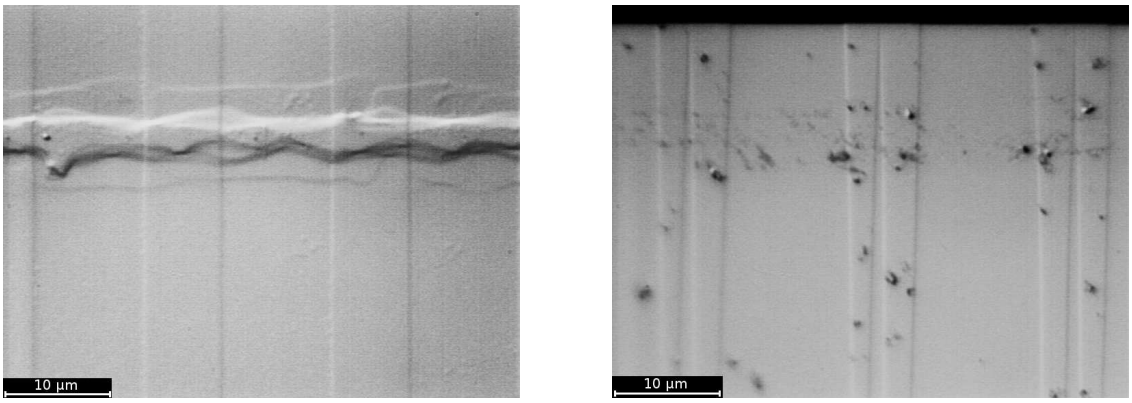

(a) Top view ($\| Z$) of sample Pb78zSr (b) Side view ($\| Y$) of sample Pb78zSr

Figure 7.8.: Details of poled samples Pb78zSr (zoomed views). (a) the Ti-diffused waveguides are periodically poled. (b) The nucleated domains did not merge (yet).

have not always merged in lateral direction below the electrode area, so there are no compact domains with a duty cycle of 50%:50% over the whole sample length. Fig. 7.8(b) shows a zoomed view of the domains of sample Pb78zSr in depth direction. Also in this sample, most domains are still in nucleation stage. This is surprising, because the measured charge is more than 20 % higher than the charge required to invert the complete sample uniformly in undoped CLN.

Nevertheless, the sample Pb76zS was poled with an identical setpoint value for the charge (see Fig. 7.9(a)). The voltage shows a slightly different characteristic for this sample and drops to only 600 V…700 V during the poling process. The reason for this behaviour and if the domain quality is influenced by this is unknown. The sample was then used for further experiments concerning second harmonic generation and photorefraction.

7.4. Second Harmonic Generation

Second harmonic generation in 6-µm-wide channels has been studied. The incident fundamental power was approx. 1 mW. The lowest loss which was measured using the sample Pb76zS was 1.1 $^{\mathrm{dB}}/_{\mathrm{cm}}$. The SHG result for this channel is plotted in Fig. 7.9(b). The maximum conversion efficiency was only $\sim$ 1.3 %/W. The FWHM of the curve is 1.2 nm, which results in an effective interaction length of 10 mm. This is significantly smaller than the length of the poled region of 30 mm, meaning a non-perfect waveguide homogeneity. Also the shape of the SH curve, which is not sinc^2-like, shows the inferior homogeneity. The low SH efficiency can mainly be attributed to the imperfect domain growth. Only for a perfect 50%:50% domain duty cycle, the effective nonlinear coefficient d_{eff} is

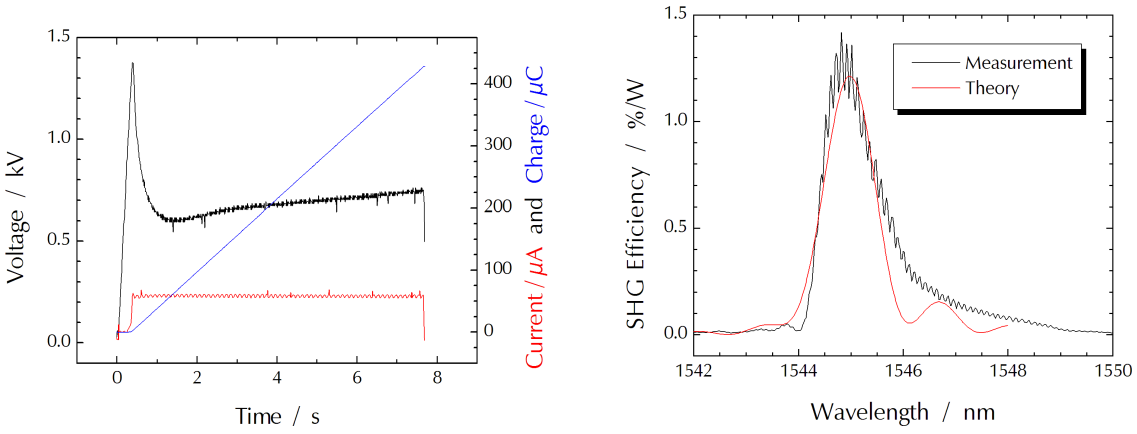

(a) Voltage, currecht, and charge

(b) Second harmonic generation

Figure 7.9.: (a) UV-assisted periodic poling of the MgO:SLN sample Pb76zS. (b) Measured second harmonic generation in an 6-µm-channel. See text for theoretical curve.

given by Eq. (2.33). If the domains have even grown incompletely and are split, as depicted in Fig. 7.8(b), d_{eff} can be expected to decrease significantly. Also, the overlap between fundamental and second harmonic modes is small, due to the larger mode size, which contributes to the lower SHG efficiency.

For this waveguide type, a theoretical SHG curve has been calculated too, to assess how much the effective nonlinearity is reduced in the measured waveguide.

Since the FEM tool developed by Strake can only calculate Ti:CLN waveguides, proper diffusion conditions for that waveguide type (to mimic Ti:MgO:SLN wabeguides) had to be determined from the diffusion conditions for the Ti:MgO:SLN samples. This should not cause a large error in the calculation since the dependence of the extraordinary index on the titanium concentration are linear for both waveguide types, and because the dispersion properties are quite similar (see Fig. 7.5). A titanium thickness of 70 nm and a diffusion time of 16 h at 1060 °C were used for the FEM calculation so that the theoretical and the experimentally measured mode sizes matched. The equation system (2.18) was solved numerically, as already explained in the previous chapter.

The shape of the measured SH curve suggests an inhomogeneity of the waveguide with a quadratic variation of $\Delta\beta$. For the calculation, a quadratic lithium concentration profile has been assumed along the sample. The concentration in the center and at the end faces have been assumed to be 49.50 mol% and 49.45 mol%, respectively, so that the shapes of the calculated curve and measured one matched as closely as possible. The waveguide inhomogeneity may, however, also have been caused by variations of Ti stripe width or thickness along the propagation direction.

Due to the imperfect waveguide model and the inaccuracy of the Sellmeier

equation (4.2) for wavelengths $> 1200\,\text{nm}$, the theoretical and actual phasematching wavelengths did not match exactly and the domain period had to be set to $17.59\,\mu\text{m}$ in the calculation.

Moreover, the sample length was set to $L = 12\,\text{mm}$ and the d_{33} coefficient was set to $6.2\,\text{pm/V}$ to obtain the curve plotted in Fig. 7.9(b). That nonlinear coefficient is approx. three times smaller than the value used in the previous chapters for a perfect domain grating having 50%:50% duty cycle.

In a recent paper from 2009, Chen et al. [115] report on second harmonic generation in Ti:MgO(2%):SLN waveguides with an efficiency of $630\,\%/\text{W}$. Their sample length was 40 mm. If the whole sample is periodically poled, this results in a length-normalised efficiency of $39\,\%/\text{W}\,\text{cm}^2$. They also report an optical loss of $0.12\,\text{dB/cm}$. Compared to these results, the waveguides presented in this work are inferior. Their waveguide fabrication technique, where they used a gas flow of wet O_2, while in this work dry argon and oxygen were used, might play a role. Wet oxygen might lead to a higher titanium diffusivity, as it was reported by Bulmer [112] for MgO-doped congruent lithium niobate. By fine-tuning the diffusion conditions and by improving the periodic domain patterning, the performance of the waveguides type presented in this work can be expected to improve.

7.5. Photorefraction

The low-finesse Fabry-Pérot method was also used here to determine the photorefractive sensitivity, using the same setup as it was used for the CLN and MgO:CLN samples. The sample Pb16zS as well as the periodically poled sample Pb76zS were measured. The resulting time-dependent transmitted powers are plotted in Fig. 7.10.

The number of fringes can be regarded as $m = 1.5$ in Fig. 7.10(a). With a length L of 16 mm, the refractive index change can be calculated from Eq. (5.2) to $\Delta n = 7.3 \times 10^{-5}$. This value is significantly higher than the value obtained in the waveguide in undoped CLN ($\Delta n = 2.8 \times 10^{-5}$), as reported in Sect. 6.2.4. The result of sample Pb76zS (same channel as for SHG measurement), assuming $m = 1$ and a sample length of 32 mm, was an index change of $\Delta n = 2.4 \times 10^{-5}$. This value is a little lower than the one obtained in Ti:CLN. However, the mode size was larger in the in the MgO:SLN sample, which reduces the intensity for a given power. Also, the loss of the Ti:MgO:SLN waveguide was higher, so the "effective interaction length" of the photorefraction-inducing light is smaller than the sample length, reducing the effect.

Again, these results may be ambiguous due to different mode excitation and different mode sizes, but a reduction of the photorefraction in MgO-doped waveguides was also not observable here.

This is in contrast to the result of Chen et al. [115]. They characterised the pho-

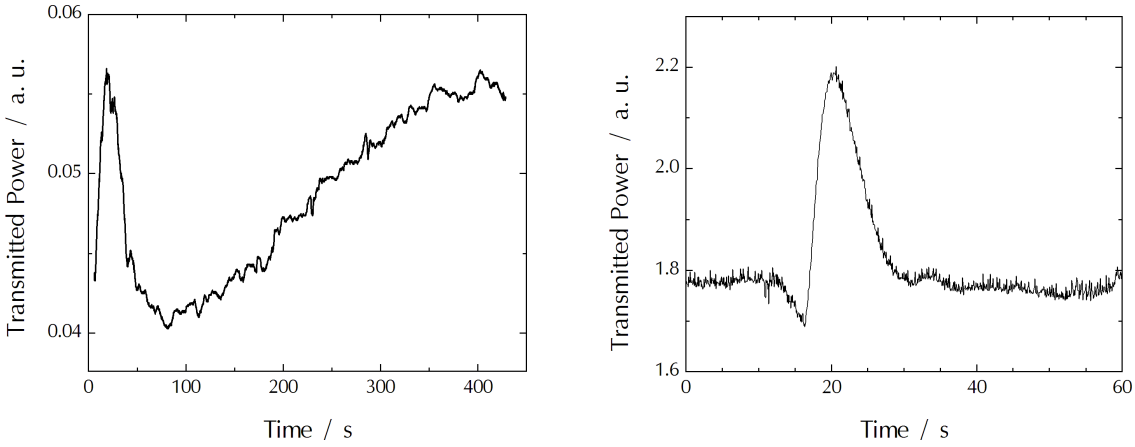

(a) Pb16zS (b) Pb76zS

Figure 7.10.: Photorefraction in a Ti-diffused waveguide in MgO:SLN samples Pb16zS and Pb76zS

torefraction by observing a shift of the SHG phasematching wavelength when light of 780 nm wavelength was launched into the waveguide, inducing photorefraction. They observed a shift of several nanometers in Ti:CLN waveguides, but nearly no shift in Ti:MgO:SLN waveguides. An explanation may be their use of wet oxygen during the titanium indiffusion, where protons can also be incorporated into the crystal. Protons are well-known to reduce the photorefractive effect in lithium niobate (see the several chapters about proton exchange in this work).

7.6. Conclusion

The first titanium indiffused channel waveguides have been fabricated in MgO-doped SLN and measurements of the photorefraction have been performed. The results have been presented during the conference ECIO 2005 [116]. Also, the periodic poling, using the UV light assisted technique, of Ti:MgO:SLN waveguides has first been performed during the course of this work.

Concluding this chapter, it can be stated that the waveguides produced during this work proved to be of lower quality compared with standard Ti:CLN waveguides. They had significantly rougher surface morphology, leading to higher optical losses. By fine-tuning the diffusion conditions, it is likely that waveguides can be fabricated which have a smoother morphology and which have an index profile providing better mode confinement and better mode overlap to increase the SHG efficiency. Further work is necessary to improve the quality of the ferroelectric domain grating. The poling technique which makes use of UV light assistance did not yield domain gratings of high quality, as it was the case for MgO-doped congruent lithium niobate. More important, the waveguides showed no

improved performance concerning photorefractive sensitivity. This is similar to the Ti:MgO:CLN waveguides reported on in the previous chapter. The explanation for the non-reduced photorefraction given there for Ti:MgO:CLN waveguides is also applicable for the Ti:MgO:SLN waveguides.

8. Zn-diffused Waveguides in CLN

Zinc-doped bulk CLN crystals are known to show less photorefraction compared with undoped crystals. It is also known that channel waveguides can be fabricated by Zn doping because the refractive index is increased, in contrast to MgO-doping. The following chapter will therefore present fabrication and properties of Zn-indiffused waveguides as well as a comparison with Ti:CLN waveguides.

8.1. Channel Waveguides

First, it was planned to use ZnO as source material for the diffusion because Young et al. reported on surface degradation when using metallic zinc [65]. The diffusion conditions were chosen to be 2 h 10 min at a temperature of 900 °C. While the temperature was chosen arbitrarily (but still similar to values reported in the literature), the diffusion time was chosen according to the diffusivity reported by Young (see Tab. 4.5) to achieve a diffusion depth of 5 µm, which is similar to Ti-diffused waveguides. Some preliminary experiments using ZnO were carried out, but they did not lead to usable waveguides. These experiments were stopped when the waveguides fabricated from metallic Zn stripes turned out to be of good quality (see below). The diffusion conditions mentioned above were also chosen for indiffusing Zn stripes.

Some first preliminary diffusion experiments of a planar zinc layer into lithium niobate as well as metal stripes with a small layer thickness of 35 nm led to waveguides guiding only visible light.

For the fabrication of waveguides targeted for wavelengths around 1550 nm, the layer thickness was significantly increased for the next sample (Pb816z) to 92 nm. The photomask #1, having waveguide widths of 5 µm, 6 µm, and 7 µm (see p. 111), was used for all Zn-diffused waveguides.

The surface of the waveguides looks quite rough (see Fig. 8.1(a)). Nevertheless, the fabricated waveguides showed low optical losses in TM polarisation of 0.12 $^{dB}/_{cm}$ (average of all measured channels), with 0.09 $^{dB}/_{cm}$ being the lowest value. No waveguiding was observed in TE polarisation. The mode sizes were approx. $10.0 \times 7.0\,\mu m^2$ measured in 5-µm-wide channels down to $9.5 \times 6.1\,\mu m^2$ in 7-µm-wide channels. Fig. 8.1(b) shows a near field image of a 6-µm-wide channel.

The large mode size is an indication of the waveguiding being too weak, i. e. too close to cut-off. The next fabricated sample (Pb845z) therefore had a slightly

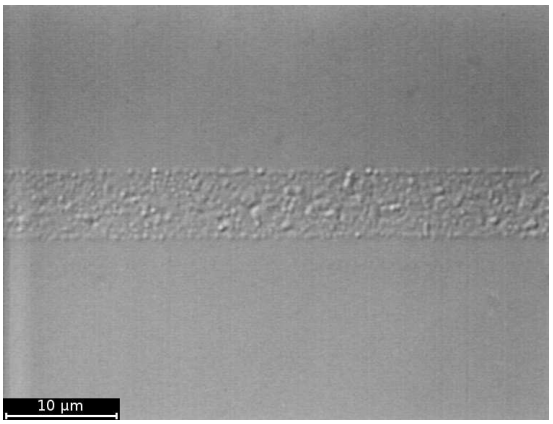

(a) Surface top view

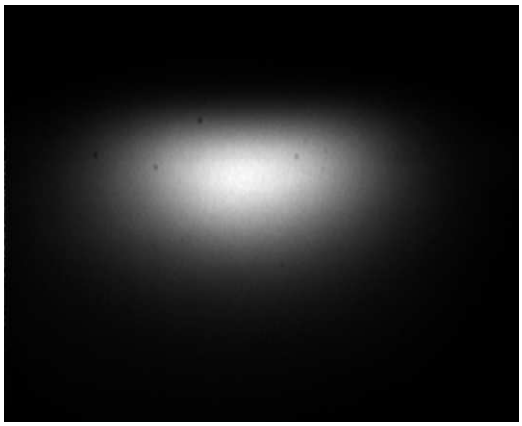

(b) Near field

Figure 8.1.: Zn-diffused waveguide sample Pb816z (Top view and near field at 1550 nm of 6-µm channels)

higher Zn layer thickness of 98 nm. The same diffusion temperature and time were used. The typical propagation loss in TM polarisation was measured to be approx. 0.15 $^{\mathrm{dB}}/_{\mathrm{cm}}$. In this sample, waveguiding in TE polarisation was observed with optical losses of $0.5 \ldots 0.6\,^{\mathrm{dB}}/_{\mathrm{cm}}$. The TM near field dimensions are nearly equal for all three waveguide widths (approx. $9.0 \times 6.0\,\mu\mathrm{m}^2$). This value is still quite large compared with TM modes in Ti-diffused waveguides.

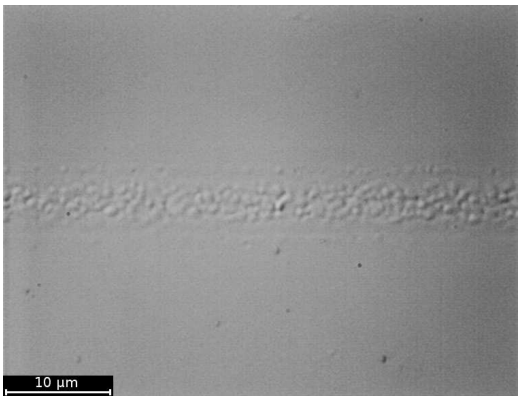

(a) Surface top view

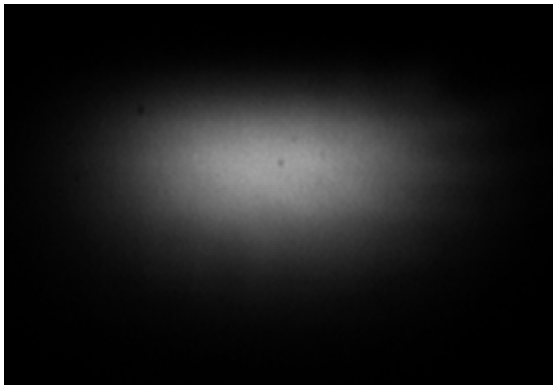

(b) Near field

Figure 8.2.: Zn-diffused waveguide sample Pb845z (Top view and near field at 1550 nm of 7-µm channels)

Using equations (4.7) and (4.9), the Zn-induced index increase at the crystal surface was calculated for sample Pb845z. It amounts to $\Delta n_{\mathrm{e}} = 0.055$ at $\lambda = 1550\,\mathrm{nm}$, which is large compared with the index increase for a standard Ti-diffused wave-

guide of $\Delta n_e = 0.014$. This is in contrast to the weak waveguiding which was observed experimentally. However, the Sellmeier equation given by Schlarb and Betzler is only accurate for short wavelengths ($\lambda \leq 1200\,\text{nm}$) and results in too large index values in the infrared region because of a missing MIR oscillator term. That Sellmeier fit can therefore not be used to set up a realistic waveguide model. Further experiments, similar to those of Ti indiffusion into MgO:SLN, are necessary to be able to model these waveguides more precisely.

8.2. Periodic Poling

The sample Pb816z was periodically poled with a grating period of 16.7 µm. The standard method for undoped CLN was used. Fig. 8.3(a) shows voltage, current, and charge during the poling process.

Also the second sample Pb845z was periodically poled (Fig. 8.3(b)). The grating period was increased to 17.96 µm in order to shift the phase matching condition to a longer wavelength and a lower temperature (see next section).

The voltage and current characteristics of these two samples show the behaviour usually observed in CLN. The voltage is ramped up until the poling current sets in. It can be noted that the initial voltage peak is very small for undoped CLN samples compared with the MgO doped samples which were presented in the previous chapters. The different charges result from different lengths of the poled areas (26 mm × 7 mm for sample Pb816z and 38 mm × 7 mm for sample Pb845z, respectively). The noise which is present in the current signal originates in electromagnetic interference due to a lacking shielding of the poling setup. The noise was more pronounced in the later experiments of this work after moving into new cleanroom facilities.

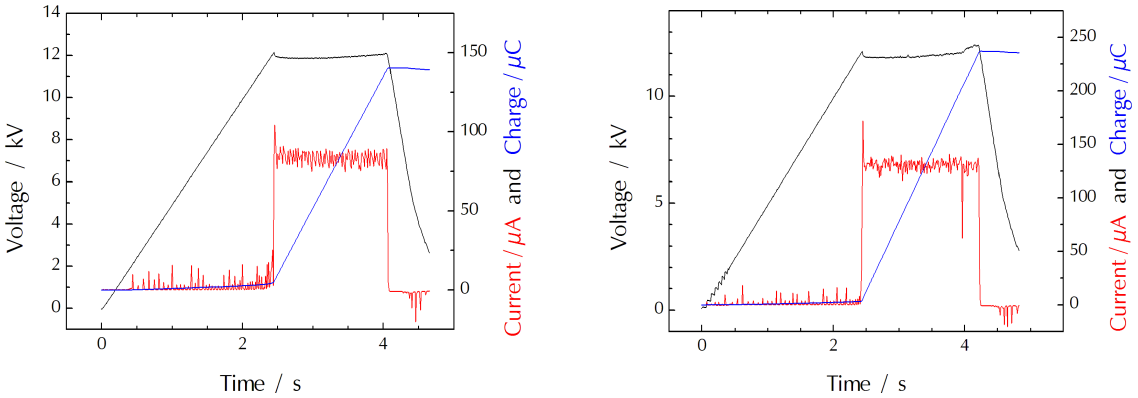

(a) Sample Pb816z (b) Sample Pb845z

Figure 8.3.: Periodic poling (current, voltage, and charge) of samples Pb816z and Pb845z

8.3. Second Harmonic Generation

SHG measurements have been carried out as usual using waveguides of the sample Pb816z. Fig. 8.4(a) shows a result in a 6 µm wide channel waveguide at a temperature of 150 °C. The high temperature had to be chosen to shift the phasematching condition to a wavelength which is within the tuning range of the ECL used as pump source (the explanation on p. 62 is also applicable here). The FWHM of the SHG peak of the sample Pb816z is 0.5 nm, which means an effective nonlinear interaction length of 23.4 mm. This is only slightly shorter than the length of the poled area of 26 mm, meaning a quite good homogeneity of the waveguide. The peak conversion efficiency is approx. 60 %/W ($\widehat{=}$ 8.9 %/W cm^2). Compared with standard Ti-indiffused waveguides (see p. 54), this is significantly smaller.

Second harmonic measurements were performed with the sample Pb845z, too. One result of a 6 µm wide channel waveguide at a temperature of 30 °C is depicted in Fig. 8.4(b). The FWHM of the SHG peak is 0.3 nm, meaning an effective interaction length of 39 mm, which nearly exactly matches the length of the poled area. This interaction length and the sinc^2-like shape of the SHG curve are signs of a very good homogeneity of the waveguide. The peak efficiency is approx. 120 %/W. While this value is larger than the efficiency measured in the previous sample, the length-normalised efficiency of 7.9 %/W cm^2 is smaller. Also this result can therefore not yet compete with Ti-diffused waveguides.

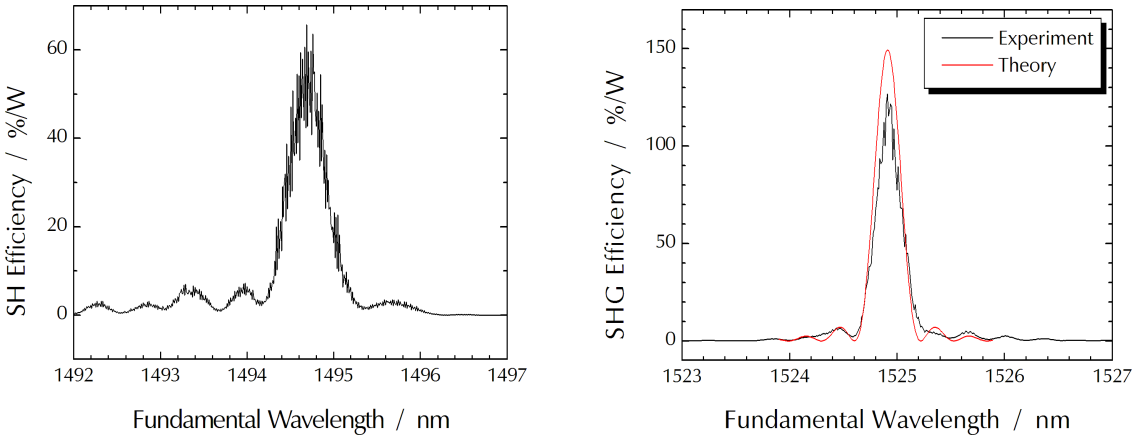

(a) Pb816z (6-µm-channel, 150 °C)

(b) Pb845z (6-µm-channel, 30 °C)

Figure 8.4.: Second Harmonic Generation in samples Pb816z and Pb845z. See text for theoretical curve.

Second harmonic generation in a Zn-indiffused waveguide was also investigated theoretically. As already described in previous chapters, the FEM tool developed by Strake can perform calculations only for Ti-diffused waveguides in

CLN. For calculating effective indices and mode sizes using this tool, proper diffusion conditions have to be set so that the theoretical index profile matches the real one as closely as possible. Since the real index profile is unknown (because the Sellmeier equation by Schlarb and Betzler is not applicable here, as mentioned above), the theoretical waveguide parameters were varied until the theoretical mode size at $\lambda = 1550\,\mathrm{nm}$ matched the measured one. This procedure resulted in a Ti layer thickness of 31 nm, a diffusion time of 12.5 h, and a waveguide width of 12 µm. Also, the dispersion of the effective indices of the propagating modes in Zn:CLN waveguides is different from the one in Ti:CLN waveguides, which leads to different phase matching wavelengths. For the calculation, the domain period was therefore adjusted to 17.699 µm so that the theoretical phase matching wavelength matched the experimentally determined one. Solving the equation system (2.18) numerically yielded the phase matching curve plotted in Fig. 8.4. The effective nonlinear coefficient was again set to $d_{\mathrm{eff}} = 20\,\mathrm{pm/V}$. Despite the imperfect waveguide model, the theoretical SHG curve fits remarkably well to the measured one.

Ming et al. [117] reported on second harmonic generation in Zn-diffused waveguides in periodically poled CLN. They achieved a SHG efficiency of $59\,\%/\mathrm{W\,cm^2}$, which is much higher than the value reported in this work. They used a Zn layer thickness of 120 nm, which leads to a better confinement of the optical modes, to smaller mode sizes, and to a higher overlap between fundamental and SH modes.

8.4. Photorefraction

The sample Pb845z was also characterised concerning photorefraction using the Fabry-Pérot method. A Ti:Sapphire laser was now available, so the measurements could be performed with a higher power than the previous measurements with the MgO-doped samples.

The experiment was carried out at different temperatures in a 7 µm wide channel waveguide. The Ti:Sa wavelength was set to 780 nm, the polarisation was adjusted to vertical using a $\lambda/2$ plate. The power behind the sample was 8 mW.

Fig. 8.5 shows the resulting time-dependent power transmitted through the sample. The number of oscillations at room temperature can be read to $m = 9.5$. At $T = 90\,^{\circ}\mathrm{C}$, the number can be estimated to $m = 1$. With a sample length of 51 mm, the refractive index changes can be calculated to $\Delta n = 1.44 \times 10^{-4}$ (30 °C) and $\Delta n = 1.5 \times 10^{-5}$ (90 °C), respectively.

The recorded curves of the transmitted power sometimes show a behaviour deviating from a oscillatory one, e. g. a sudden change in slope (see curve for $T = 30\,^{\circ}\mathrm{C}$ in Fig. 8.6 at the time $t = 150\,\mathrm{s}$). This may be attributed to coupling to different modes at the short wavelength λ_{PR}, which is a drawback of this measurement technique, as already mentioned in Section 5.3.2. Although this proba-

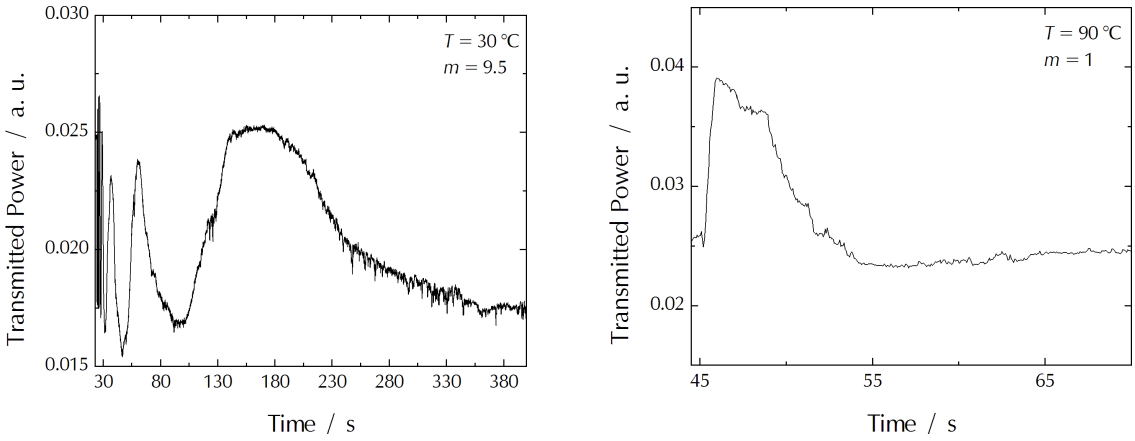

(a) $T = 30\,°C$ (b) $T = 90\,°C$

Figure 8.5.: Photorefraction measurement in sample Pb845z (7 µm wide channel)

bly has no large effect on the resulting Δn in this case, since most fringing already happens at times $t < 80\,s$, this potential source of error must be pointed out, however.

In order to compare this result with standard Ti-diffused waveguides, the measurements have been repeated in such a waveguide, too. The power of the photorefraction-inducing light should have the same intensity inside the waveguide, so that the induced index changes can be compared. Therefore, the mode sizes at a wavelength of 800 nm have been determined in the sample Pb845z and a standard Ti-diffused sample named Pb494zl.

The FWHM mode sizes were approx. $4.8\,µm \times 4.0\,µm$ (resulting in an "effective area" of $19\,µm^2$ by multiplying the FWHMs in horizontal and vertical directions) for the sample Pb845z and $2.5\,µm \times 1.7\,µm$ (effective area of $4.3\,µm^2$) for the sample Pb494zl, respectively. According to this ratio of the areas, the power (behind the sample) was chosen to be $\approx 1.7\,mW$. A potential source of error is the determination of the mode sizes at short wavelengths: because the waveguides are multi-moded at these wavelengths, it is experimentally difficult to only excite the fundamental mode. The near field pattern, which can be observed at the end of the waveguide, may be a superposition of both the fundamental and higher modes. This may result in a wrong "effective mode area" and therefore a wrong choice for the power of the photorefraction-inducing light.

The photorefraction measurement was thus carried out in the sample Pb494zl. The numbers of oscillations were $m = 9$ (30 °C), $m = 5$ (80 °C), and $m = 2$ (150 °C). Two results are displayed in Fig. 8.6. At $T = 180\,°C$, no Fabry-Pérot oscillations due to photorefraction could reproducably be observed. With a sample length of 33 mm, the according refractive index changes are $\Delta n = 2.1 \times 10^{-4}$ (30 °C), $\Delta n = 1.2 \times 10^{-4}$ (80 °C), and $\Delta n = 4.7 \times 10^{-5}$ (150 °C).

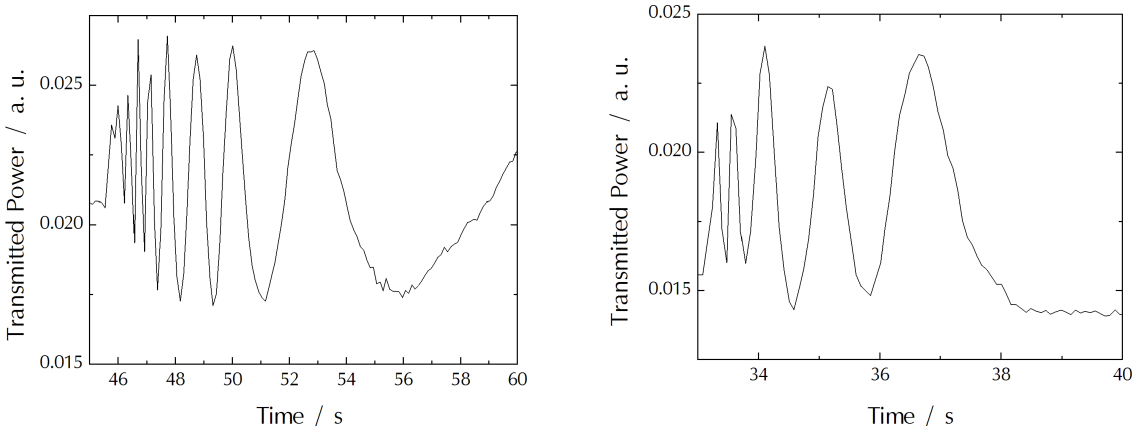

(a) $T = 30\,°C$ (b) $T = 80\,°C$

Figure 8.6.: Photorefraction measurement using Ti:CLN sample Pb494zl (6-µm-channel)

An overview of the obtained results is plotted in Fig. 8.7. As expected, the photorefraction in Ti-diffused waveguides is higher than that in Zn-diffused waveguides. In the Zn waveguides, the measured photorefractive index change at a temperature of 90 °C is comparable with the index change on the Ti waveguide at 180 °C.

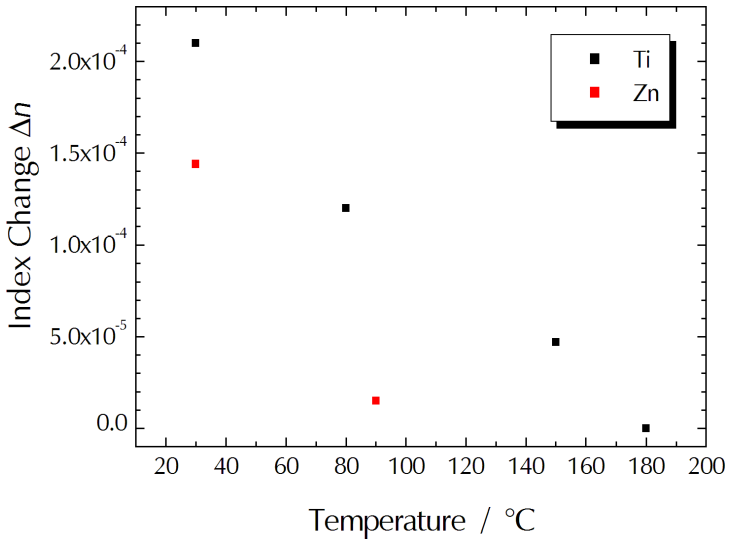

Figure 8.7.: Overview of the temperature-dependent index changes due to photorefraction in Zn-diffused and in Ti-diffused waveguides

Ming et al. [117] report that no evidence of photorefractive effect could be observed during their wavelength conversion experiments. Asobe et al. [73] report a very low photorefraction (characterised by a shift in the phasematching

wavelength) in Zn ridge waveguides fabricated by liquid phase epitaxy (LPE) and subsequent ion etching. No at least semiquantitative characterisation of Zn-indiffused waveguides in CLN concerning their photorefreactive sensitivity are known to the author, however. A direct comparison of own results to results reported in other works could therefore not be performed. Nevertheless, the observed significant reduction of the photorefraction is a positive result.

8.5. Conclusion

Concluding this chapter, Zn-diffused waveguides with low loss have successfully been fabricated. Waveguiding was observed in TM and TE polarisations. Second harmonic generation has been measured with results which can be considered satisfactory for the first experiments. The results of Ming et al. prove, however, that significantly higher SHG efficiencies are possible. Further experiments to systematically optimize the diffusion conditions, in order to achieve better mode confinement, are necessary. A better confinement of the optical modes leads to smaller mode sizes, which facilitates fibre butt coupling, and higher overlap of fundamental and SH modes. A significantly increased SHG efficiency is necessary for later wavelength conversion experiments, because the generated SH wave acts as pump for the DFG process (see Section 2.2.4)

Successful wavelength conversion experiments in Zn-indiffused waveguides have already been performed by Ming et al. This work mainly concentrates on the characterisation of the photorefraction in Zn-indiffused waveguides as well as in Ti-indiffused waveguides using the low-finesse Fabry-Pérot method. Comparing those results, the photorefraction is found to be greatly reduced in Zn waveguides, making high-power nonlinear devices possible at low temperatures.

9. Proton Exchanged Waveguides in CLN

The third waveguide type investigated in this work is the annealed proton exchanged waveguide. It is known to show a significantly reduced photorefraction compared with the bulk material. The topics of this chapter are own experiments on the fabrication of APE waveguides, the properties of those waveguides, the comparison of the photorefraction with the titanium- and zinc-indiffused waveguides fabricated previously, and finally an experiment on wavelength conversion.

9.1. Channel Waveguides

For fabricating proton exchanged waveguides, no metal stripes are necessary, but rather a slit mask on the sample surface. The traditional positive lithography process could not be used in the beginning of this investigation, because no slit photomask was available then. The slits were fabricated using the photomask #3 (see Appendix on p. 112), which was previously also used for fabricating Ti-diffused waveguides, and image reversal lithography, as explained in Section 8.1.

Using the image reversal lithography, problems concerning the homogeneity of the slit width have been observed. Therefore, a new photomask ("#2" in the Appendix) for the lithography of the metals slits for the proton exchange was designed. This mask provides slit widths of 5.5 ... 8 µm in steps of 0.5 µm. The mask was used for the last few samples.

A number of samples have been fabricated. The exchange time and temperature as well as the annealing time have slightly been varied. Among all the samples, two examples will be presented and discussed here.

One sample (named Pb784zB) was periodically poled before the proton exchange. A waveguide mask was prepared using photomask #3. The sample was then exchanged for 15 h at 160 °C and annealed for 20 h at 330 °C. The optical losses were measured to be 0.1 ... 0.4 $^{dB}/_{cm}$, the typical mode size in 7 µm wide channels was $7.7 \times 6.0\,\mu m^2$.

Another sample (named Pb812z) was proton exchanged for 15 h at 167 °C (mask #2 was used) and annealed for 20 h at 330 °C. The propagation losses were measured to be 0.15 ... 0.3 $^{dB}/_{cm}$, and the typical mode size to be $7.0 \times 5.3\,\mu m^2$. The

exchange temperature was increased for the later sample to achieve a better confinement of the mode, leading to a smaller mode size. Still, the mode size is quite large compared with the one in standard Ti-diffused waveguides.

Fig 9.1 shows images of the waveguide surfaces of the samples Pb784zB and Pb812z. It was observed that the waveguides were hardly visible under the microscope after annealing. The images have therefore been contrast-enhanced for better visibility.

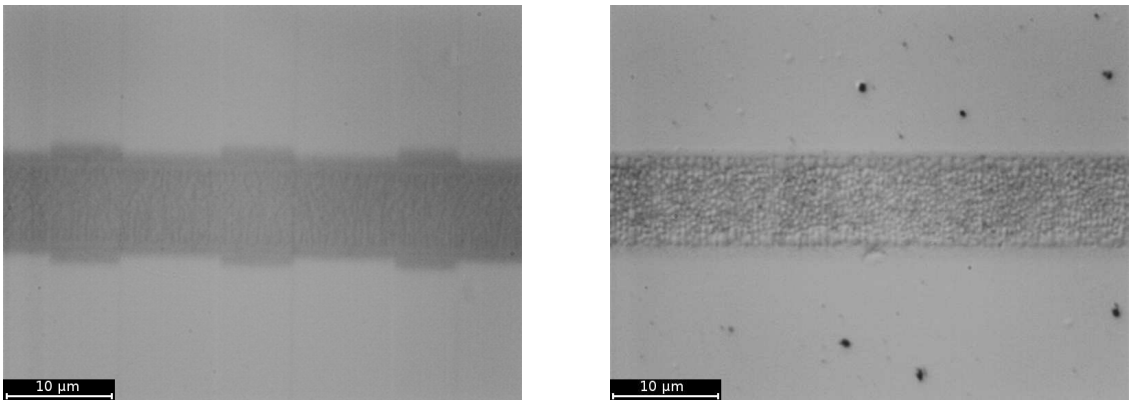

(a) Pb784zB (b) Pb812z

Figure 9.1.: APE waveguides, samples Pb784zB and Pb812z

A special feature can be observed in the samples which were periodically poled before the waveguide fabrication. The waveguides show width variations in the surface micrographs (see Fig. 9.1(a)). The reason for this is unknown. Different diffusivities for $+Z$ and $-Z$ directions would lead to different amounts of protons which are introduced into the crystal during the exchange. To the author's knowledge, different exchange rates or diffusivities for the $+Z$ and $-Z$ surfaces have not been reported up to now.

9.2. Periodic Poling

For periodic domain gratings designed for second hamonic generation in the wavelength range between 1500 nm and 1600 nm, grating periods of 14.74 µm ($\lambda_f \approx 1552$ nm [103]) or 15.5 µm ($\lambda_f \approx 1536$ nm [118]; $\lambda_f \approx 1596$ nm [119]) can be found in the literature. These periods are smaller than those usually used for standard Ti-diffused waveguides for applications in the mentioned wavelength range ($\Lambda \approx 16.6$ µm).

The first poled APE-treated samples were therefore poled with the shortest periods available ($\Lambda = 16.1$ µm and $\Lambda = 16.2$ µm). Only the last sample Pb812z

was poled with a larger period of 17.96 µm because the SHG phase matching condition turned out to be at too low a wavelength at room temperature.

Periodic poling was done prior to the proton exchange in nearly all samples, but also poling after the waveguide fabrication was tried (sample Pb812z).

The standard poling technique was utilised for this type of samples. Plots of voltage, current, and charge can be found in Fig. 9.3. As for the Zn-indiffused waveguide samples, the voltage and current characteristics of these two samples show no special features and need no detailed discussion. The length of the poled area was 26 mm in both samples, the sample area of 202 mm^2 leads to a set-point value of 162 µC for the charge, which is nearly exactly the actual value for the charges for both samples.

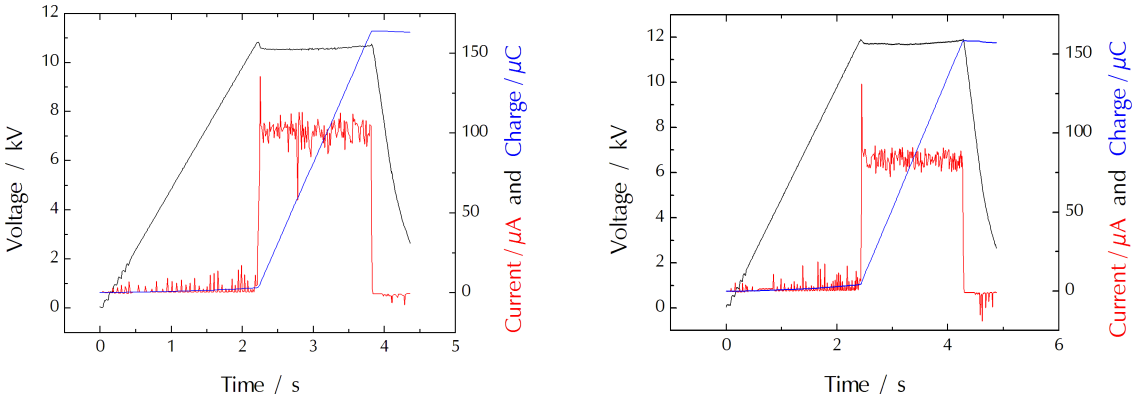

(a) Pb784zB (b) Pb812z

Figure 9.2.: Periodic poling (voltage, current, and charge characteristic) of samples Pb784zB and Pb812z

9.3. Second Harmonic Generation

The domain period of Pb784zB was 16.20 µm. Second harmonic generation was investigated in 7 µm wide waveguides. At a temperature of 110 °C, SHG could be observed at ≈ 1477 nm. Again, as explained in Sect. 6.2.3, the temperature had to be increased to shift the phasematching condition to a wavelength which was accessible with the tunable ECL. The peak conversion efficiency is approx. 65 %/W (if the oscillations at the maximum, which arise from the air gap between the fibre and the sample endfaces, acting as a Fabry-Pérot etalon, are not taken into account). With a sample length of 25.5 mm, the length-normalised conversion efficiency can be calculated to be 10 %/W cm^2.

The FWHM of the SHG curve of the sample Pb784zB is 0.4 nm. This is the result of an effective interaction length of 29 mm, which is even longer than the

sample length. The reason may be slightly different dispersion properties of the APE waveguide than those assumed in Eq. (2.25). From the small FWHM and the sinc^2-like shape, a good homogeneity of the waveguide can be concluded.

The choice of a small domain periodicity, which was inspired by values found in the literature, did not lead to a phase matching condition at a usable wavelength. The reason is probably a weaker mode confinement in the waveguides of this work. For a given temperature, the phase matching wavelength shifts to smaller values if the index profile is shallower.

The sample Pb812zB was poled with a larger period of 17.96 µm in order to shift the phase matching temperature to a longer wavelength. Fig. 9.3(b) shows a SHG result in channel 10b, which is a 6 µm wide waveguide. It is notable that not only the fundamental SH mode TM_{00}, but also the first higher mode in depth direction TM_{01} can be excited. The conversion efficiencies are approx. 25 %/W (TM_{00}) and 40 %/W (TM_{01}), respectively. Again, the peak efficiencies appear to be higher because of the afore mentioned Fabry-Pérot effect. An efficiency of 25 %/W equals a length-normalised efficiency of only 3.7 %/W cm^2.

The FWHM of the SHG curve (for the fundamental SH mode) of the sample Pb812z is 0.69 nm, resulting from an effective interaction length of 17 mm. This is shorter than the actual length of the poled area. Also, the shape of the SHG curve deviates from the sinc^2-like behaviour. The homogeneity of this waveguide can therefore considered to be worse.

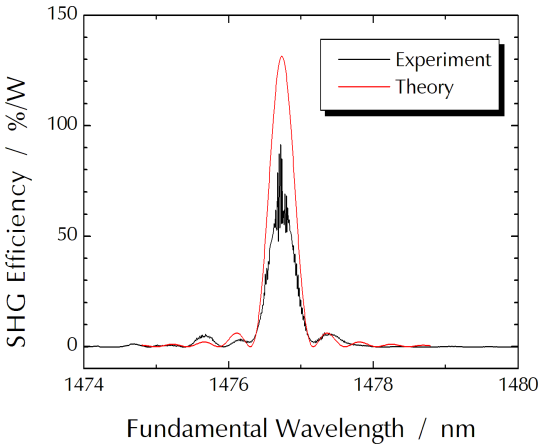

(a) Pb784zB (Λ = 16.20 µm, 110 °C, 7 µm channel width)

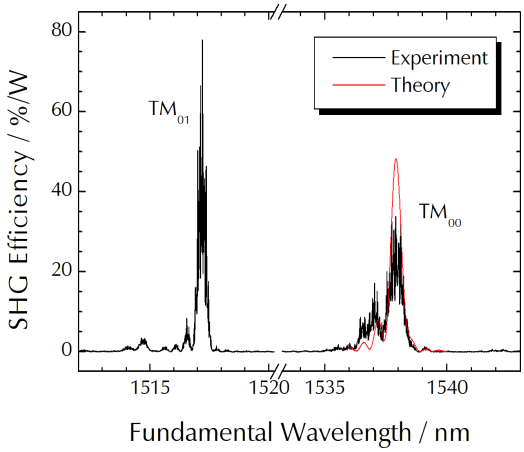

(b) Pb812z (Λ = 17.96 µm, 40 °C, 6 µm channel width)

Figure 9.3.: Second harmonic generation in APE waveguide samples Pb784zB and Pb812z. See text for theoretical curves.

An explanation for the higher conversion efficiency for the higher TM_{01} mode is the presence of a surface-near "dead layer", see Section 4.2.3. This can lead to a higher overlap of the fields of the fundamental mode at the fundamental

wavelength and the higher mode at the SH wavelength (see also Fig. 2.3 for field distributions).

It can also be noted that the FWHM of the curve for the coupling to the TM_{01} SH mode is smaller than the width of the peak for the fundamental mode coupling. The reason is a different dispersion of the effective indices of the two SH modes which enters Eq. (2.24).

Theoretical SHG curves have been calculated as well. No particular waveguide model has been used here. The mode sizes were measured at $\lambda = 1550\,\text{nm}$ and $\lambda = 800\,\text{nm}$ for the sample Pb784zB and at $\lambda = 1550\,\text{nm}$ for the sample Pb812z. The mode size at $\lambda = 800\,\text{nm}$ has not been measured for the sample Pb812z, so it has been assumed to be half of the mode size at $\lambda = 1550\,\text{nm}$, since this behaviour was observed in 6 µm wide waveguides of the sample Pb784zB. Using GHG approximations of the field distributions, the overlap factor was calculated. The equation system (2.18) was solved numerically. For the sample Pb812z, a quadratic inhomogeneity of the waveguide was assumed so that the calculated curve matches well the experimental one. The resulting curves are also plotted in Fig. 9.3. The theoretical peak efficiencies are slightly larger than the experimentally observed efficiencies. Possible reasons for that are a mismatch between the assumed overlap factors and the actual ones, and an influence of the "dead layer" mentioned above, which reduces the effective nonlinearity.

Chou et al. [120] reported a SHG efficiency of $65\,\%/\text{W}\,\text{cm}^2$ already in 1999. Their fabrication parameters (PE depth of 0.7 µm, annealing for 26 h at 325 °C) were quite similar to those of the waveguides of this work. They investigated a 12 µm wide waveguide, however. Nevertheless, the nonlinear optical performance of the waveguides of this work is not state-of-the-art. Further work, like fine-tuning the exchange conditions to increase the overlap factor, or to refine the photolithography procedure to achieve a better waveguide homogeneity, is necessary to improve the quality of these waveguides.

9.4. Photorefraction

The sample Pb784zB was characterised concerning photorefraction in the same way as the samples Pb845z (Zn-indiffused) and Pb494zl (Ti-indiffused), using the Fabry-Pérot method, so the results are easily comparable.

The mode sizes in different waveguides at a wavelength of 800 nm were measured. The "effective areas" varied between 15 μm^2 and 21 μm^2. The waveguide V1, which was used for this investigation, showed an effective mode area of 16 μm^2. The laser power was therefore chosen such that the power behind the sample was approx. 4 mW ($\approx \frac{16\,\mu\text{m}^2}{19\,\mu\text{m}^2} \times 5\,\text{mW}$) to get a nearly identical intensity as in the Zn-doped sample Pb845z.

Fig. 9.4(a) shows the result of the photorefraction measurement at 30 °C. The

number of oscillations can be estimated to $m = 0.5$. This means an index change of $\Delta n = 1.5 \times 10^{-5}$. At a temperature of 80 °C, no oscillations were observed at this laser power level.

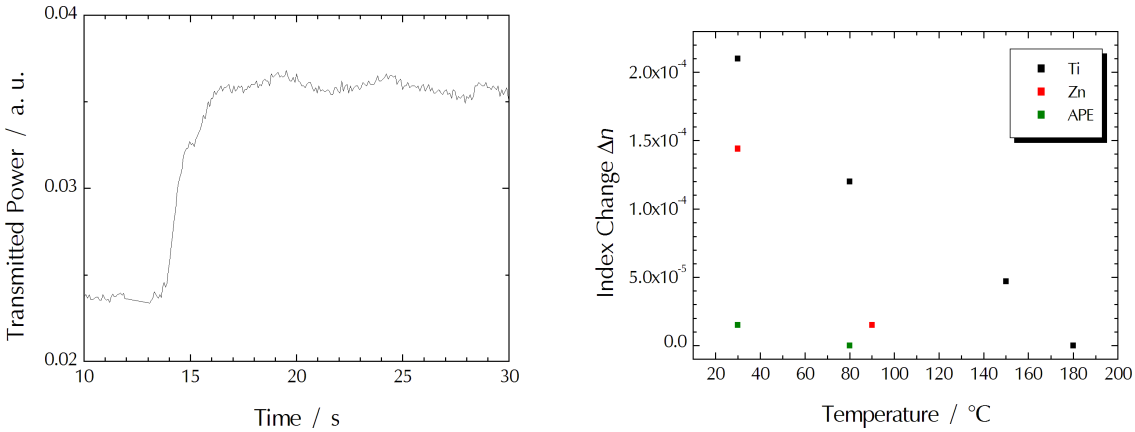

(a) P/R in Pb784zB ($T = 30$ °C)

(b) Comparison of different samples

Figure 9.4.: (a) Photorefraction measurement in sample Pb784zB (7 µm wide waveguide, $T = 30$ °C.) (b) Overview of the temperature-dependent index changes due to photorefraction in Zn-diffused, Ti-diffused, and APE waveguides

Fig. 9.4(b) gives an overview of the index changes measured in the three samples Pb784z (APE), Pb845z (Zn) and Pb494zl (Ti). The photorefraction in the APE waveguides is significantly reduced compared with the Zn-diffused waveguides.

As already mentioned in Section 8.4, these results may be incorrect due to an incorrect determination of the effective mode area, resulting in a wrong power of the photorefraction-inducing light.

Fujiwara et al. [10] also compared the photorefraction of APE waveguides and Ti-diffused waveguides. They measured the photorefraction-induced Δn using a Mach-Zehnder interferometer. Over an intensity range of approx. 2...20 $\mathrm{W/cm^2}$, they observe in an APE waveguide at $\lambda = 488$ nm a Δn which is two orders of magnitude smaller than a Δn in a Ti-diffused waveguide at $\lambda = 633$ nm. They do not mention any temperature, so probably their experiments took place at room temperature. The result of this work is only a factor of 10 between the induced index changes in APE and Ti waveguides (see Fig. 9.4(b)). However, the intensity used in this work is approx. 10^4 times larger than the intensity used by Fujiwara et al., and also other wavelengths were used, so the results are not necessarily comparable.

9.5. Resonant SHG and Wavelength Conversion

Nonlinear devices leveraging resonant enhancement of the fundamental wave or the second harmonic wave promise to increase the conversion efficiency significantly [121]. To test the stability of resonant SHG in APE waveguides at high optical powers, such a wavelength conversion experiment was also carried out.

Different versions of resonators are possible. The fundamental wave or the second harmonic wave may be the resonant one, or even both ones (doubly-resonant SHG). For this experiment, the SH wave was chosen to be the resonant wave. Mirrors consisting of a stack of 10 dielectric layers (alternatingly TiO_2 and SiO_2) were deposited on the sample endfaces. The transmittance T of these mirrors on glass were measured using a spectrophotometer. The resulting reflectance R (assuming $R = 1 - T$ for lossless mirrors) is plotted in Fig. 9.5(a). The reflectance has a maximum around 800 nm ($R = 95.6\,\%$ and $R = 95.0\,\%$, respectively, for right and left sides) and a minimum around 1600 nm ($R = 14\,\%$ and $R = 16\,\%$, respectively).

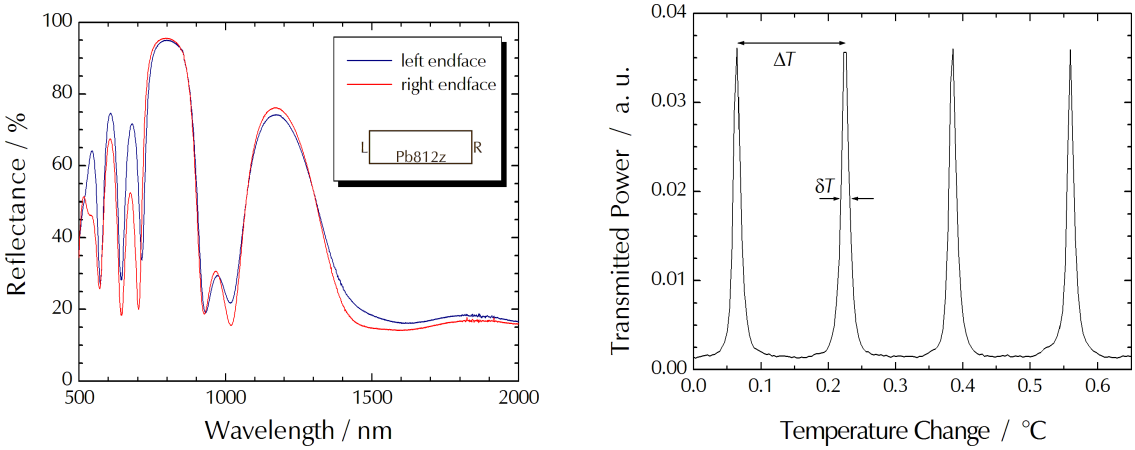

(a) Endface mirrors

(b) Finesse measurement (4-µm-channel)

Figure 9.5.: Resonator properties of sample Pb812z. (a) Reflectance of endface mirrors (HR @ 775 nm and AR @ 1550 nm) (b) Measurement of finesse $\mathcal{F} = \Delta T/\delta T$ at 765 nm (Ti:Sa laser), $T \approx 90\,°C$

To determine the finesse of the waveguide resonator, the transmitted power though the sample at a wavelength of 765 nm was monitored while changing the optical path length by changing the temperature. The measurement took place at approx. 90 °C to reduce the photorefraction. A 4 µm wide waveguide was chosen to ensure that only the fundamental TM_{00} mode would be excited. The sample length was 29 mm. Fig. 9.5(b) shows the best result obtained. The value calculated from the curve is $\mathcal{F} = \Delta T/\delta T = 12.9$. Measurements in other channels of the sample resulted in smaller values of approx. 8. Assuming mirror reflectivities of

94 %, a finesse of 12.9 results from propagation losses of $\alpha = 0.28\,\mathrm{dB/cm}$. While this result has not been verified using an independent measurement method like the low-finesse method, it does not seem unrealistic.

First, second harmonic generation has been investigated in the resonator sample. Fig. 9.6 shows the SHG curve which was recorded with the finest resolution possible (1 pm). The resonant behaviour is clearly visible.

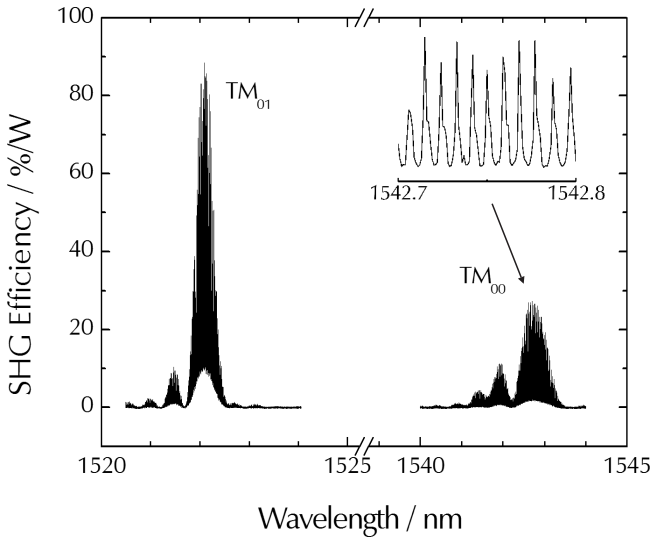

Figure 9.6.: Efficiency for resonant SHG in sample Pb812z (6 µm wide channel, 80 °C), recorded with 1 pm resolution

The measured peak SHG efficiency, however, is not increased compared with the non-resonant curve shown in Fig. 9.3(b). The generated SH power—and therefore the efficiency η—increases with the power enhancement factor f. This factor is as follows [122]

$$f = \frac{1 - R_\mathrm{f}}{\left(1 - \sqrt{R_\mathrm{f} R_\mathrm{r}}\,\mathrm{e}^{-\alpha L}\right)^2} \tag{9.1}$$

where R_f and R_r are the front and rear mirror reflectivities, α is the propagation loss, and L is the sample length. Assuming the values mentioned above, an enhancement factor of $f = 1.3$ can be expected. The measured loss at $\lambda = 1550\,\mathrm{nm}$ is $0.29\,\mathrm{dB/cm}$, the loss at shorter wavelengths is probably higher. Assuming a propagation loss of $0.34\,\mathrm{dB/cm}$ results in $f = 1.0$ (i. e. no enhancement).

From this result, an increased SHG efficiency can not be expected from these waveguides. The quality of the waveguide resonators has to be increased significantly by improving the mirror reflectivities and by reducing the waveguide losses in order to achieve high power enhancement factors.

Next, wavelength experiments concerning all-optical wavelength conversion

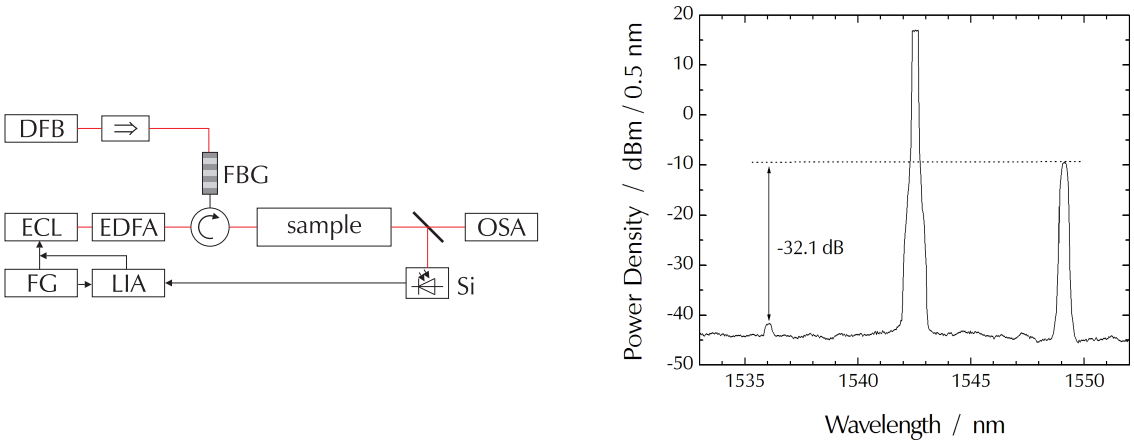

(a) Experimental setup (b) AOWC spectrum

Figure 9.7.: Resonant cSHG/DFG wavelength conversion. (a) Experimental setup. See text for explanation and abbreviations. (b) Wavelength conversion spectrum and conversion efficiency, channel 10b, $P_p = 200\,\mathrm{mW}$.

were performed. The setup used for the experiments is sketched in Fig. 9.7(a). As fundamental (pump) source, an ECL, whose radiation was boosted by a fibre amplifier (EDFA), was used. As signal source, a distributed feedback (DFB) laser was used. The pump and signal wavelengths were chosen to be approx. 1542.6 nm and 1549 nm, respectively. A circulator was used to send the pump light, connected to the first port, to a fibre bragg grating (FBG) at the second port, which was tuned to the pump wavelength. This setup has the advantage that only little power is lost and the remaining amplified spontaneous emission (ASE) of the EDFA is not reflected back to the sample because of the small bandwidth of the FBG. The signal light from the DFB laser is transmitted by the FGB, since it is not tuned to that wavelength. An optical isolator is used to block the DFB laser from the transmitted ASE light. Behind the sample, the light was split using a bulk beam splitter which has a splitting ratio of 50%:50% for the visible range and 87.4%$\parallel$:12.6%$\perp$ measured at 1542 nm. The output light could be monitored using a silicon photodiode as well as an optical spectrum analyser (OSA). Using the power measured by the OSA and the one measured in front of the sample using a fibre power meter, the fibre-to-fibre insertion loss was measured to be approx. 5 dB. The ECL was frequency modulated using a function generator (FG). The SHG signal from the photodiode was fed back to the ECL using a lock-in amplifier (LIA). Using this feedback scheme, the ECL was stabilised to a cavity resonance of the sample.

In the wavelength conversion experiments, the pump source was amplified up to 200 mW. The power of the DFB laser was slightly tuned to optimise the resulting idler power. The resulting spectrum at 200 mW pump power, as an example,

is shown in Fig. 9.7(b). The resolution of the OSA was set to 0.5 nm, so the ordinate of the plot is scaled in $^{\mathrm{dBm}}/_{0.5\,\mathrm{nm}}$. Since the linewidth of the lasers is much smaller than this value, the laser lines appear in the spectrum as broad lines with a flat top at their actual power levels in dBm.

For pump powers of 100 mW and 200 mW, conversion efficiencies of −33.6 dB and −32.1 dB, respectively, could be achieved. This is significantly smaller than the efficiencies reported in the literature for single-pass AOWCs using Ti-diffused or APE waveguides. Schreiber et al. [123] achieved a conversion efficiency of −10 dB (Ti:CLN), Chou et al. [120] report an internal conversion efficiency of −8 dB (APE:CLN). They used similar pump power levels (Schreiber 214 mW, Chou approx. 300 mW).

The reason for the low wavelength conversion efficiency is the very low SH power, which acts as pump for the difference frequency process (see Fig. 2.11). With an SHG efficiency of 20 %/W, and a coupled fundamental power of 100 mW (estimated from the measured power of 17 dBm in Fig. 9.7(b) and the afore mentioned insertion loss), the generated SH power is only 2 mW. A much higher power would be necessary for driving an efficient DFG process, requiring an improved waveguide sample having a higher SHG efficiency.

9.6. Conclusion

Low-loss waveguides in congruent lithium niobate could successfully be fabricated by proton exchange and a subsequent annealing step (APE), although the reproducibility can still be enhanced.

The achieved SHG conversion efficiencies were quite low. By refining the proton exchange conditions and the annealing conditions, waveguides with a smaller mode size and a higher overlap between fundamental and second harmonic modes should be obtained. Since the waveguide homogeneity for the sample Pb812z, which was prepared using a dedicated slit photomask, seems worse than that of sample Pb784zB, the fabrication of the slit mask on the sample surface needs also to be improved. A better waveguide homogeneity leads to a narrower SHG curve with a higher peak efficiency. Also, since the sample Pb784zB, being periodically poled before the waveguide fabrication, shows a higher SHG efficiency than the sample Pb812z, further samples should be poled in this way.

Further work must be done in setting up a complete waveguide model, so that the refractive index profile resulting from the exchange step and the annealing (i. e. diffusion) step are known as exactly as possible. For the dependence of the refractive index on the local proton concentration and its dispersion, the result of Roussev [89] (Eq. (4.12)) can be used. These dependences could also be determined in own experiments, as it was done for indiffused titanium in MgO:SLN. Using such a waveguide model, phase matching conditions for nonlinear interactions can be predicted more precisely. The right domain period for given wave-

guide parameters and target wavelengths could then be calculated in advance, instead of a "trial-and-error" approach used in this work.

AOWC experiments were conducted successfully. The conversion efficiencies were quite small, but wavelength conversion at low temperatures and moderately high pump powers have proven to be possible. For the resonant wavelength conversion scheme, the quality of the waveguide resonators has to be improved by enhancing the reflectivity of the endface mirrors and by refining the exchange and annealing conditions to obtain waveguides with lower propagation losses ($< 0.1\,^{\mathrm{dB}}/_{\mathrm{cm}}$ is desirable for a high power enhancement factor).

Only a very small sensitivity to photorefraction could be measured. The photorefraction-induced index change is approx. one order of magnitude smaller than that of a Ti-diffused waveguide. According to the comparison above, the APE waveguides are the best choice for high-power optical applications among the waveguide types presented so far.

10. Proton Exchanged Waveguides in MgO:CLN

The last experiments of this work were the fabrication of annealed proton exchanged waveguides in MgO(5%):$LiNbO_3$ and the comparison of their properties with those of the waveguides previously made. The advantages of both the proton exchanged waveguides and the MgO-doped bulk material are expected to be combined in such waveguides.

10.1. Periodic Poling

A MgO-doped (5 mol%) CLN sample Pb5zMg5 was periodically poled prior to the waveguide fabrication with a periodicity of $\lambda = 17.96\,\mu m$. The method of UV-assisted poling, which was already described previously in Sections 4.3.2 and 6.2, was also tried here. See Fig. 10.1 for plots of voltage, current, and charge.

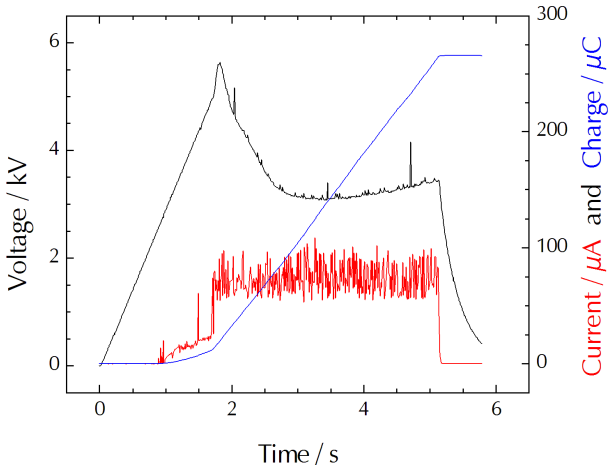

Figure 10.1.: Periodic poling (voltage, current, and charge) of sample Pb5zMg5

No reduction of the coercive voltage could be observed, though. Also, the initial voltage peak is higher than observed in previous experiments (see Section 6.2.2). The reason for this is unclear. The sample Pb5zMg5 has been cut from a wafer belonging to an older batch than those samples reported on in Section 6.2. If there are variations of the MgO content between different wafer batches, and

if the MgO content of the sample Pb5zMg5 is lower, this would lead to a higher coercive voltage and to a smaller or even no reduction of the coercive voltage by UV light. Wengler [99] points out that UV light of $\lambda = 334\,\text{nm}$ leads to a significant reduction of the coercive voltage only if the magnesium concentration of the crystal is above the optical damage threshold. Maybe, due to an error in the experimental setup, the UV radiation did simply not reach the sample surface, or reached only a fraction of the surface. The current flow which is visible in Fig. 10.1 before the "main" poling current sets in may be explained by this (domain inversion starts for a part of the sample at lower voltages, the major poling process starts at a larger voltage). This would, however, not explain the large initial voltage peak.

It is unclear how the unsuccessful UV assistance during the periodic poling affects the quality of the domain grating. However, the periodic domain structure became visible due to some slight etching during the cleaning process (see Fig. 10.2). The domain grating turned out to look quite regular and homogeneous, so this issue is probably of minor importance for the first nonlinear optical investigations using this sample.

10.2. Channel Waveguides

Titanium masks of type #2 (see p. 111) were prepared as usual on the surfaces of the samples. The proton exchange was carried out at a temperature of 171 °C for 17.5 hours. The subsequent annealing took place at 330 °C for 20 h. For this first test of APE in MgO:CLN, the fabrication conditions were chosen similar to those used for APE in undoped CLN to allow direct comparison with the previous samples. It is known, however, that the exchange in MgO-doped material is slower [30], so that the fabrication conditions will have to be refined in future experiments.

After the polishing, the sample length was 26 mm. Fig. 10.2 shows the waveguide surface of the sample Pb5zMg5 after the APE process. The waveguide morphology looks quite rough. However, despite the apparent bad quality, optical losses down to $0.2\,^{\text{dB}}/_{\text{cm}}$ could be measured. The photomicrograph does not give a clear indication about width variations of the waveguide like those observed in APE:CLN waveguides (see p. 88). A strongly contrast-enhanced version is shown in Fig. 10.2(b). In that picture, some slight variations are visible. However, this issue has to be clarified in later experiments when fabricating waveguides with higher proton concentrations.

Fig. 10.3 shows near field images of two waveguide channels at two different wavelengths (800 nm and 1550 nm). The mode size measured for channel 14a at 1550 nm was $7.7 \times 6.3\,\mu\text{m}^2$, which is slightly larger than those of the APE:CLN waveguides. This was expected, however, due to the weaker waveguiding.

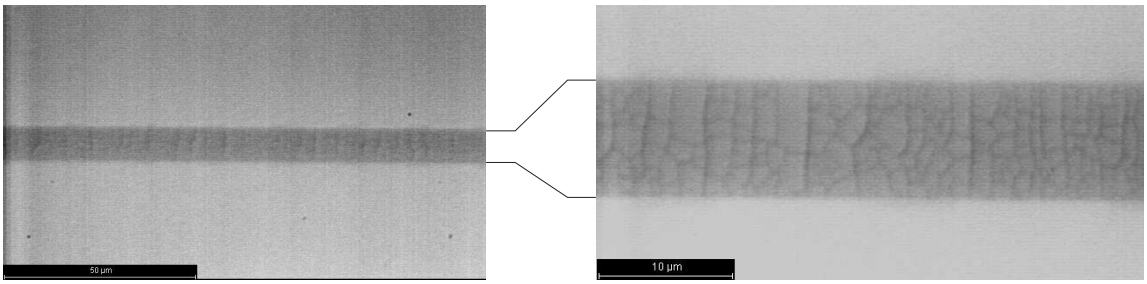

(a) Surface of APE waveguides

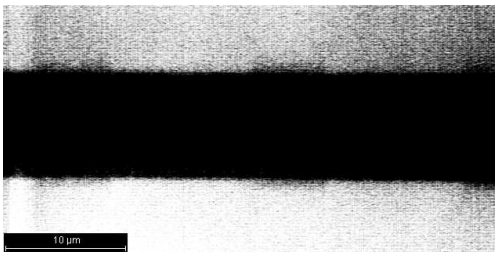

(b) Strongly contrast-enhanced picture

Figure 10.2.: Surface of annealed proton exchanged waveguides in MgO:CLN (sample Pb5zMg5)

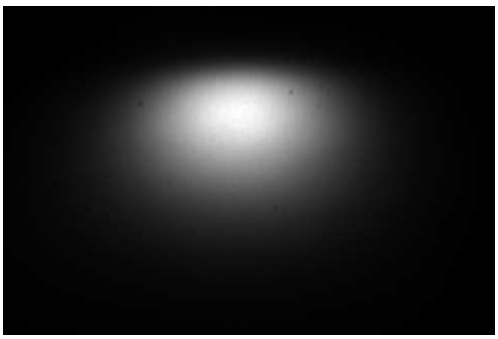

(a) $\lambda = 1550\,\text{nm}$ (channel 14a)

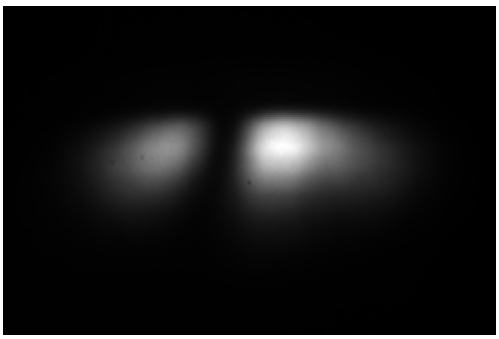

(b) $\lambda = 800\,\text{nm}$ (channel 16a)

Figure 10.3.: Near field images at different wavelengths (sample Pb5zMg5)

10.3. Second Harmonic Generation

Second harmonic generation has been investigated in sample Pb5zMg5, too. The results, measured at 30 °C and 80 °C in channel 14a, are shown in Fig. 10.4. The coupled input power at 1550 nm was 1 mW. Again, coupling to the fundamental TM_{00} SH mode and the higher TM_{01} mode is observed. Also, the two SHG peaks show different FWHMs due to different dispersion properties of the effective indices of the two modes.

The peak conversion efficiency is 15 %/W ($\widehat{=}$ 2.2 %/W cm^2). This number is very low compared with our "standard" nonlinear devices and even smaller than the result of sample Pb812z (see p. 90). This can be attributed to the weak waveguiding and the small overlap between the fundamental and the second harmonic modes. With improved fabrication conditions, the efficiency can be expected to increase. Another possible reason for a smaller SHG efficiency is a reduced effective nonlinearity due to an imperfect periodic poling. Since the poor nonlinear performance of these waveguides can fully be explained, theoretical calculations of the SHG efficiency have not been performed.

Asobe et al. [124] report on second harmonic generation in MgO-doped APE waveguides. They observed an efficiency of 25 %/W in a 10 mm long waveguide. They chose exchange and annealing conditions to obtain a FWHM mode size of $5.0 \times 2.5\,\mu m^2$ at $\lambda = 1550$ nm. This is much smaller than the mode size reported here and proves that the overlap factor and therefore the SHG efficiency can be significantly increased by carefully tailoring the waveguide fabrication parameters.

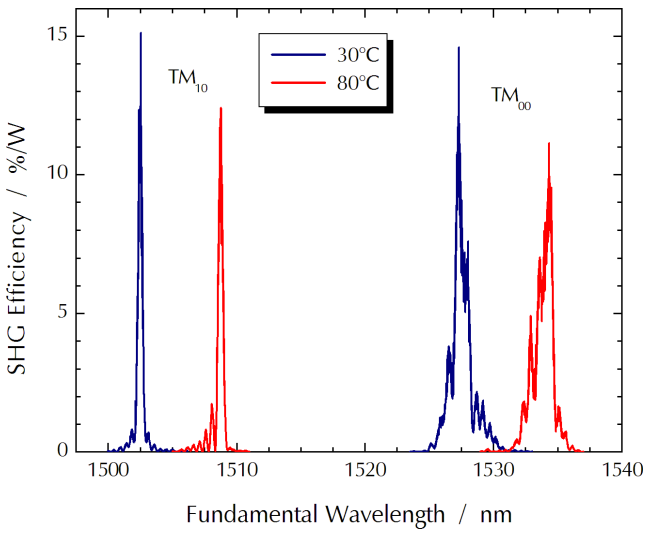

Figure 10.4.: Second Harmonic Generation at 30 °C and 80 °C

10.4. Photorefraction

Photorefraction measurements were also performed for this sample using the same setup explained in previous chapters. The measurements at two different temperatures (30 °C and 50 °C) are shown in Fig. 10.5(a).

Since it was not possible by the experimentator to excite the fundamental mode at a wavelength of 800 nm and to measure its mode size (only the TM_{01} mode or a superposition of modes could be observed), the effective area of the TM_{10} mode has been used for setting the appropriate power of the photorefraction-inducing light (Fig. 10.3(b)). It was estimated to 21 µm^2, which is slightly larger than the mode size measured for the Zn waveguide sample Pb845z. The power of the Ti:Sa laser was adjusted to obtain a power of 6 mW behind the sample.

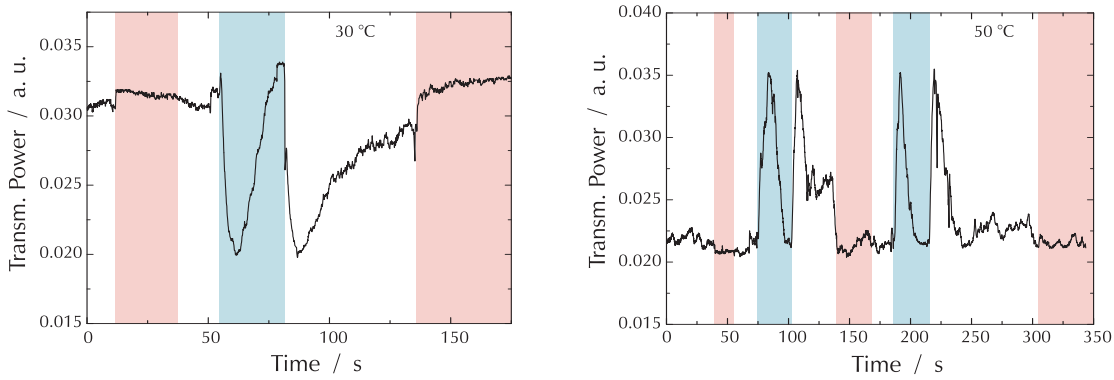

(a) P/R in Pb5zMg5

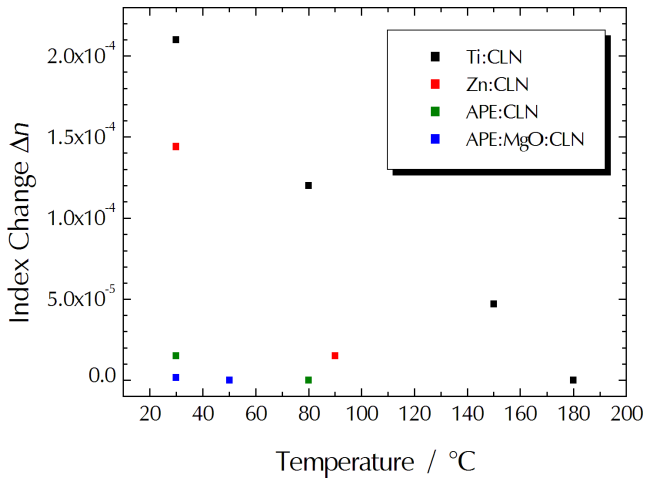

(b) Comparison of different samples

Figure 10.5.: (a) Photorefraction measurements at 30 °C and 50 °C (red: Ti:Sa on; blue: UV-B on) (b) Comparison of the photorefractive sensitivity of different samples, now including sample Pb5zMg5

At 30 °C, a slight variation of the transmitted probe beam light can be observed when the Ti:Sa beam is switched on. Fig. 10.5(a) shows the transmitted power versus time. The time ranges where the photorefraction-inducing from the Ti:Sa was switched on are marked red in the plots. The time ranges where illumination with UV-B light took place in order to erase the induced index change in the waveguide are marked blue in the plots. One full oscillation can be observed during the time of UV-B illumination. From this, the number of fringes which occur when the Ti:Sa light is switched on ($t = 12\,\mathrm{s}$ and $t = 136\,\mathrm{s}$) has been estimated to approx. $m = 0.1$, corresponding to an induced index change of $\Delta n = 3 \times 10^{-6}$.

It must again be noted that the determination of the mode size at short wavelengths is error-prone, since it is experimentally difficult to only excite the fundamental mode. A wrong power of the photorefraction-inducing light is chosen if the mode size is determined incorrectly.

At the slightly higher temperature of 50 °C, no change in transmitted power can be observed. At least at this power level, the waveguide shows no photorefraction in this experiment.

Fig. 10.5(b) shows the updated comparison of the photorefractive sensitivity, now including the result in the APE:MgO:CLN waveguide.

Asobe et al. [124] investigated the photorefractive effect in APE waveguides fabricated in undoped CLN as well as MgO-doped CLN. They characterised the photorefraction by observing a shift of the SHG phasematching wavelength while photorefraction-inducing light with $\lambda = 784\,\mathrm{nm}$ and a power of 20 mW was launched into the waveguide. At 25 °C, they observed a shift of 3.0 nm in an APE:CLN waveguide, and only 0.4 nm in an APE:MgO:CLN waveguide. At 50 °C, they could not observe any wavelength shift in the MgO-doped waveguide, which is consistent to the result of this work.

10.5. Conclusion

Many remarks and conclusions stated for APE:CLN waveguides in the previous chapter are also valid for APE waveguides in MgO-doped CLN.

Low-loss waveguides could successfully be fabricated. The waveguiding was too weak, leading to large mode sizes. The waveguide fabrication parameters will have to be refined in future experiments to obtain mode sizes which are similar to those in "standard" Ti-diffused waveguides. The overlap between fundamental and second harmonic modes can then also be expected to increase, leading to higher SHG efficiencies.

From Fig. 10.5(b), it can be concluded that the APE:MgO:CLN waveguides show the smallest photorefractive sensitivity and are therefore well-suited for wavelength conversion devices at high optical powers near room temperature, if the remaining issues (waveguide fabrication and periodic poling) can be solved.

11. Summary and Outlook

Summary

In this work, a number of different types of waveguides, which promised to reduce the photorefractive sensitivity, have been fabricated. Low photorefraction is key for the target application of wavelength conversion utilising nonlinear integrated optics.

The waveguides were investigated concerning their surface morphology and optical losses. Periodic ferroelectric domain gratings have been fabricated using either standard electric field poling or a newly-developed method using UV light for a reduction of the coercive voltage. Second harmonic measurements have been carried out in order to assess the nonlinear properties of the waveguides, including the quality of the domain grating. An experiment concerning all-optical wavelength conversion has been performed using one of the waveguide types.

A recap of the chapters of this work follows:

- Ti-diffused waveguides in MgO-doped CLN.

  Two approaches of fabrication were investigated for this waveguide type. The diffusion of MgO into already periodically poled Ti:CLN waveguide samples was tried as well as the indiffusion of Ti stripes into commercially available bulk-doped MgO:CLN with a subsequent poling. The waveguides doped by diffusion showed a rough morphology, high losses and low SHG efficiency. SNMS investigations of planar indiffused samples revealed a Mg-rich surface-near layer, leading to a poor surface quality and a degraded nonlinearity. High-quality titanium-diffused waveguides can be fabricated directly in bulk MgO-doped $LiNbO_3$. Using the new method of UV light assistance, also the MgO-doped crystals could be successfully periodically poled with a good homogeneity. However, no reduction of the photorefractive sensitivity in Ti:MgO:CLN waveguides—in contrast to bulk crystals—could be observed.

- Ti-diffused waveguides in MgO-doped SLN.

  First, the diffusion of titanium into MgO:SLN was investigated using optical and SNMS measurements at planar waveguides. Channel waveguides could be successfully be fabricated. The morphology was not satisfactory and the optical losses were still quite high, however. Periodical poling was

also performed with UV light assistance. The resulting quality of the domain grating as well as the SHG efficiency was not satisfactory. A reduction of the photorefraction—again, in contrast to bulk MgO:SLN crystals—was not observed.

- Zn-diffused waveguides in CLN.

  Channel waveguides using zinc indiffusion could be fabricated with low optical losses. Using the standard E-field poling, domain gratings were fabricated, resulting in acceptable, yet improvable, second harmonic results. The photorefractive sensitivity was measured to be reduced compared with Ti:CLN waveguides.

- APE waveguides in CLN.

  Using the annealed proton exchange method, channel waveguides were fabricated in undoped CLN. Some waveguides had very low optical losses of $\leq 0.1\,{}^{\mathrm{dB}}/_{\mathrm{cm}}$. Periodal poling could be performed successfully. SHG efficiencies were not very high, but acceptable in some samples. Wavelength conversion in the C band was performed using a resonator sample with a quite low conversion efficiency, due to the low generated SH power. The photorefraction was measured to be greatly reduced compared with Ti and Zn waveguides.

- APE waveguides in MgO-doped CLN.

  Finally, APE waveguides were fabricated in bulk MgO-doped lithium niobate. Due to non-ideal exchange conditions, the waveguiding was even weaker than in the APE:CLN waveguides. Still, the waveguide losses were quite low. The SHG efficiency was measured to be not very large. Hardly any photorefraction was visible in this type of waveguide, even at room temperature.

Pros and cons of the fabricated waveguides as well as possible measures to improve their quality are listed in Tab. 11.1. Fig. 11.1 shows again the overview of the photorefraction which was measured in the waveguides of different type. The photorefractive sensitivity S was simply defined here as the index change normalized to the effective mode area.

The titanium-indiffused waveguides show a high photorefractive sensitivity and are therefore not suited for nonlinear optical applications at low temperatures. The zinc waveguides show a reduced—compared with Ti waveguides—but still significant photorefraction at room temperature. However, zinc waveguides are easier to fabricate, requiring just a diffusion step after lithography and the deposition of a metal layer. The APE method requires the exchange step with a more delicate setup and the annealing step and is more time-consuming in total. But concerning photorefraction, APE waveguides in undoped or MgO-doped $LiNbO_3$ are the waveguides of choice for high-power nonlinear devices.

Table 11.1.: Pros and cons of the waveguides fabricated in this work (not necessarily in general) and possible measures to improve their performances

Waveguide	⊕ Pros	⊖ Cons	! Actions
Ti:CLN and MgO indiffudion		· waveguides unusable due to high loss	· shorter Ti diffusion and longer MgO diffusion
Ti:MgO:CLN	· established fabrication technique · successful UV assisted poling	· low mode overlap for SHG · no reduction of photorefraction observed	· refine diffusion conditions · try diffusion in wet atmosphere
Ti:MgO:SLN	· established fabrication technique	· inferior domain grating quality · low mode overlap for SHG · no reduction of photorefraction observed	· increase charge or try pulsed poling technique · refine diffusion conditions · try diffusion in wet atmosphere
Zn:CLN	· standard waveguide fabrication technique · low loss waveguides possible · little photorefraction	· low mode overlap for SHG	· refine diffusion conditions
APE:CLN	· low loss waveguides possible · very little photorefraction	· waveguide quality variable · low mode overlap for SHG · more complicated waveguide fabrication	· improve lithography · refine exchange and annealing conditions
APE:MgO:CLN	· low loss waveguides possible · extremely low photorefraction	· low mode overlap for SHG · more complicated waveguide fabrication	· refine exchange and annealing conditions

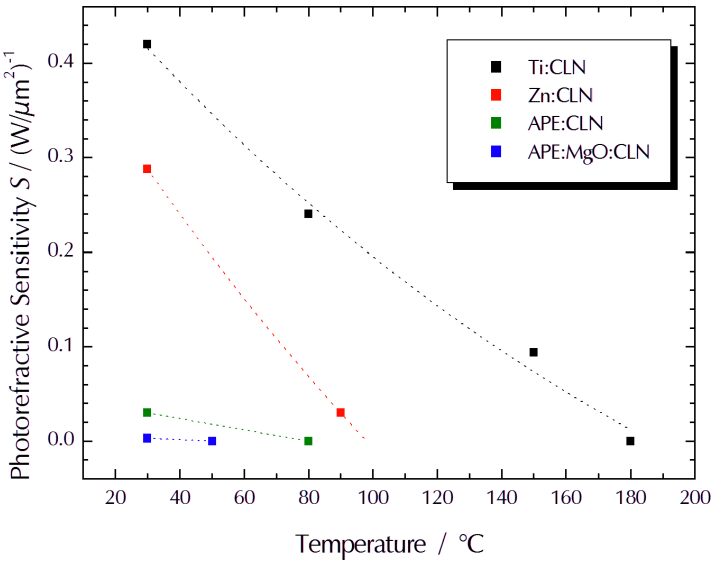

Figure 11.1.: Comparison of the photorefractive sensitivities of the different waveguide types. The sensitivity S is defined here as index change Δn normalised to the light intensity inside the waveguide given in $^{W}/_{\mu m^2}$. The dotted lines are mere guides to the eye.

Possible Future Activities

A number of options exist for further development of integrated optic waveguides having low photorefractive sensitivity.

The first step for improving the quality of the APE waveguides in undoped and especially in doped lithium niobate is the refinement of exchange and annealing conditions. Proper conditions, leading to better wave confinement, smaller mode sizes and higher overlap between optical modes in fibres and waveguides as well as between fundamental and second harmonic modes, have to be found. This applies also to the Zn-indiffused waveguides.

As the proton exchanged waveguides in MgO-doped $LiNbO_3$ seems to be the most promising candidate, further investigations on the properties of these waveguides will be useful. Determining hydrogen concentration profiles might be possible non-destructively by micro-raman measurements, because several bands (e. g. $69\,cm^{-1}$, $253\,cm^{-1}$) depend on the H concentration [125, 126]. Refractive index profiles and their dispersion can be obtained by m-line spectroscopy, as already described in Section 7.1. A detailed waveguide model could thus be set up, allowing further optimisation as well as more precise predictions of the phase matching conditions.

Another way for the fabrication of proton exchanged waveguides could also be considered. Instead of using pure acid, the exchange can be carried out with a diluted acid. This method directly results in α-phase waveguides, eliminating

the need for the time-consuming annealing step. However, the exchange times then become significantly longer, so using low temperatures of $\approx 160\,°C$ might be impractical due to the low exchange coefficient. A possible solution is the use of an acid having a significantly higher boiling point, e. g. stearic acid [90]. However, a different setup for performing the proton exchange will be needed when using higher temperatures.

A waveguide type also worth considering are the so-called reverse proton exchanged waveguides. They are fabricated by exchanging the surface-near protons of APE waveguides by lithium using an lithium-containing eutectic melt [118]. This procedure results in buried waveguides having more symmetric field profiles, resulting in a high mode overlap and in a better nonlinear-optical conversion efficiency.

Finally, the origin of the photorefraction, i. e. the Fe^{2+} impurities, can be addressed. If the number of oxidisable impurities is reduced, i. e. if the ratio of non-ionised and ionised Fe centres $c_{Fe^{2+}}/c_{Fe^{3+}}$ is reduced, the index changes caused by the photorefractive effect can be expexted to decrease. Falk et al. [127] report successful oxidisations of $LiNbO_3$ crystals, using a thermoelectric oxidisation method, leading to an optical damage which was reduced by one order of magnitude. It would be insightful to conduct such experiments also using Ti or Zn waveguide samples and compare their photorefractive sensitivities before and after an oxidisation treatment.

A. Photo Masks

Masks #1 and #2

The waveguide separations are identical for the masks #1 and #2. The waveguide widths, however, differ. The widths of the mask #1 are a: 5 µm, b: 6 µm and c: 7 µm. The widths of the structure #2, used for the fabrication of proton exchanged waveguides, are: 1a: 8 µm, 1b: 7.5 µm . . . 3c: 4 µm, 4a: 8 µm, 4b: 7.5 µm . . . 5c: 5.5 µm (repeated four times for the groups 6. . . 25).

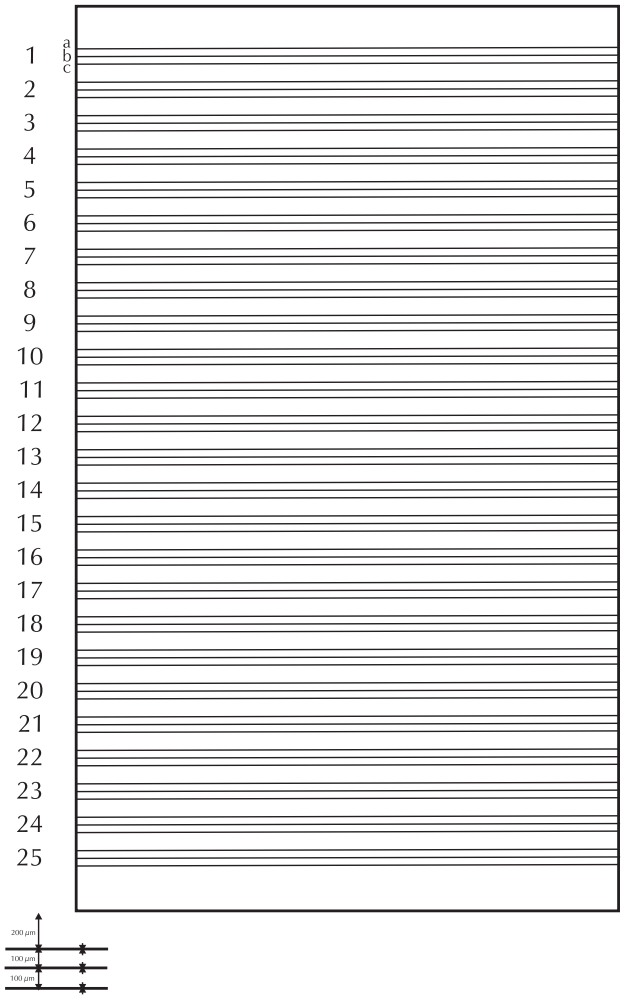

Mask #3

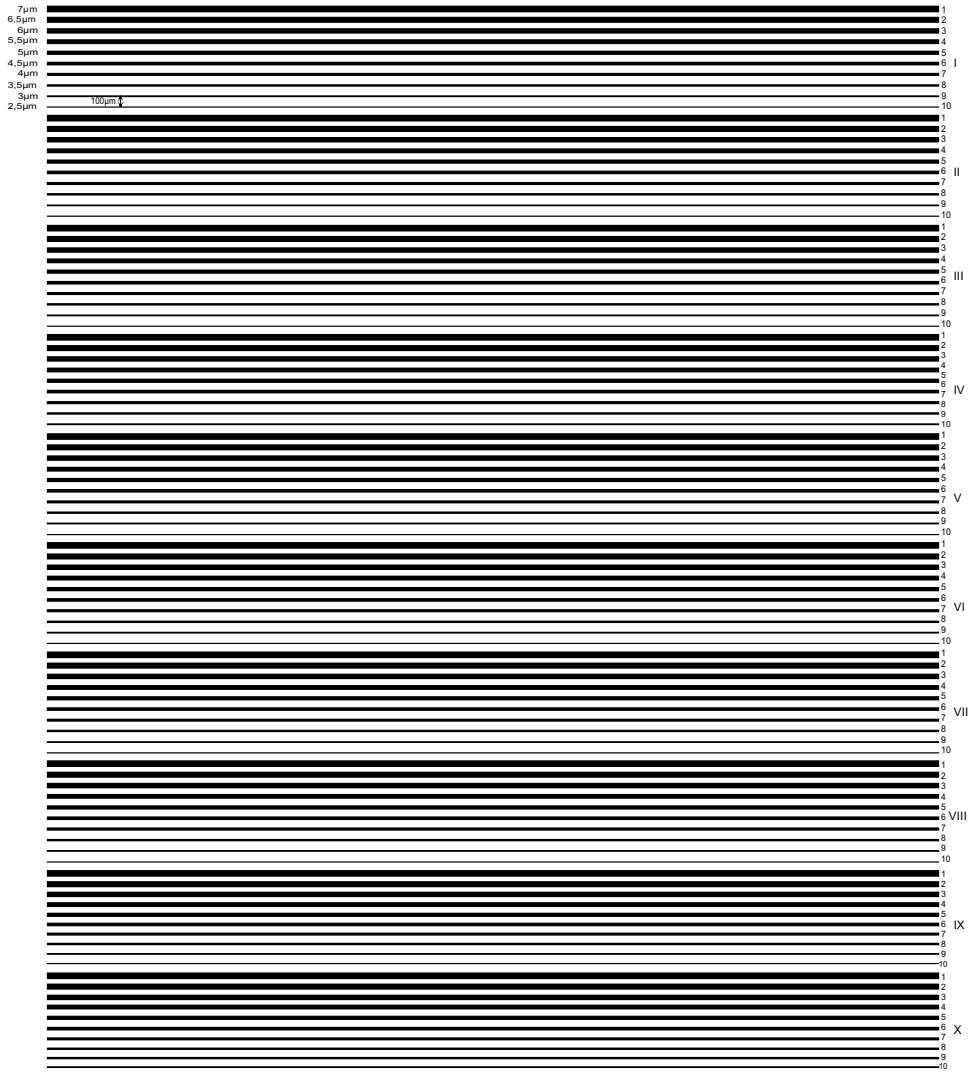
7µm
6,5µm
6µm
5,5µm
5µm
4,5µm
4µm
3,5µm
3µm
2,5µm
100µm
I
II
III
IV
V
VI
VII
VIII
IX
X

Abbreviations

AOWC	All-Optical Wavelength Converter/Conversion
APE	Annealed Proton Exchanged
ASE	Amplified Spontaneous Emission
CLN	Congruent (or Congruently melting) Lithium Niobate
DCCZ	Double-Crucible Czochralski growth
DFG	Difference Frequency Generation
DWDM	Dense Wavelength Division Multiplexing
ECL	External (or Extended) Cavity Laser
FWHM	Full Width at Half Maximum
ITU	International Telecommunication Union
MIR	Mid-wavelength Infrared (3000 nm . . . 50000 nm)
NIR	Near Infrared (780 nm . . . 1400 nm)
OSA	Optical Spectrum Analyser
PPLN	Periodically Poled Lithium Niobate
SFG	Sum Frequency Generation
SHG	Second Harmonic Generation
SLN	Stoichiometric Lithium Niobate
SVEA	Slowly Varying Amplitude Approximation
SWIR	Short-wavelength Infrared (1400 nm . . . 3000 nm)
THG	Third Harmonic Generation
TSSG	Top-Seeded Solution Growth
WDM	Wavelength Division Multiplexing

Bibliography

[1] J. Yamawaku, H. Takara, T. Ohara, K. Sato, A. Takada, T. Morioka, O. Tadanaga, H. Miyazawa, and M. Asobe: "Simultaneous 25 GHz-spaced DWDM wavelength conversion of 1.03 Tbit/s (103 $\times$ 10 Gbit/s) signals in PPLN waveguide", Electronics Letters, **39**(15), 1144–1145 (July 2003), URL http://dx.doi.org/10.1049/el:20030719

[2] A. Räuber: "Chemistry and Physics of Lithium Niobate", in E. Kaldis (Editor), "Current Topics in Materials Science, Volume 1", pp. 481–601 (North-Holland Publishing Company, Amsterdam, 1978)

[3] V. Gericke, P. Hertel, E. Krätzig, J. P. Nisius, and R. Sommerfeldt: "Light-Induced Refractive Index Changes in $LiNbO_3$:Ti Waveguides", Applied Physics B, **44**(3), 155–162 (November 1987), URL http://dx.doi.org/10.1007/BF00692317

[4] D. A. Bryan, R. Gerson, and H. E. Tomaschke: "Increased optical damage resistance in lithium niobate", Applied Physics Letters, **44**(9), 847–849 (May 1984), URL http://link.aip.org/link/?APPLAB/44/847/1

[5] D. A. Bryan, R. R. Rice, R. Gerson, H. E. Tomaschke, K. L. Sweeney, and L. E. Halliburton: "Magnesium-doped lithium niobate for higher optical power applications", Optical Engineering, **24**(1), 138–143 (January 1985)

[6] Y. Furukawa, K. Kitamura, and S. Takekawa: "Stoichiometric Mg:$LiNbO_3$ as an effective material for nonlinear optics", Optics Letters, **23**(24), 1892–1894 (December 1998), URL http://www.opticsinfobase.org/ol/abstract.cfm?URI=ol-23-24-1892

[7] Y. Furukawa, K. Kitamura, A. Alexandrovski, R. K. Route, M. M. Fejer, and G. Foulon: "Green-induced infrared absorption in MgO doped $LiNbO_3$", Applied Physics Letters, **78**(14), 1970–1972 (April 2001), URL http://link.aip.org/link/?APPLAB/78/1970/1

[8] T. R. Volk, V. I. Pryalkin, and N. M. Rubinina: "Optical-damage-resistant $LiNbO_3$:Zn crystal", Optics Letters, **15**(18), 996–998 (September 1990), URL http://www.opticsinfobase.org/ol/abstract.cfm?URI=ol-15-18-996

[9] J. Jackel, A. M. Glass, G. E. Peterson, C. E. Rice, D. H. Olson, and J. J. Veselka: "Damage-resistant $LiNbO_3$ waveguides", Journal of Applied Physics, **55**(1), 269–270 (January 1984), URL http://link.aip.org/link/?JAPIAU/55/269/1

[10] T. Fujiwara, R. Srivastava, X. Cao, and R. V. Ramaswamy: "Comparison of photrefractive index change in proton-exchanged and Ti-diffused $LiNbO_3$ waveguides", Optics Letters, **18**(5), 346–348 (March 1993), URL http://www.opticsinfobase.org/ol/abstract.cfm?URI=ol-18-5-346

[11] W. Grundkötter: Dynamik nichtlinearer Wechselwirkungen zweiter Ordnung in integriert optischen Wellenleitern, Ph.D. thesis, Universität Paderborn (2006)

[12] S. K. Korotky, W. J. Minford, L. L. Buhl, M. D. Divino, and R. C. Alferness: "Mode Size and Method for Estimating the Propagation Constant of Single-Mode Ti:$LiNbO_3$ Strip Waveguides", IEEE Transactions on Microwave Theory and Techniques, **30**(10), 1784–1789 (October 1982), URL http://ieeexplore.ieee.org/xpl/freeabs_all.jsp?isnumber=25109&arnumber=1131321&count=58&index=51

[13] G. Hocker and W. K. Burns: "Mode dispersion in diffused channel waveguides by the effective index method", Applied Optics, **16**(1), 113–118 (January 1977), URL http://www.opticsinfobase.org/ao/abstract.cfm?URI=ao-16-1-113

[14] E. Strake: Numerische Analyse integriert optischer Komponenten in $LiNbO_3$ mit der Theorie gekoppelter Moden, Ph.D. thesis, Universität-GH Paderborn (1991)

[15] P. A. Franken, A. E. Hill, C. W. Peters, and G. Weinreich: "Generation of Optical Harmonics", Physics Review Letters, **7**(4), 118–119 (August 1961), URL http://link.aps.org/abstract/PRL/v7/p118

[16] J. A. Armstrong, N. Bloembergen, J. Ducuning, and P. S. Pershan: "Interactions between light waves in a nonlinear dielectric", Physical Review, **127**(6), 1918–1939 (September 1962), URL http://link.aps.org/abstract/PR/v127/p1918

[17] R. W. Boyd: Nonlinear Optics (Academic Press, 2003), 2nd edition

[18] A. Yariv: Quantum Electronics (Wiley, 1989), 3rd edition

[19] G. Schreiber: Quasi-phasenangepaßte Frequenzkonversion mit periodisch gepolten Ti:$LiNbO_3$ Wellenleitern, Ph.D. thesis, Universität Paderborn (2001)

[20] A. Ashkin, G. D. Boyd, J. M. Dziedzic, R. G. Smith, A. A. Ballman, J. J. Levinstein, and K. Nassau: "Optically-induced refractive index inhomogeneities in $LiNbO_3$ and $LiTaO_3$", Applied Physics Letters, **9**(1), 72–74 (July 1966), URL http://dx.doi.org/10.1063/1.1754607

[21] F. S. Chen, J. T. LaMacchia, and D. B. Fraser: "Holographic Storage in Lithium Niobate", Applied Physics Letters, **13**(7), 223–225 (October 1968), URL http://link.aip.org/link/?APPLAB/13/223/1

[22] F. S. Chen: "Optically Induced Change of Refractive Indices in $LiNbO_3$ and $LiTaO_3$", Journal of Applied Physics, **40**(8), 3389–3396 (July 1969), URL http://link.aip.org/link/?JAPIAU/40/3389/1

[23] P. Yeh: Introduction to Photorefractive Nonlinear Optics (Wiley, New York, 1993)

[24] K. Buse: "Light-induced charge transport processes in photorefractive crystals I: Models and experimental methods", Applied Physics B, **64**(3), 273–291 (February 1997), URL http://dx.doi.org/10.1007/s003400050175

[25] A. M. Glass, D. von der Linde, and T. J. Negran: "High-voltage bulk photovoltaic effect and the photorefractive process in $LiNbO_3$", Applied Physics Letters, **25**(4), 233–235 (August 1974), URL http://link.aip.org/link/?APPLAB/25/233/1

[26] V. M. Fradkin and R. M. Magomadov: "Anomalous photovoltaic effect in $LiNbO_3$:Fe in polarized light", JETP Letters, **30**(11), 686–688 (1979), URL http://www.jetpletters.ac.ru/ps/1370/article_20739.shtml

[27] V. I. Belinicher, V. K. Malinovskiĭ, and B. I. Sturman: "Photogalvanic effect in a crystal with polar axis", Sov. Phys. JETP, **46**(2), 362–366 (August 1977)

[28] N. V. Kukhtarev, V. B. Markov, S. G. Odulov, M. S. Soskin, and V. L. Vinetskii: "Holographic Storage in Electrooptic Crystals. I. Steady State", Ferroelectrics, **22**, 949–960 (1979)

[29] F. Jermann and J. Otten: "Light-induced charge transport in $LiNbO_3$:Fe at high light intensities", Journal of the Optical Society of America B, **10**(11), 2085–2092 (November 1993), URL http://www.opticsinfobase.org/josab/abstract.cfm?URI=josab-10-11-2085

[30] Properties of Lithium Niobate, EMIS Datareviews Series No. 5 (INSPEC, 1989)

[31] R. S. Weis and T. K. Gaylord: "Lithium Niobate: Summary of Physical Properties and Crystal Structure", Applied Physics A, **37**(4), 191–203 (August 1985), URL http://dx.doi.org/10.1007/BF00614817

[32] Y. S. Kuz'minov: Lithium Niobate Crystals (Cambridge International Science Publishing, 1999)

[33] Crystal Technology, Inc.: "Lithium Niobate Data Sheet", URL `http://www.crystaltechnology.com/docs/LN_LTAppNote.pdf`

[34] K. Kitamura, J. K. Yamamoto, N. Iyi, S. Kimura, and T. Hayashi: "Stoichiometric $LiNbO_3$ single crystal growth by double crucible Czochralski method using automatic powder supply system", Journal of Crystal Growth, **116**(3–4), 327–332 (February 1992), URL `http://dx.doi.org/10.1016/0022-0248(92)90640-5`

[35] Y. Furukawa, M. Sato, K. Kitamura, and F. Nitanda: "Growth and characterization of off-congruent $LiNbO_3$ single crystals grown by the double crucible method", Journal of Crystal Growth, **128**(1–4), 909–914 (March 1993), URL `http://dx.doi.org/10.1016/S0022-0248(07)80068-6`

[36] K. Polgár, . Péter, I. Földvári, and Z. Szaller: "Structural defects in flux-grown stoichiometric $LiNbO_3$ single crystals", Journal of Crystal Growth, **218**(2–4), 327–333 (September 2000), URL `http://dx.doi.org/10.1016/S0022-0248(00)00600-X`

[37] R. L. Holman et al.: "Chemical control of optical damage in lithium niobate", Applied Physics Letters, **32**(5), 280–283 (March 1978), URL `http://link.aip.org/link/?APPLAB/32/280/1`

[38] P. F. Bordui, R. G. Norwood, D. H. Jundt, and M. M. Fejer: "Preparation and characterization of off-congruent lithium niobate crystals", Journal of Applied Physics, **71**(2), 875–879 (January 1992), URL `http://link.aip.org/link/?JAPIAU/71/875/1`

[39] L. O. Svaasand, M. Eriksrud, A. P. Grande, and F. Mo: "Crystal growth and properties of $LiNb_3O_8$", Journal of Crystal Growth, **18**, 179–184 (1973), URL `http://dx.doi.org/10.1016/0022-0248(73)90197-8`

[40] V. Gopalan, T. E. Mitchell, Y. Furukawa, and K. Kitamura: "The role of nonstiochiometry in 180° domain switching of $LiNbO_3$ crystals", Applied Physics Letters, **72**(16), 1981–1983 (April 1998)

[41] S. C. Abrahams and P. Marsh: "Defect Structure Dependence on Composition in Lithium Niobate", Acta Crystallograpica B, **42**, 61–68 (February 1986)

[42] D. P. Birnie III: "Analysis of diffusion in lithium niobate", Journal of Material Science, **28**, 302–315 (1993)

[43] G. Malovichko, V. Grachev, and O. Schirmer: "Interrelation of intrinsic and extrinsic defects – congruent, stoichiometric, and regularly ordered lithium niobate", Applied Physics B, **68**, 785–793 (1999)

[44] F. P. Safaryan, R. S. Feigelson, and A. M. Petrosyan: "An approach to the defect structure analysis of lithium niobate single crystals", Journal of Applied Physics, **85**(12), 8079–8082 (June 1999)

[45] G. J. Edwards and M. Lawrence: "A temperature-dependent dispersion equation for congruently grown lithium niobate", Optical and Quantum Electronics, **16**(4), 373–375 (July 1984), URL http://dx.doi.org/10.1007/BF00620081

[46] U. Schlarb and K. Betzler: "Influence of the defect structure on the relative indices of undoped and Mg-doped lithium niobate", Physical Review B, **50**(2), 751–757 (July 1994), URL http://link.aps.org/abstract/PRB/v50/p751

[47] I. Shoji, T. Kondo, A. Kitamoto, M. Shirane, and R. Ito: "Absolute scale of second-order nonlinear-optical coefficients", Journal of the Optical Society of America B, **14**(9), 2268–2294 (September 1997), URL http://www.opticsinfobase.org/abstract.cfm?URI=josab-14-9-2268

[48] K. Buse: "Light-induced charge transport processes in photorefractive crystals II: Materials", Applied Physics B, **64**(4), 391–407 (March 1997), URL http://dx.doi.org/10.1007/s003400050190

[49] B. K. Das: Integrated optical distributed Bragg reflector and distributed feedback lasers in Er:$LiNbO_3$ waveguides with photorefractive gratings, Ph.D. thesis, Universität Paderborn (2003)

[50] T. Volk, N. Rubinina, and M. Wöhlecke: "Optical-damage-resistant impurities in lithium niobate", Journal of the Optical Society of America B, **11**(9), 1681–1687 (September 1994), URL http://josab.osa.org/abstract.cfm?id=7783

[51] T. Fujiwara, X. Cao, R. Srivastava, and R. V. Ramaswamy: "Photorefractive effect in annealed proton-exchanged $LiNbO_3$ waveguides", Applied Physics Letters, **61**(7), 743–745 (August 1992), URL http://dx.doi.org/10.1063/1.107784

[52] Y. Kong, S. Liu, Y. Zhao, H. Liu, S. Chen, and J. Xu: "Highly optical damage resistant crystal: Zirconium-oxide-doped lithium niobate", Applied Physics Letters, **91**(8), 081908 (2007), URL http://link.aip.org/link/?APPLAB/91/081908/1

[53] M. Nakamura, S. Takekawa, Y. Liu, and K. Kitamura: "Optical Damage Resistance of Near-Stoichiometric $LiNbO_3$ Crystal Doped with Sc", Japanese Journal of Applied Physics, **43**(7B), L947–L949 (2004), URL http://jjap.ipap.jp/link?JJAP/43/L947/

[54] E. P. Kokanyan, L. Razzari, I. Cristiani, V. Degiorgio, and J. B. Gruber: "Reduced photorefraction in hafnium-doped single-domain and periodically poled lithium niobate crystals", Applied Physics Letters, **84**(11), 1880–1882 (March 2004), URL http://link.aip.org/link/?APPLAB/84/1880/1

[55] R. V. Schmidt and I. P. Kaminow: "Metal-diffused optical waveguides in $LiNbO_3$", Applied Physics Letters, **25**(8), 458–460 (October 1974), URL http://link.aip.org/link/?APPLAB/25/458/1

[56] M. Fukuma, J. Noda, and H. Iwasaki: "Optical properties in titanium-diffused $LiNbO_3$ strip waveguides", Journal of Applied Physics, **49**(7), 3693–3698 (July 1978), URL http://link.aip.org/link/?JAPIAU/49/3693/1

[57] W. K. Burns, P. H. Klein, E. J. West, and L. E. Plew: "Ti diffusion in Ti:$LiNbO_3$ planar and channel optical waveguides", Journal of Applied Physics, **50**(10), 6175–6182 (October 1979), URL http://link.aip.org/link/?JAPIAU/50/6175/1

[58] H. Lüdtke, W. Sohler, and H. Suche: "Characterization of Ti:$LiNbO_3$ Optical Waveguides", in R. T. Kersten and R. Ulrich (Editors), "Dig. Workshop Integrated Optics", pp. 122–126 (Berlin, 1980)

[59] E. Strake, G. P. Bava, and I. Montrosset: "Guided Modes of Ti:$LiNbO_3$ Channel Waveguides: A Novel Quasi-Analytical Technique in Comparison with the Scalar Finite-Element Method", Journal of Lightwave Technology, **6**(6), 1126–1135 (June 1988), URL http://dx.doi.org/10.1109/50.4105

[60] H. Herrmann: Optisch nichtlineare Differenzfrequenzerzeugung abstimmbarer, kohärenter Strahlung im mittleren Infrarotbereich in Ti:$LiNbO_3$-Streifenwellenleitern, Ph.D. thesis, Universität-GH Paderborn (1991)

[61] F. Caccavale, F. Gonella, A. Quaranta, and I. Mansour: "Analysis of Ti:$LiNbO_3$ waveguides using secondary ion mass spectrometry and near field method", Electronics Letters, **31**(13), 1054–1056 (June 1995), URL http://ioj.iee.org.uk/journals/el/1995/13/19950732.html

[62] M. Fukuma and J. Noda: "Optical properties of titanium-diffused $LiNbO_3$ strip waveguides and their coupling-to-a-fiber characteristics", Applied Optics, **19**(4), 591–597 (February 1980), URL http://ao.osa.org/abstract.cfm?id=23762

[63] O. Eknoyan, D. W. Yoon, and H. F. Taylor: "Low-loss optical waveguides in lithium tantalate by vapor diffusion", Applied Physics Letters, **51**, 384–386 (August 1987), URL http://link.aip.org/link/?APPLAB/51/384/1

[64] B. Herreros and G. Lifante: "$LiNbO_3$ optical waveguides by Zn diffusion from vapor phase", Applied Physics Letters, **66**(12), 1449–1451 (March 1995), URL http://link.aip.org/link/?APPLAB/66/1449/1

[65] W. M. Young, R. S. Feigelson, M. M. Fejer, M. J. F. Digonnet, and H. J. Shaw: "Photorefractive-damage-resistant Zn-diffused waveguides in MgO:LiNbO3", Optics Letters, **16**(13), 995–997 (July 1991), URL http://ol.osa.org/abstract.cfm?id=10663

[66] L. Ming: Fabrication And Applications Of Zinc Indiffused Channel Waveguides in Periodically Poled Lithium Niobate, Ph.D. thesis, University of Southampton (May 2005)

[67] M. C. Hübner: "Charakterisierung Zn-diffundierter $LiNbO_3$-Wellenleiter", (2000). Wahlpflichtpraktikum, unpublished results

[68] U. Schlarb, M. Wöhlecke, B. Gather, A. Reichert, K. Betzler, T. Volk, and N. Rubinina: "Refractive indices of Zn-doped lithium niobate", Optical Materials, **4**(6), 791–795 (October 1995), URL http://dx.doi.org/10.1016/0925-3467(95)00018-6

[69] G. D. Boyd, R. V. Schmidt, and F. G. Storz: "Characteristics of metal-diffused $LiNbO_3$ for acoustic devices", Journal of Applied Physics, **48**(7), 2880–2881 (July 1977), URL http://link.aip.org/link/?JAPIAU/48/2880/1

[70] W. M. Young, M. M. Fejer, M. J. F. Digonnet, A. F. Marshall, and R. S. Feigelson: "Fabrication, Characterization and Index Profile Modeling of High-Damage Resistance Zn-Diffused Waveguides in Congruent and MgO: Lithium Niobate", Journal of Lightwave Technology, **10**(9), 1238–1246 (September 1992), URL http://dx.doi.org/10.1109/50.156875

[71] E. Cantelar, R. E. di Paolo, J. A. Sanz-García, P. L. Pernas, R. Nevado, G. Lifante, and F. Cussó: "Second-harmonic Generation in Zn-diffused periodically poled $LiNbO_3$ Channel Waveguides", Applied Physics B, **73**(5–6), 515–517 (October 2001), URL http://dx.doi.org/10.1007/s003400100716

[72] M. Domenech, R. E. D. Paolo, G. Lifante, and F. Cussó: "Blue Light by SHG in Diode Pumped $LiNbO_3$ Waveguides", physica status solidi (a), **192**(1), 135–138 (July 2002)

[73] M. Asobe, H. Miyazawa, O. Tadanaga, Y. Nishida, and H. Suzuki: "A Highly Damage-Resistant Zn:$LiNbO_3$ Ridge Waveguide and its Application to a Polarization-Independent Wavelength Converter", Journal of Quantum Electronics, **39**(10), 1327–1333 (October 2003), URL http://dx.doi.org/10.1109/JQE.2003.817243

[74] J. L. Jackel and C. E. Rice: "Topotactic $LiNbO_3$ to cubic perovskite structural transformation in $LiNbO_3$ and $LiTaO_3$", Ferroelectrics, **38**(1), 801–804 (October 1981), URL http://dx.doi.org/10.1080/00150198108209543

[75] J. L. Jackel, C. E. Rice, and J. J. Veselka: "Proton-exchange for high-index waveguides in $LiNbO_3$", Applied Physics Letters, **41**(7), 607–608 (October 1982), URL http://link.aip.org/link/?APPLAB/41/607/1

[76] J. Olivares and J. M. Cabrera: "Guided modes with ordinary refractive index in proton exchanged $LiNbO_3$ waveguides", Applied Physics Letters, **62**(20), 2468–2470 (May 1993), URL http://link.aip.org/link/?APPLAB/62/2468/1

[77] A. Yi-Yan: "Index instabilities in proton-exchanged $LiNbO_3$ waveguides", Applied Physics Letters, **42**(8), 633–635 (April 1983), URL http://link.aip.org/link/?APPLAB/42/633/1

[78] J. L. Jackel and C. E. Rice: "Short- and long-term stability in proton exchanged lithium niobate waveguides", SPIE Proceedings, **460**, 43–48 (1984)

[79] G. Hagner and T. Bachmann: "Refractive Index Profiles and Exchange Ratios of Proton-Exchanged Waveguides in Congruent and MgO-Doped $LiNbO_3$", physica status solidi (a), **165**(1), 205–212 (January 1998), URL http://www3.interscience.wiley.com/cgi-bin/abstract/40000789/ABSTRACT

[80] C. E. Rice: "The structure and properties of $Li_{1-x}H_xNbO_3$", Journal of Solid State Chemistry, **64**(2), 188–199 (September 1986), URL http://dx.doi.org/10.1016/0022-4596(86)90138-6

[81] Y. N. Korkishko and V. A. Fedorov: "Relationship between refractive indices and hydrogen concentration in proton exchanged $LiNbO_3$ waveguides", Journal of Applied Physics, **82**(3), 1010–1017 (August 1997), URL http://link.aip.org/link/?JAPIAU/82/1010/1

[82] M. De Micheli, J. Botineau, S. Neveu, P. Sibillot, and D. B. Ostrowsky: "Independent control of index and profiles in proton-exchanged lithium niobate guides", Optics Letters, **8**(2), 114–115 (February 1983), URL http://ol.osa.org/abstract.cfm?&id=7925

[83] R. A. Becker: "Comparison of guided-wave interferometric modulators fabricated on $LiNbO_3$ via Ti indiffusion and proton exchange", Applied Physics Letters, **43**(2), 131–133 (July 1983), URL http://link.aip.org/link/?APPLAB/43/131/1

[84] P. G. Suchoski, T. K. Findakly, and F. J. Leonberger: "Stable low-loss proton-exchanged $LiNbO_3$ waveguide devices with no electro-optic degradation", Optics Letters, **13**(11), 1050–1052 (November 1988), URL http://ol.osa.org/abstract.cfm?&id=9448

[85] M. L. Bortz, L. A. Eyres, and M. M. Fejer: "Depth profiling of the d_{33} nonlinear coefficient in annealed proton exchanged $LiNbO_3$ waveguides", Applied Physics Letters, **62**(17), 2012–2014 (April 1993), URL http://dx.doi.org/10.1063/1.109519

[86] D. F. Clark, A. C. G. Nutt, K. K. Wong, P. J. R. Laybourn, and R. M. D. L. Rue: "Characterization of proton-exchange slab optical waveguides in z-cut $LiNbO_3$", Journal of Applied Physics, **54**(11), 6218–6220 (November 1983), URL http://link.aip.org/link/?JAPIAU/54/6218/1

[87] M. L. Bortz and M. M. Fejer: "Annealed proton-exchanged $LiNbO_3$ waveguides", Optics Letters, **16**(23), 1844–1846 (December 1991), URL http://ol.osa.org/abstract.cfm?id=10892

[88] J. M. White and P. F. Heidrich: "Optical waveguide refractive index profiles determined from measurement of mode indices: a simple analysis", Applied Optics, **15**(1), 151–155 (January 1976), URL http://www.opticsinfobase.org/ao/abstract.cfm?URI=ao-15-1-151

[89] R. V. Roussev: Optical-Frequency Mixers in Periodically Poled Lithium Niobate: Materials, Modeling and Characterization, Ph.D. thesis, Standford University (December 2006), URL http://www.stanford.edu/group/fejer/cgi-bin/publications.php#DISS

[90] Y. N. Korkishko, V. A. Fedorov, and O. Y. Feoktistova: "$LiNbO_3$ Optical Waveguide Fabrication by High-Temperature Proton Exchange", Journal of Lightwave Technology, **18**(4), 562–568 (April 2000), URL http://www.opticsinfobase.org/abstract.cfm?id=65782

[91] K. Yamamoto, H. Yamamoto, and T. Taniuchi: "Simultaneous sum-frequency and second-harmonic generation from a proton-exchanged MgO-doped $LiNbO_3$ waveguide", Applied Physics Letters, **58**(12), 1227–1229 (March 1991), URL http://dx.doi.org/10.1063/1.104370

[92] D. Feng, N.-B. Ming, J.-F. Hong, Y.-S. Yang, J.-S. Zhu, Z. Yang, and Y.-N. Wang: "Enhancement of second-harmonic generation

in $LiNbO_3$ crystals with periodic laminar ferroelectric domains", Applied Physics Letters, **37**(7), 607–609 (October 1980), URL http://link.aip.org/link/?APPLAB/37/607/1

[93] E. J. Lim, M. M. Fejer, and R. L. Byer: "Second-harmonic generation of green light in periodically poled planar lithium niobate waveguide", Electronics Letters, **25**(3), 174–175 (February 1989), URL http://dx.doi.org/10.1049/el:19890127

[94] M. Yamada, N. Nada, M. Saitoh, and K. Watanabe: "First-order quasi-phase matched $LiNbO_3$ waveguide periodically poled by applying an external field for efficient blue second-harmonic generation", Applied Physics Letters, **62**(5), 435–436 (February 1993), URL http://link.aip.org/link/?APPLAB/62/435/1

[95] V. Gopalan and M. C. Gupta: "Origin and characteristics of internal fields in $LiNbO_3$ crystals", Ferroelectrics, **198**(1), 49–59 (June 1997), URL http://dx.doi.org/10.1080/00150199708228337

[96] V. Shur, E. Rumyantsev, R. Batchko, G. Miller, M. Fejer, and R. Byer: "Physical basis of the domain engineering in the bulk ferroelectrics", Ferroelectrics, **221**(1), 157–167 (January 1999), URL http://dx.doi.org/10.1080/00150199908016450

[97] Y. L. Lee, H. Suche, G. Schreiber, R. Ricken, V. Quiring, and W. Sohler: "Periodical domain inversion in singlemode Ti:MgO:$LiNbO_3$ channel waveguides", Electronics Letters, **38**(15), 812–813 (July 2002), URL http://dx.doi.org/10.1049/el:20020545

[98] M. Fujimura, T. Sohmura, and T. Suhara: "Fabrication of domain-inverted gratings in MgO:$LiNbO_3$ by applying voltage under ultraviolet irradiation through photomask at room temperature", Electronics Letters, **39**(9), 719–721 (May 2003), URL http://dx.doi.org/10.1049/el:20030492

[99] M. C. Wengler, U. Heinemeyer, E. Soergel, and K. Buse: "Ultraviolet light-assisted domain inversion in magnesium-doped lithium niobate crystals", Journal of Applied Physics, **98**(6), 064104 (September 2005), URL http://dx.doi.org/10.1063/1.2058184

[100] Y. L. Lee, private communication

[101] Christian Schemel, private communication

[102] H. Moritz: "Optical Single Layer Lift-off Process", IEEE Transactions on Electron Devices, **32**(3), 672–676 (March 1985), URL http://ieeexplore.ieee.org/xpl/freeabs_all.jsp?isnumber=31925&arnumber=1484743&count=35&index=22

[103] K. R. Parameswaran, J. R. Kurz, R. V. Roussev, and M. M. Fejer: "Observation of 99% pump depletion in single-pass second-harmonic generation in a periodically poled lithium niobate waveguide", Optics Letters, **27**(1), 43–45 (January 2002), URL http://www.opticsinfobase.org/ol/abstract.cfm?URI=ol-27-1-43

[104] K. R. Parameswaran: Highly Efficient Optical Frequency Mixers, Ph.D. thesis, Standford University (May 2002), URL http://www.stanford.edu/group/fejer/cgi-bin/publications.php#DISS

[105] R. Regener and W. Sohler: "Loss in Low-Finesse Ti:$LiNbO_3$ Optical Waveguide Resonators", Applied Physics B, **36**, 143–147 (1985)

[106] F. Caccavale, P. Chakraborty, A. Capobianco, G. Gianello, and I. Mansour: "Characterization and optimization of Ti-diffused $LiNbO_3$ optical waveguides by second diffusion of magnesium", Journal of Applied Physics, **78**(1), 187–193 (July 1995), URL http://link.aip.org/link/?JAPIAU/78/187/1

[107] F. Caccavale, P. Chakraborty, I. Mansour, G. Gianello, M. Mazzoleni, and M. Elena: "A secondary-ion-mass spectrometry study of magnesium diffusion in lithium niobate", Journal of Applied Physics, **76**(11), 7552–7558 (December 1994), URL http://link.aip.org/link/?JAPIAU/76/7552/1

[108] K. Komatsu, M. Kondo, and Y. Ohta: "Titanium/magnesium double diffusion method for efficient fibre-$LiNbO_3$ waveguide coupling", Electronics Letters, **22**(17), 881–882 (August 1986), URL http://dx.doi.org/10.1049/el:19860600

[109] T. Bremer, P. Hertel, S. Oelschig, R. Sommerfeldt, and W. Heiland: "Depth Profiling of Magnesium-doped $LiNbO_3$ Waveguides", Thin Solid Films, **175**, 235–239 (August 1989), URL http://dx.doi.org/10.1016/0040-6090(89)90833-X

[110] R.-H. Kim, H.-H. Park, and G.-T. Joo: "Cation diffusion characteristics in MgO-doped $LiNbO_3$ during Ti diffusion", Applied Surface Science, **169–170**, 570–574 (January 2001), URL http://dx.doi.org/10.1016/S0169-4332(00)00722-4

[111] C.-S. Lau, P.-K. Wei, C.-W. Su, and W.-S. Wang: "Fabrication of magnesium-oxide-induced lithium outdiffusion waveguides", Photonics Technology Letters, **4**(8), 872–875 (August 1992), URL http://dx.doi.org/10.1109/68.149892

[112] C. H. Bulmer: "Characteristics of Ti-indiffused waveguides in MgO-doped $LiNbO_3$", Electronics Letters, **20**(22), 902–904 (October 1984)

[113] H. Nakajima, M. Yuki, T. Oka, H. Yamauchi, S. Kurimura, I. Sakaguchi, and K. Kitamura: "Ti-diffused waveguides fabricated on stoichiometric $LiNbO_3$", in "Proc. Photonics in Switching", p. 242 (2002). Paper PS.ThB5

[114] H. Osterberg and L. W. Smith: "Transmission of Optical Energy Along Surfaces: Part II, Inhomogeneous Media", Journal of the Optical Society America, **54**(9), 1078–1079 (September 1964), URL http://www.opticsinfobase.org/josa/abstract.cfm?URI=josa-54-9-1078

[115] Y. Chen, G. Liu, Y. Zheng, and F. Geng: "Periodically poled Ti-diffused near-stoichiometric MgO:$LiNbO_3$ waveguide nonlinear-optic wavelength converter", Optics Express, **17**(6), 4834–4841 (March 2009), URL http://www.opticsinfobase.org/abstract.cfm?URI=oe-17-6-4834

[116] A. Hellwig, H. Suche, R. Schrör, and W. Sohler: "Titanium-indiffused Waveguides in Magnesium Oxide Doped Stoichiometric Lithium Niobate (MgO:SLN)", in "Proceedings of the ECIO", p. 254 (2005). Paper ThB2-5

[117] L. Ming, C. B. E. Gawith, K. Gallo, M. V. O'Connor, G. D. Emmerson, and P. G. R. Smith: "High conversion efficiency single-pass second harmonic generation in a zinc-diffused periodically poled lithium niobate waveguide", Optics Express, **13**(13), 4862–4868 (June 2005), URL http://www.opticsexpress.org/abstract.cfm?URI=OPEX-13-13-4862

[118] K. R. Parameswaran, R. K. Route, J. R. Kurz, R. V. Roussev, M. M. Fejer, and M. Fujimura: "Highly efficient second-harmonic generation in buried waveguides formed by annealed and reverse proton exchange in periodically poled lithium niobate", Optics Letters, **27**(3), 179–181 (February 2002), URL http://ol.osa.org/abstract.cfm?id=67699

[119] M. Fujimura, T. Murayama, and T. Suhara: "Quasi-Phase-Matched Difference Frequency Generation Devices with Annealed/Proton-Exchanged LiNbO3 Waveguides Buried by Reverse Proton Exchange", Japanese Journal of Applied Physics, **43**(12A), L1543–L1545 (November 2004), URL http://jjap.ipap.jp/link?JJAP/43/L1543/

[120] M. H. Chou, I. Brener, M. M. Fejer, E. E. Chaban, and S. B. Christman: "1.5-µm-band wavelength conversion based on cascaded second-order nonlinearity in $LiNbO_3$ waveguides", Photonics Technology Letters, **11**(6), 653–655 (June 1999), URL http://dx.doi.org/10.1109/68.766774

[121] R. Nouroozi, Y. H. Min, W. Grundkötter, V. Quiring, R. Ricken, and W. Sohler: "Efficient Second Harmonic Generation in Matched Ti:PPLN Waveguide Resonators", in "Proceedings of the ECIO 2007", (2007)

[122] R. Regener and W. Sohler: "Efficient second-harmonic generation in Ti:$LiNbO_3$ channel waveguide resonators", Journal of the Optical Society of America B, **5**(2), 267–277 (February 1988), URL http://www.opticsinfobase.org/josab/abstract.cfm?uri=josab-5-2-267

[123] G. Schreiber, H. Suche, Y. L. Lee, W. Grundkötter, V. Quiring, R. Ricken, and W. Sohler: "Efficient cascaded difference frequency conversion in periodically poled Ti:$LiNbO_3$ waveguides using pulsed and cw pumping", Applied Physics B, **73**(5–6), 501–504 (October 2001), URL http://dx.doi.org/10.1007/s003400100708

[124] M. Asobe, O. Tadanaga, T. Yanagawa, H. Itoh, and H. Suzuki: "Reducing photorefractive effect in periodically poled ZnO- and MgO-doped $LiNbO_3$ wavelength converters", Applied Physics Letters, **78**(21), 3163–3165 (May 2001), URL http://dx.doi.org/10.1063/1.1374228

[125] C. Ziling, L. Pokrovskii, N. Terpugov, I. Savatinova, M. Kuneva, S. Tonchev, M. N. Armenise, and V. M. N. Passaro: "Optical and structural properties of annealed PE:$LiNbO_3$ waveguides formed with pyrophosphoric and benzoic acids", Journal of Applied Physics, **73**(7), 3125–3132 (April 1993), URL http://link.aip.org/link/?JAPIAU/73/3125/1

[126] G. R. Paz-Pujalt, D. D. Tuschel, G. Braunstein, T. Blanton, S. T. Lee, and L. M. Salter: "Characterization of proton exchange lithium niobate waveguides", Journal of Applied Physics, **76**(7), 3981–3987 (October 1994), URL http://link.aip.org/link/?JAPIAU/76/3981/1

[127] M. Falk, T. Woike, and K. Buse: "Reduction of optical damage in lithium niobate crystals by thermo-electric oxidization", Applied Physics Letters, **90**, 251912 (2007), URL http://dx.doi.org/10.1063/1.2750405

Acknowledgements

I would like to thank all people who contributed in the success of this work, including

- Prof. W. Sohler for affiliating me with the integrated optics group
- H. Suche for the countless helpful advice
- R. Ricken, C. Schemel and R. Schrör for the preparation and fabrication of a humongous amount of samples
- V. Quiring for the periodic poling of a major part of the samples
- Y. Lak Lee for many funny moments in the lab
- I. Zimmermann for all the organisational effort in the background